博　士　論　文

Integration of laser line scanning system on articulated arm coordinate measuring machine

知能情報システム工学専攻

郜大勇

令和 05 年 3 月

福岡工業大学　大学院

多関節アームに位置する座標測定機のため のレーザライン走査システムについて

知能情報システム工学専攻　郜大勇

要旨

現代の計測技術は絶えず発展し、レーザを用いたパターン光投影三次元計測技術は航空宇宙、リバースエンジニアリングや文化財の修復、製品の外部欠陥検査などの領域に応用されている。しかし、パターン光やカメラ自体の特性によっては、すべての物体表面を走査することはできない。さらに、大型製品を相手にする場合は、複数の計測したデータを合成しなければならない。そのため、物体の三次元情報を得るためには、三次元座標測定器、マニピュレータ、ターンテーブルなどを組み合わせて使用する必要がある。多関節アーム三次元座標測定機はその柔軟性、軽量性、測定範囲の広さなどの利点により、工作物の寸法測定に応用されている。多関節アームの計測速度は、最大の利点となる。多関節アームとパターン光投影計測の利点を組み合わせ、パターン光投影計測と多関節アームの上端に固定されたカメラを組み合わせ、多関節アームレーザラインスキャンシステムを構築できる。

パターン光投影は表面に投影する本数によって、シングルラインパターンとマルチラインパターンに分けることができる。シングルラインパターンの送信器は1本のレーザラインのみを投影し、カメラ画像上で1本のラインを結像する。シングルラインの縞抽出は多義的ではなく、直交方向のパターン光投影に広く応用されている。マルチラインの1つであるクロスラインパターンは、2本のレーザの三次元再構成技術に基づいており、交差することで複数の方向を測定すると同時に、効率も向上させる。複雑な表面では密度が高くなく、複数回の計測が必要である。マルチラインパターンは、上記問題を解決できる。ただし、3D 登録ラベルとして抽出されたタグは、スキャンする前にターゲットに貼り付けなければならない。

本稿では、多関節アーム三次元座標測定機におけるレーザラインスキャンシステムの統合について研究した。まず、新たな方式とし、固定平板によるシングルライン 3D カメラと多関節アーム三次元座標測定機との関係を校正する方法を提案した。シングルラインと多関節アームシステムとの組み合わせは、スキャンシステムを検証するために使用される。次に、2 つのレーザを用いてクロスラインパターンを構築し、2 つのレーザを周期的に制御して走査系を検証した。最後に、多関節アーム三次元座標測定機をベースとした平行マルチラインパターン投影システムを構築した。その結果、マーキング平行マルチライン投影計測の機能は多関節アームによって提供される空間姿勢に置き換えることができ、同じ設定のクロスラインパターンと比較して、マルチラインパターン光投影計測の効率を向上することが示された。

本論文の内容を、以下のように大まかに紹介する。

第1章はレーザーパターン光投影計測の背景と多関節アーム三次元座標測定機の開

発について述べ、本論文の研究目的について述べる。

第2章はシングルラインパターンの三次元再構成技術とキャリブレーションモデルについて述べる。

第3章は二重レーザを用いたクロスラインパターンの三次元再構成技術について述べる。

第4章はマルチライン三次元再構成技術とマーキング機能の代替方法について述べる。

第5章は実験結果を示し、有効性を検証する。

第6章は本稿の内容をまとめ、今後の課題について論じる。

キーワード：多関節アーム三次元座標測定機，シングルラインパターン光投影計測，クロスラインパターン光投影計測，マルチラインパターン光投影計測

西暦2023年03月01日

Integration of laser line scanning system on articulated arm coordinate measuring machine

Doctoral Course of Intelligent Information System Engineering

Tai Dayong

Abstract

With the rapid development of measuring technology, the 3D structured light measurement technology based on laser is widely applied to various fields, such as aerospace, reverse engineering and restoration of cultural relics, product surface defect detection, and other fields. Because the structured light cannot scan all the objects by itself. Moreover, when facing some large-size products, it is necessary to combine the data of multiple measurements. So it must be used with a coordinate measuring instrument, manipulator and turntable to obtain the objects' three-dimensional information. The articulated arm coordinate measurement machine is widely used in the measurement of workpiece size due to its flexibility, light weight and wide measuring range. The measuring speed of articulated arm is the greatest advantages. Combining the advantages of the articulated arm and structured light measurement, an articulated arm structured light scanning system is constructed by combining structured light and a camera fixed at the upper end of articulated arm.

The scanning structured light system based on laser can be divided into single-line structured light systems and multi-lines structured light systems according to the number of laser planes, single-line structured light emitter only shoots out a laser line, and images a line in the camera. The extraction of light strips not being polysemous, it is easy to achieve, and so is widely used along the orthogonal direction of the structured light. Cross-line structured light based on two lasers 3D reconstructed technology, The measurement of two cross lasers can move in multiple directions, while also improving efficiency. And the points' density is not high for the complex surface, so it needs to be measured several times. Multi-lines structured light can solve the problem. However, marks extracted as 3D registered labels must be posted on the target before scanning.

In this paper, we study the integration of laser line scanning system on articulated arm coordinate measuring machine. Firstly, we propose a new calibration approach for the relationship between the single-line structured light 3D camera and the articulated arm CMM via a fixed flat board. the combination the single-line structured light with the articulated arm systems is used to verify the scanning system. Secondly, we use two lasers to construct cross-lines structured light and control two lasers periodically to verify the scanning system. Finally,

we construct parallel multi-lines structured light system based on the articulated arm CMM. It demonstrated that the function of marks parallel multi-lines structured light used can be replaced by the spatial attitude provided by the articulated arm, and the efficiency of the multi-lines scanning system is improved comparing with the same setting of cross-line structured light.

The outline of this thesis is as follows.

Chapter1 introduce the background of the laser structured light measurement and development of the articulated arm CMM, and the purpose of this research.

Chapter 2 study single-line structured 3D reconstructed technology and calibration model.

Chapter 3 study cross-line structured light based on two lasers 3D reconstructed technology.

Chapter 4 presents multi-lines structured light 3D reconstructed technology and the method of replacing of the function of marker points.

Chapter 5 shows the experimental results of the proposed method to verify the effectiveness of the method.

Chapter 6 summarizes this paper and elaborate the future topic.

Keyword *: Articulated arm ,3D structured light, Single-line structured, Cross-line structured, Multi-lines structured light.*

Mar. 01, 2022

Index

Chapter 1 Introduction

1.1 Background

The development of science and technology depends on productivity, and measurement science is no exception. Measurement technology is currently under development. With the rise of 3D printing technology, the measurement of complex surface contours has become the main field of study for researchers. In some key industries, such as aerospace, wind turbine blades and automotive batteries[1-3], it is more demanding in terms of shape measurement with high standards. In a word, we can call the measurement of complex surface contours 3D measurement technology. This kind of technology has a range of applications, from quality assurance to VR to reverse engineering.

The measurement carried out by common gauges such as dial indicator and vernier caliper is called traditional measurement method. It is a kind of relative measurement, and the commonality is that all of these gauges use themselves as a measurement base. Traditional measurement often has limited range, which means once the measured object is too large or too small over the range, it cannot be measured. Therefore, the measuring range of traditional measurement is very narrow. With the advancement of measurement technology and measuring demands, a new measuring instrument, Coordinate Measuring Machining (CMM), has emerged in the 1960s. The development of CMM means a lot. On the one hand, machining such as automatic machine tools, CNC machine tools with high efficiency, and parts with complex shapes requires fast and reliable measuring equipment. On the other hand, the advancement of electronic, computer, digital control, and precision processing technology provides a technical basis for the development of CMM[4]. The modern CMM system is a comprehensive interdisciplinary field with the integration of optics, electronics, sensors, imaging, manufacturing, and computer technology-involving a wide range of field of study and requiring support from those related to this study. Meanwhile, a number of non-contact measurement technologies based on optics, electromagnetism and acoustics have developed rapidly, and they are more efficient than contact measurement technology, non-destructive and have large measuring range. At present, the optical-based non-contact measurement method is the most widely used 3D measurement method[5].

Optical 3D measurement technology is the most important and common method in non-contact measurement[6-7]. Because of its good reputation for speed and precision, the use of this technology has become commonplace in industries and among manufacturers. Optical 3D measurement technology can be divided into two categories: active measurement and passive measurement. Active measurement is to use a human-controlled light source to irradiate the measured object in order to obtain the 3D measurements of the measured object based on the structured light, while passive measurement, without any human factors, is to obtain the 3D measurements of the surface of the measured object only by camera and other optical equipment

in the natural light environment. The main active 3D measurement methods include time-of-flight method, laser triangulation, Moire fringe method, optical interferometry, and projection structured light method, among which the projection structured light method includes phase shift measurement contouring[8-9] and Fourier change contouring[10-11]. Passive optical 3D measurement does not require special light sources nor complex equipment. Passive optical 3D measurement usually uses one or more cameras to shoot the measured object, so as to obtain a 2D image which contains the information (shape, size, color, etc.) of the measured object. However, the 3D measurement system composed by only one camera is called monocular vision. And by the same logic, two cameras called binocular vision, three and more called multi-vision vision. A vision system consisting of at least two cameras, known as a stereo vision system, can provide depth information by analyzing the differences between the images captured by the two cameras. The difference between the two images, known as the disparity, can be used to calculate the distance between the camera and the object.

1.2 Articulated arm CMM

In the mid1970s, the UK company, Renishaw, developed a 3D trigger probe [12], and widely applied in CMM, which furthered the development of CMM technology. With the growth of modern microcomputer technology and the widespread use of CMM, the performance of this machine has been greatly improved, and production costs have also dropped sharply, enabling CMM to become an important equipment in modern measurement technology [13]. Orthogonal CMM has a broad application. On the one hand, because the orthogonal coordinate system is intuitive and convenient for coordinate transformation, the operation is easy and acceptable; on the other hand, it provides guaranteed precision. Today, CMM has been quite widely implemented in many industries, such as machinery manufacturing, automobile, electronics, aerospace, and national defense. It has become an indispensable measuring tool in modern industrial testing, quality control and manufacturing technology. However, with the sustained development of production and science and technology, the traditional orthogonal coordinate measurement system can hardly meet the on-site measurement requirements in many occasions. The reasons are as listed: although it provides simple and intuitive probe space motion model, it is subjected to the size of the structure of machine, which causes limited measuring range; measurement has to be carried out on machine; the cost is also very high. Considering above shortcomings, a non-orthogonal CMM was developed [14]. The non-orthogonal CMM is light and flexible, and it is easier to probe the dead angles of measured objects. It also has a larger measurement range. As a result, more useful data can be collected in a shorter time.

The articulated arm CMM is a new type of multi-degree-of-freedom non-orthogonal coordinate measurement system. It replaces the length measurement reference with an angle measurement reference [15]. It connects several rods and one probe in series with a rotating joint. One end of the articulated arm CMM is fixed to the base, while the free range of

movement of the end probe forms a spherical measuring space. The surveyor can manually move the probe to measure in its given space, use the measurement software to calculate the 3D coordinates of the collected points, and then obtain the parameter value or deviation to be measured through data processing. Compared with traditional orthogonal coordinate measuring system, the articulated arm CMM has many advantages, such as small size, light weight, good flexibility, large measuring range, portability, low cost, and the capacity to realize on-site measurement.

1.2.1 Research on Articulated arm CMM at home and abroad

Founded in 1982, the US company, FARO, is one of the earliest manufacturers in the world

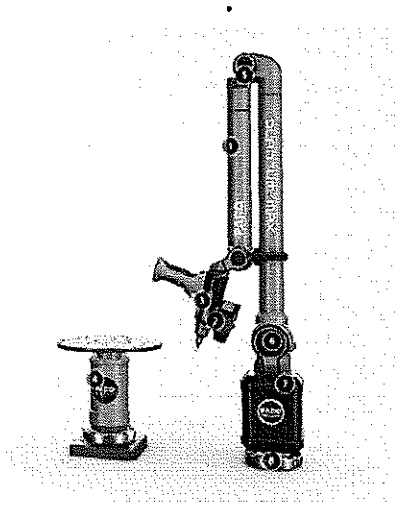

Quantum^S Max

7-Axis	SPAT[1]	P_{SIZE}[2]	P_{FORM}[3]	L_{DIA}[4]	E_{UNI}[5]
2.0m (6.6ft)	0.018mm 0.0007in	0.01mm 0.0004in	0.02mm 0.0008in	0.04mm 0.0016in	0.025mm 0.001in
2.5m (8.2ft)	0.02mm 0.0008in	0.011mm 0.0004in	0.022mm 0.0009in	0.044mm 0.0017in	0.028mm 0.0011in
3.0m (9.8ft)	0.032mm 0.0013in	0.016mm 0.0006in	0.032mm 0.0013in	0.074mm 0.0029in	0.05mm 0.002in
3.5m (11.5ft)	0.045mm 0.0018in	0.02mm 0.0008in	0.039mm 0.0015in	0.09mm 0.0035in	0.062mm 0.0024in
4.0m (13.1ft)	0.055mm 0.0022in	0.026mm 0.001in	0.044mm 0.0017in	0.108mm 0.0043in	0.076mm 0.003in

Fig.1.1 Faro Arm accuracy-contact

SPAT- single point articulation test

P_{SIZE} - sphere probing size error comparing measured versus nominal values

P_{FORM} - sphere probing form error,

L_{DIA} - sphere location diameter error (Diameter of the spherical zone containing the centers of a sphere measured from multiple orientations)

E_{UNI} - Distance error between two points comparing measured versus nominal values

https://www.faro.com/en/Products/Hardware/ScanArms

to self-develop and produce articulated arm CMM and laser trackers, and is currently the world's largest manufacturer of articulated arm CMM with output accounting for more than half of the total market [16]. FARO 3D Portable Measuring arm has many series and is among the advanced in the world. For example, the Quantum S Max 7-axis measuring arm (accuracy see Fig.1.1). The measuring range includes 2.0m, 2.5m, 3.0m, 3.5m, 4.0m, and a single point accuracy of up to 0.018mm. The scanning accuracy specifications with the laser scanning camera are shown in Fig.1.2. The accuracy is up to 0.03mm.

Quantum^{S} Max

FAROBlu Max	xR	xP	xS
2.0m (6.6ft)	0.03mm 0.0012in	0.038mm 0.0015in	0.046mm 0.0018in
2.5m (8.2ft)	0.034mm 0.0013in	0.042mm 0.0017in	0.05mm 0.002in
3.0m (9.8ft)	0.04mm 0.0016in	0.048mm 0.0019in	0.055mm 0.0022in
3.5m (11.5ft)	0.054mm 0.0021in	0.061mm 0.0024in	0.068mm 0.0027in
4.0m (13.1ft)	0.068mm 0.0027in	0.074mm 0.0029in	0.08mm 0.0031in

Fig.1.2 Faro Arm accuracy-scan, xR, xP and xS are different specifications
https://www.faro.com/en/Products/Hardware/ScanArms

Fig.1.3 shows Hexagon absolute articulated arm CMM, with a measuring range from 1.2 meters to 4.5 meters, and a total of 7 different specifications. Compatible with all kinds of contact probes and bent probes, it is currently the highest precision articulated arm CMM of Hexagon.

Fig.1.3 Hexagon absolute articulated arm CMM
https://acquip.com/hexagon-absolute-arms/

PMT Technologies (Suzhou) Co., Ltd. [18], with its product categories and functions

reaching the world-leading level. The categories include M series, E series, and P series. The P-series products (Fig.1.4) have the highest accuracy, and a single point accuracy of up to 0.012mm (the accuracy specifications see Fig.1.5).

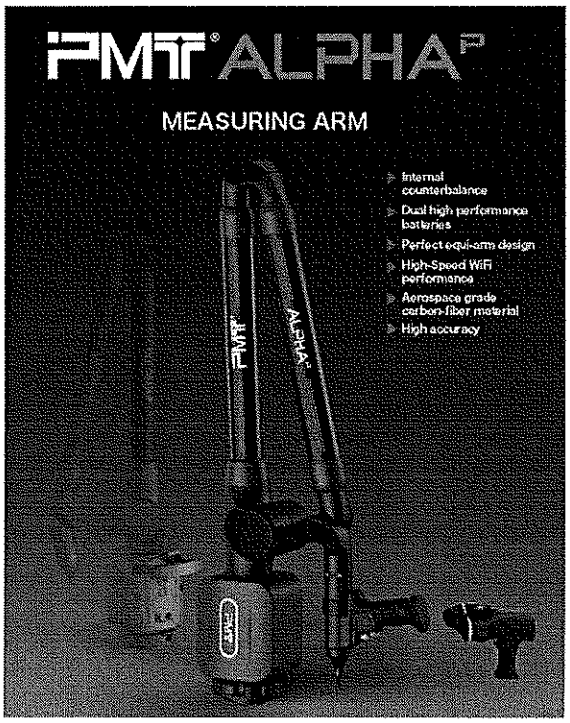

Fig.1.4 P series arm
https://www.pmt3d.com/products.html

Contact Measurement(Arm)										
Measurement Range	[1] SPAT		[2] EUNI		[3] PSIZE		[4] PFORM		[5] LDIA	
	6Axis	7Axis	6Axis	7Axis	6Axis	7Axis	6Axis	7Axis	6Axis	7Axis
1.5m	0.012mm	—	0.022mm	—	0.007mm	—	0.012mm	—	0.024mm	—
2.0m	0.016mm	0.018mm	0.024mm	0.026mm	0.008mm	0.010mm	0.015mm	0.019mm	0.030mm	0.038mm
2.5m	0.018mm	0.020mm	0.026mm	0.028mm	0.009mm	0.011mm	0.018mm	0.022mm	0.032mm	0.042mm
3.0m	0.026mm	0.032mm	0.038mm	0.048mm	0.012mm	0.016mm	0.025mm	0.032mm	0.045mm	0.072mm
3.5m	0.036mm	0.045mm	0.052mm	0.061mm	0.016mm	0.020mm	0.034mm	0.039mm	0.060mm	0.088mm
4.0m	0.045mm	0.055mm	0.063mm	0.076mm	0.020mm	0.026mm	0.038mm	0.044mm	0.077mm	0.098mm
4.5m	0.055mm	0.065mm	0.080mm	0.095mm	0.028mm	0.036mm	0.050mm	0.065mm	0.101mm	0.122mm

Fig.1.5 Accuracy specification
https://www.pmt3d.com/products.html

In our country, VMC8000M shown in Figure1.6 is one of the products of Kosaka Laboratory.

The accuracy of repeatability of fixed points can reach 0.019mm(2sigma), and measuring accuracy is 0.034mm(2sigma) [19].

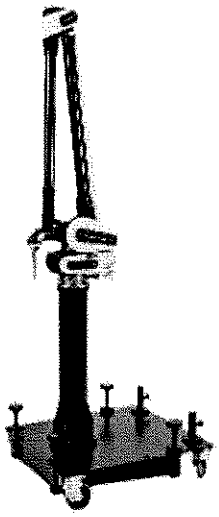

Fig.1.6 VMC8000M series, Kosaka Laboratory
https://www.kosakalab.co.jp/english/information/detail.html?itemid=61&dispmid=890

1.3 The optical 3D measurement

Table 1 The classification of 3D measurement

Active optical 3D measurement	Time-of-flight method
	laser triangulation
Passive optical 3D measurement	binocular stereo vision

This section describes the laser 3D measurement method in active optical 3D measurement and the measurement method based on binocular stereo vision in passive optical 3D measurement. The 3D laser measurement is a new 3D measurement method, which has fast speed and good anti-interference ability in the actual use, and also makes it an important and commonly used method in non-contact measurement. In the industrial online measurement, it has good application [20-21]. The 3D laser measurement system usually consists of components such as laser projectors and cameras. In a single measurement process, the laser projector projects the laser to the surface of the measured object, generates light bar data on the surface, and then captures these light bar data through the camera, converts its 3D data into 2D data. After a series of image processing, the pixel coordinates of the center of the light bar can be obtained. Finally, the calibration data of the system model is used to determine the 3D coordinates of the center of the light bar, so that the 3D data of the center of the light bar on the surface of the measured object can be reconstructed [22].

1.3.1 The time-of-flight method

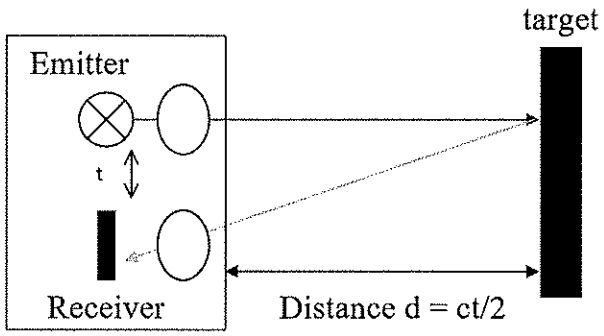

(a)

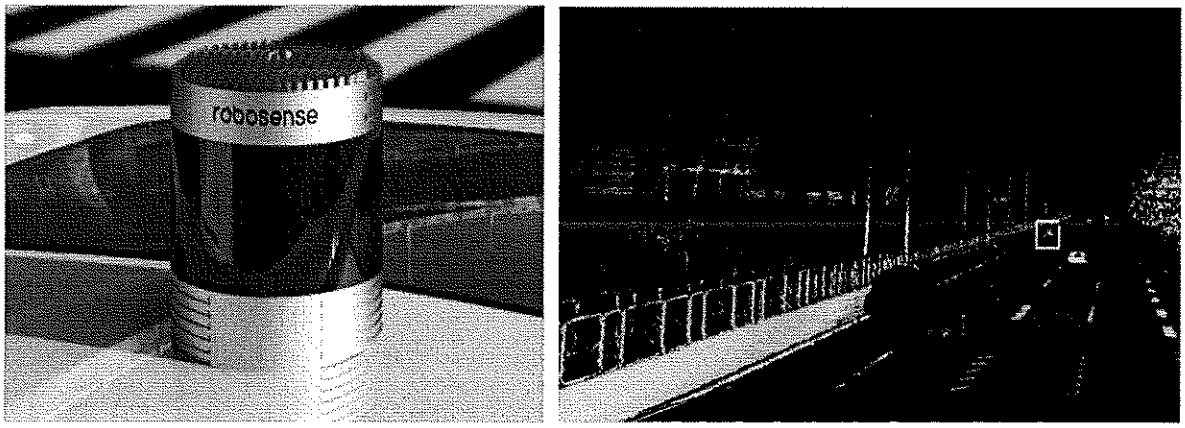

(b) (c)

Fig.1.7 In-car LIDAR (a) time-of-flight princle (b) detector (c) 3D point clouds
https://www.robosense.cn/rslidar/RS-Ruby_Plus

The time-of-flight method [23-24] is also known as laser ranging method, which is often used for LIDAR ranging. This method uses the laser to irradiate the measured object and then reflect back, receive the reflected laser through the laser receiver, and then calculate the time it takes to transmit-receive the laser. Because the laser speed is known, the distance between the laser emitter and the measured object can be obtained. We call this method the time-of-flight. This method neatly converts the temporal resolution of laser detection into the actual required distance accuracy, and is often used for long-distance measurement. As is shown in Fig.1.7, this method is used very widely in in-car detection radar [25].

1.3.2 The laser triangulation measurement

Laser-based optical 3D measurement has been evolved for decades. Due to the characteristics of high brightness and monochromaticity, laser is gradually adopted and also proved to be practical in different fields of measurement. It has features of high precision, fast speed and

good accuracy. With the constant advancement of science and technology and people's rising demands, the 3D laser scanning technology has gradually evolved from simple ranging to 3D reconstruction of the entire object surface. Laser triangulation [26] is the most commonly used active optical 3D measurement method. The laser triangulation measurement diagram is shown in Fig.1.8. A laser beam is emitted through the laser light source and projected to the surface of the measured object, then the reflected laser light is focused through the lens, and the detector receives the focused laser, and images on the detector. When the position of the measured object moves vertically down S, the imaging position on the detector moves the distance *e*, and there is a certain relationship between the change of the imaging position and the change of the actual position. Based on this relationship, the real distance of the measured object can be calculated

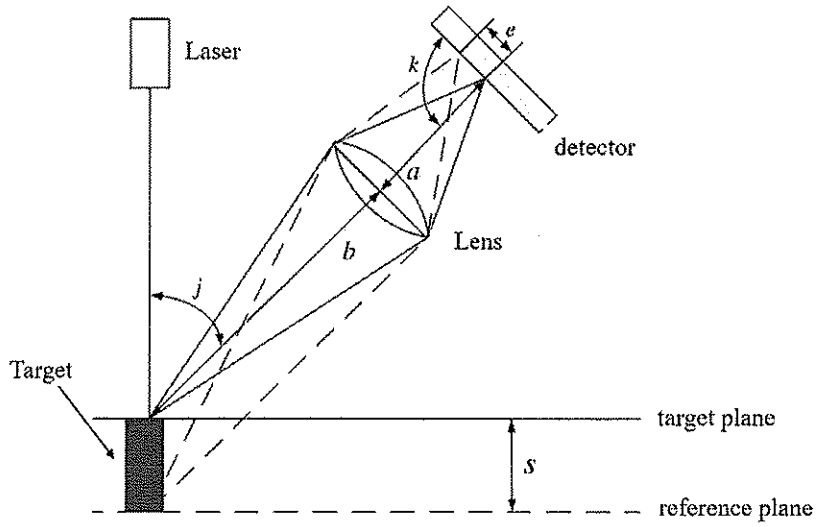

Fig.1.8 laser triangulation measurement diagram

through the moving distance of the imaging location.

1.3.3 The binocular stereo vision measurement

Binocular stereo vision [27-28] consists of two cameras, and the geometric relation is simple (shown in Fig.1.9). It uses the spatial position between the two cameras and the matching relation of the same point in the space in the camera image to obtain the real 3D coordinate value of the point. The binocular stereo vision measurement usually requires the following six steps:

(1) Image capture. Use the two cameras to capture the measured object and obtain a 2D images.

(2) Extraction of image features. Extract features of captured 2D images, including texture, shape, and color.

(3) Feature matching. Find the points with same features in the 2D images through above Extraction of image features and certain methods to match them one by one.

(4) 3D reconstruction. Determine the 3D coordinate points of the 2D image matching points based on the calibration results of the two cameras.

(5) 3D merging. Since the reconstruction through one time shot is only a part of the measured object, we need to joint together the 3D point cloud reconstructed each time by virtue of certain external conditions, so as to ensure the continuity of the 3D data of the object.

1.3.4 Research on 3D laser scanning technology

1.3.4.1 The 3D laser scanning technology in the word

The research on 3D laser measurement technology started early in foreign countries, and so far there have been well-developed theoretical systems in the world. In 1994, M. Levoy and his team used laser triangulation to design a 3D laser scanning device by applying high-definition cameras to collect the 3D contour data of Michelangelo's sculptures and then carrying on the 3D reconstruction, which has successfully opened up doors for the 3D laser scanning technology. In 1997, EI-Hakim of NRC Canada built a complete hardware platform. They fixed the laser projector and CCD camera on an experimental trolley to form a data acquisition and registration system. In 1998, they realized 3D modeling of the indoor scene on the basis of the original system; In 2001, I.Stamos and P.K. Allen realized a complete 3D scanning system that enables 3D reconstruction of large outdoor buildings and obtains the color texture information at the same time, and they finally established a real 3D architectural model. Over more than two decades of rapid development, companies that research and produce 3D laser scanners have popped up mostly in Europe and the United States. These companies have different products in terms of measurement range, accuracy, laser type and measurement object. Let's take some of the company's products as examples.

The Canadian company Polhemus [29] has developed a single-line-based handheld 3D laser scanner - FastSCAN II (see Fig.1.9, use laser triangulation measurement method). The scanner completes the 3D reconstruction of the surface of the measured object by projecting the line laser on the surface of the measured object, and at the same time using the cameras at both ends of the scanner to shoot it, recording the laser line information on the surface of the measured object. When the measurement distance is limited within 50cm, the resolution can reach 0.01mm, and the measurement accuracy can reach up to 0.18mm. The scanner can be used to scan human faces. This way, digital human shapes can be created for later animation and multimedia production, as well as for 3D measurement and model preservation of small artifacts.

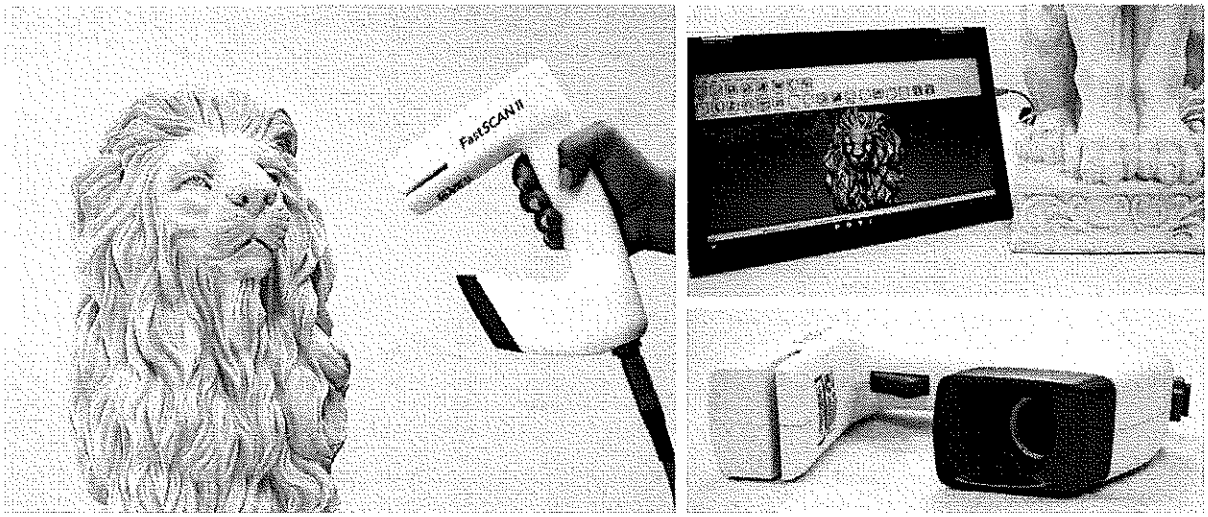

Fig.1.9 FastSCAN II, laser triangulation measurement method
https://polhemus.com/scanning-digitizing/fastscan/

Handy scanner use laser triangulation and binocular stereo vision methods to reconstruct 3D object. Canadian company Creaform [30] has developed a hand-hold 3D laser scanner based on crossover multi-line, HandySCAN 3D-BLACK series (see Fig.1.10). It boasts a measurement speed of 1,300,000 points per second and has a resolution of up to 0.025mm. It is a mobile data acquisition system (also its own positioning system), without the need for external tracking or positioning equipment. It uses triangulation measurement to identify its relative position with the measured object in real time. The system is light with weight of less than 1 kg. It can be

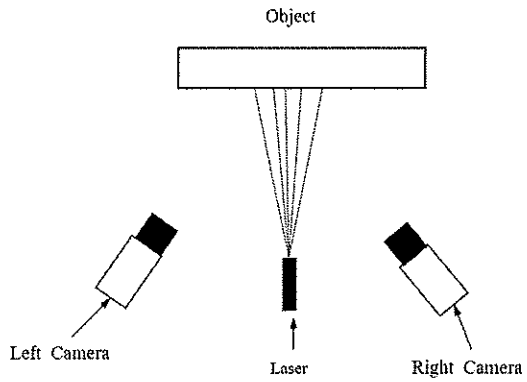

(a) laser triangulation and binocular stereo vision methods

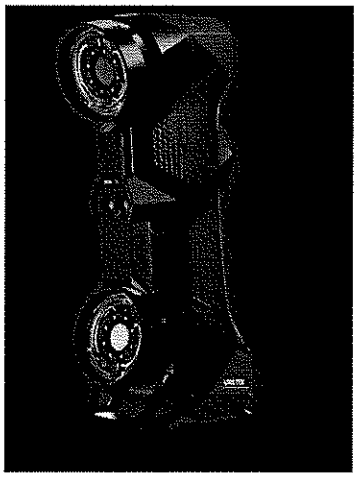

(b) product

Fig.1.10 HandySCAN 3D
https://www.zg-3d.com/product.html

packed into a small suitcase, easy to carry, and 3D scanning anytime, anywhere. Its supporting

software system also has powerful processing functions, which can automatically fill and repair the reconstructed 3D point cloud.

1.3.4.2 The 3D laser scanning domestic technology

In our county, as a supplier of sensors, measuring systems, laser markers, microscopes, and machine vision systems worldwide, KEYENCE is at the forefront of factory automation [31]. KEYENCE laser profilers (shown in Fig.1.11) are laser displacement sensors that collect height data across a laser line rather than a single point. This enables 2D/3D measurements such as height difference, width, or angle to be performed using a single sensor.

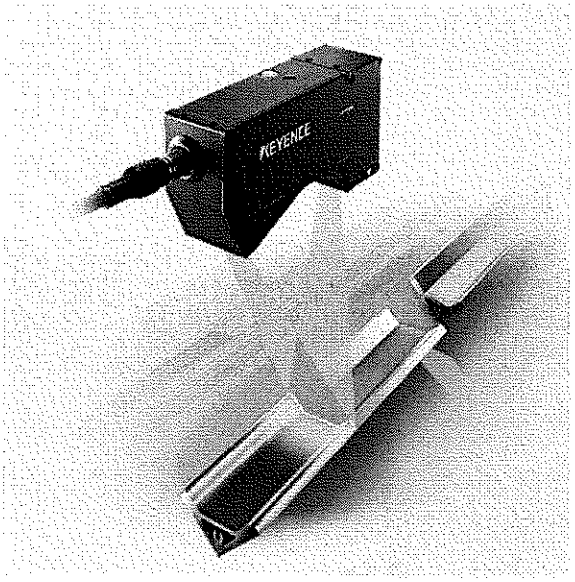

Fig.1.11 laser profilers
https://www.keyence.co.in/products/measure/laser-2d/

1.4 The purpose of this research

1.4.1 The aim of this study

The single-line has been used widely used. However, it needs to combine with Coordinate Measuring Machine, Robot and Turntable to obtain 3D information of the objects. The point clouds obtained by handheld 3D laser scanner one frame are relatively sparse, so marker points for registered point clouds should be attached on the object before scanning. In this paper, we study the combination of articulated arm CMM with laser structured light. The accuracy of the articulated arm CMM scanning system based on single-line can reach 0.05mm. The speed of cross-lines scanning system with articulated arm CMM is 1.2 faster then single-line, and the

multi-lines laser scanning system with articulated arm CMM is researched, which can scan and reconstruct objects without attaching marker points.

1.4.2 The content and outline of the research

The research contents of this paper include: build a 3D laser scanning system based on single-line, propose a flat-based hand-eye calibration method. In order to improve the efficiency of scanning, we make cross-lines structured light by adding a laser to the single-line structured light. A method of periodically controlling the two laser emitters is used to solve the ambiguity of light strip extraction. By using the postures of the articulated arm CMM provided during the scanning, we solve the problem that multi-line scanning needs to be labeled with marker points. The 3D coordinates captured by the camera are converted into a unified coordinate system of the articulated arm CMM, so that the continuity of 3D reconstruction can be guaranteed.

The outline of this paper is as follows:

Chapter I: Introduction. This chapter mainly introduces the reconstruction method of articulated arm CMM and 3D laser measurement, and reviews the research status of 3D laser measurement at home and abroad, so as to put forward the research object, purpose and significance of this paper, and elaborate and plan the overall content of this paper.

Chapter 2: Construction and calibration of single-line laser scanning system models. This chapter gives detailed description on how to achieve the hand-eye calibration of the single-line structured light 3D camera and the end-effector of the articulated arm CMM.

Chapter 3: This chapter introduces the cross-lines structured light 3D camera and the method to distinguish between the two laser lines when two laser emitters open simultaneously.

Chapter 4: Introduce the function of marker points for multi-lines 3D camera and the principle of reconstruction 3D point clouds from one frame in binocular model. Use the posture to replace the function of marker points.

Chapter 5: System Construction and application experiments. This chapter mainly introduces the hardware composition, software design, measurement process and actual use of the systematic platform built in this paper.

Chapter 6: Summary and Outlook. This chapter summaries the content of this study, and outlines the problems that need to be discussed in further studies.

Chapter 2 Single-line scanning system

2.1 Hardware structure

Fig. 2.1 shows a schematic of the system we propose. A single-line laser structured light and a 2D camera are fixed at the end of the articulated arm with seven degrees of freedom to form the 3D measurement system, the articulated arm and the camera are connected to computer with USB interface respectively. The articulated arm base coordinate system is defined as $O_bX_bY_bZ_b$, the origin is located in the center of the base, the X, Y, Z axes are defined as shown in the figure 2.1. The coordinate system of the end-effector of the articulated arm defined as $O_tX_tY_tZ_t$, the origin is located at the center of the end hard probe ball, and the Z-axis is defined as the extension direction along the end arm. The coordinate system of the 2D camera is defined as $O_SX_SY_SZ_S$ and the Z axis is defined along the optical axis of the camera lens.

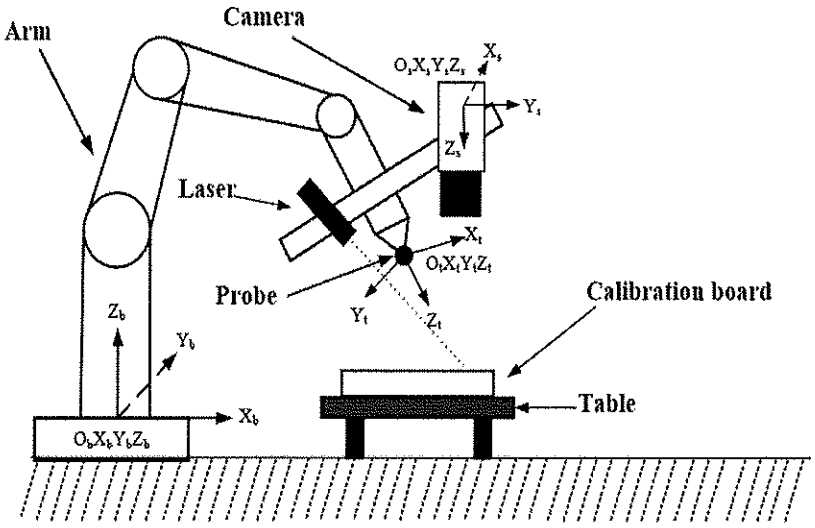

Fig.2.1 Schematic articulated arm CMM laser scanning system

2.1.1 Articulated arm CMM kinematic Model

The articulated coordinate measuring machine is a general term for a type of measuring instrument, generally speaking, it refers to the group of frames, measuring arms, measuring heads, etc. through the rotation joint series to form a type of coordinate measuring instruments, even if specific to this there are many types. For example, the most common measuring arm still contains 6 degrees of rotation freedom, the most common configuration of which is, the measuring machine by three pairs of rotating shafts connected to the column and members (including measuring arm and probe). There have also been 5-axis coordinate measuring arms on the market, with a total of 5 degrees of freedom, using 5 encoders and 3 rods; For easy

operation and improved flexibility, there is also a 7-axis articulated coordinate measuring machine. This machine has a total of 7 rotating joints. Recently, a new structural form has been proposed, the basic form of which is a full-structure articulated coordinate measuring machine, but it attaches an adjustable fastening device between the column of the measuring machine and the first measuring arm, and the relative position relationship between the column and the first measuring arm is completely fixed after the fastening device is locked if necessary. Theoretical analysis shows that in such full-structure machine, the error of the first joint and the second joint is larger than that of other joints, so although the measurement range is limited, its local measurement accuracy has been improved. At the same time, when the fastening device is loosened, it can move the probe to another position for measurement, so a large measuring range can be achieved.

There are diversified structures of articulated coordinate measuring machine, and the key of its mechanical design and processing is how to skillfully put the angle encoder and ensure the accuracy of rotation, which is also the hard part in mechanical design. Therefore, the mechanical design basically revolves around the angle encoder. Because of this, the choice of angle encoder became a starting point for mechanical design. In addition, electrical problems need to be addressed in the mechanical design, such as how to send the power signal and cables of the angle encoder from the joints to the circuit board, and how to avoid entanglement of the cables during use.

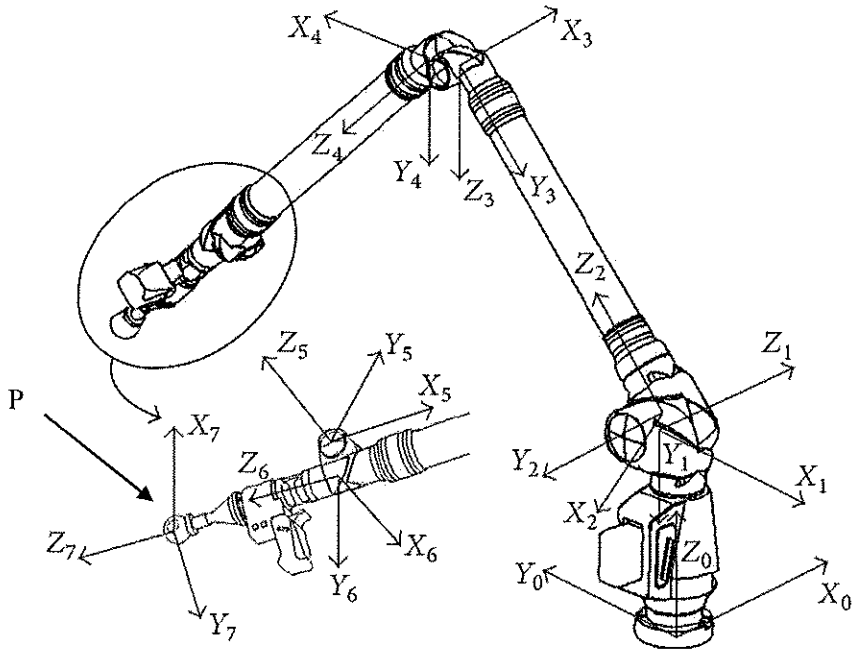

Fig.2.2 Faro arm reference systems

We can learn from the joint design of FARO articulated coordinate measuring machines. It features a total of 7 articulated movements similar to Fig.2.2. First, it chooses a quite compact disc type grating, so that the installation space of the grating is relatively small. In order to avoid entanglement of wires, it uses conductive slip rings and distributed circuit systems in the joints(Fig.2.3). Each board is connected to an angle encoder and only needs to pass through the power and signal lines within the conductive slip ring. In order to prevent dust from affecting the rotation accuracy of the joints and the reading of the grating disc, there are end caps at both ends to close the entire structure. A pair of bearings is arranged between the internal shaft and the bushing, and the pair of bearings is preloaded by parts, which ensures the accuracy of joint rotation. At the gap between the bearing and bushing, there is also a device that prevents excessive rotation of the joint [32-34].

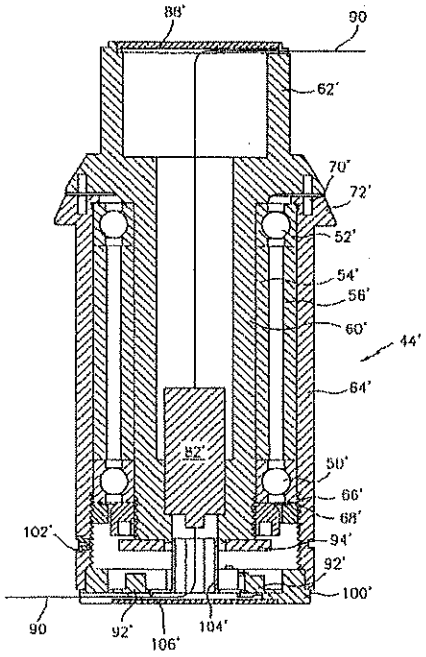

Fig.2.3 Faro arm US Patent 6920697B2

The design goals of the mechanical structures are dexterity and stability. On the one hand, because the articulated coordinate measuring machine is a manually operated measuring equipment, if its structure is too bulky, it will affect the actual use; On the other hand, a stable mechanical structure is the basis for ensuring the accuracy of articulated arm CMM. In addition to the design of the joint, it is also necessary to consider the choice of rod material. At present, manufacturers usually select carbon fiber tubes with light weight and high strength.

Structurally, articulated arm CMMs resemble open-chain robots or manipulators commonly found in industry. The kinematic equation of the robot representing each rod of the robot relative to the absolute coordinate system in space is the basis of the mathematical modeling of the articulated coordinate measuring machine. Therefore, with the help of the D-H method that has

been matured in robot research, the measurement equation of the joint coordinate measuring machine can be established.

The modeling principles of articulated arm CMM can refer to the modeling principles of robots, and robot modeling requires the following three principles [35-37]:

(1) Completeness: Completeness requirements mean that the model has enough parameters to fully describe the movements of the robot.

(2) Continuity: Continuity requirements mean that the model is continuous, that is, the small movements of the robot can be reflected through the model; It also requires that small changes in the structure of the robot be reflected in small changes in model parameters.

(3) Non-redundancy: Non-redundancy requires that the model contains a minimum number of parameters and that the error model does not contain redundant parameters.

It should be noted that although the articulated coordinate measuring machine is structurally similar to the robot operator, the robot operator focuses on the attitude of the end effector in space, while the articulated coordinate measuring machine usually needs to only focus on the coordinates of its probe (ball), and does not need to pay excessive attention to the pointing (attitude) of its probe. Therefore, if the robot model is applied directly, it often contains redundant parameters. In order to describe the position and direction of each rod of the articulated arm CMM, we need to use the following Cartesian coordinate systems. They are absolute coordinate system, base coordinate system, member coordinate system, and measuring machine probe coordinate system.

The most commonly used kinematic modeling method in industrial robots is the Denavit-Hartenberg square [38], which determines the A matrix that represents the relative position and orientation of two adjacent members. The DH method is based on the geometric parameters and joint variables of the members of the space linkage. The main parameters of the joint are:

(1) The length of the member l_i- the shortest distance between the axes of the two joints, that is, the length of the perpendicular line between the two axes, as shown in figure 2.4. When two axes intersect at a point, l_i=0.

(2) Torsion angle α_i of the member - move any axis of the same member to the other axis to intersect, then the two lines determine a plane perpendicular to the length of the member l_i, and the plane intersection angle of the two lines is the torsion angle α_i of the member.

(3) the joint variable refers to the change in the relative position of two adjacent members, and when the two members are connected by a rotating joint, the joint variable is the angle θ_i. As shown in the right figure of figure 3.3, the length line l_i of the i member is translated to the length line l_{i-1} of the $i-1^{th}$ member and intersects it, and they determine a plane θ_i angle that intersects the I-axis of the joint is measured in this plane: the starting line of θ_i is the extension of l_{i-1}, and the ending line is the parallel line of l_{i-1}, and its positive direction is determined by the right-hand rule of the i-axis unit vector.

(4) The offset amount d_i of member i is the distance at which the rod length l_i and l_{i-1} are intercepted on the axis of the $i-1^{th}$ joint.

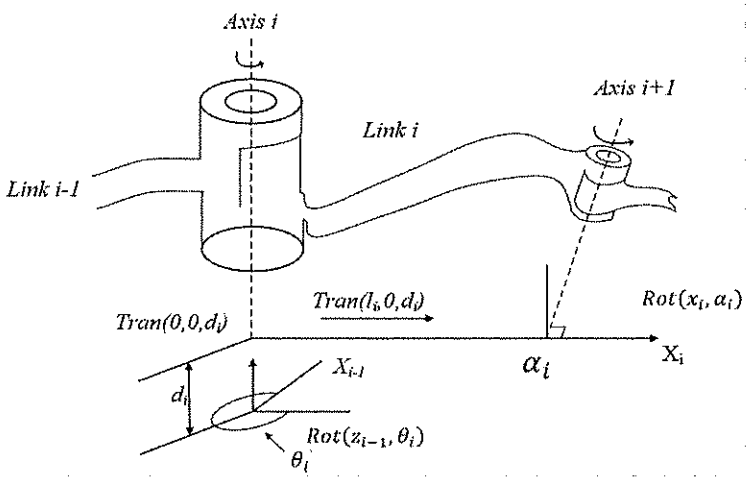

Fig.2.4 Link model between two axises

According to DH model, we have matrix A_i:

$$A_i = Rot(z_{i-1},\theta_i)Trans(0,0,d_i)Trans(l_i,0,0)Rot(x_i,\alpha_i) \quad (2.1)$$

where

$$Rot(z_{i-1},\theta_i) = \begin{bmatrix} cos\theta_i & -sin\theta_i & 0 & 0 \\ sin\theta_i & cos\theta_i & 0 & 0 \\ 0 & 0 & 1 & 0 \\ 0 & 0 & 0 & 1 \end{bmatrix} \quad (2.2)$$

$$Trans(0,0,d_i) = \begin{bmatrix} 1 & 0 & 0 & 0 \\ 0 & 1 & 0 & 0 \\ 0 & 0 & 1 & d_i \\ 0 & 0 & 0 & 1 \end{bmatrix}$$

$$Trans(l_i,0,0) = \begin{bmatrix} 1 & 0 & 0 & l_i \\ 0 & 1 & 0 & 0 \\ 0 & 0 & 1 & 0 \\ 0 & 0 & 0 & 1 \end{bmatrix} \quad (2.3)$$

$$Rot(x_i, \alpha_i) = \begin{bmatrix} 1 & 0 & 0 & 0 \\ 0 & cos\alpha_i & -sin\alpha_i & 0 \\ 0 & sin\alpha_i & cos\alpha_i & 0 \\ 0 & 0 & 0 & 1 \end{bmatrix} \tag{2.4}$$

The form of collated into a matrix is:

$$A_i = \begin{bmatrix} cos\theta_i & -sin\theta_i cos\alpha_i & sin\theta_i sin\alpha_i & l_i cos\theta_i \\ sin\theta_i & cos\theta_i cos\alpha_i & -cos\theta_i sin\alpha_i & l_i sin\theta_i \\ 0 & sin\alpha_i & cos\alpha_i & d_i \\ 0 & 0 & 0 & 1 \end{bmatrix} \tag{2.5}$$

D-H method, and the resulting coordinate conversion relationship is shown in figure 2.2. Let the coordinate system of the base of the measuring machine be $O_0X_0Y_0Z_0$, establish the coordinate system $O_iX_iY_iZ_i(i = 0,1,2,3..6)$ shown in figure 2.2 on each joint i, $P(X_p, Y_p, Z_p)$ is the measuring machine probe, and the parameters of each conversion matrix are given in Table 2.

Table 2. Parameters matrix for measure

Axis	θ_i	θ_{i0}	α_i	$cos\alpha_i$	$sin\alpha_i$	l_i	d_i
1	θ_1	θ_{10}	$-\pi/2$	0	-1	0	d_1
2	θ_2	θ_{20}	$\pi/2$	0	1	$-l_2$	0
3	θ_3	θ_{30}	$-\pi/2$	0	-1	0	d_3
4	θ_4	θ_{40}	$\pi/2$	0	1	$-l_4$	0
5	θ_5	θ_{50}	$-\pi/2$	0	-1	0	d_5
6	θ_6	θ_{60}	$\pi/2$	0	1	$-l_6$	0
7	θ_7	θ_{70}	$-\pi/2$	0	-1	0	d_7

According to the DH method, the measurement equation of the articulated arm CMM can be obtained as:

$$\begin{bmatrix} X_p & Y_p & Z_p & 1 \end{bmatrix}^T = A_1 \cdot A_2 \cdot A_3 \cdot A_4 \cdot A_5 \cdot A_6 \cdot A_7 \cdot vec \tag{2.6}$$

Among them

$$A_i = \begin{bmatrix} cos\Theta_i & 0 & -sin\Theta_i & 0 \\ sin\Theta_i & 0 & cos\Theta_i & 0 \\ 0 & -1 & 0 & d_i \\ 0 & 0 & 0 & 1 \end{bmatrix} (i = 1,3,5,7) \tag{2.7}$$

$$A_i = \begin{bmatrix} cos\Theta_i & 0 & sin\Theta_i & -l_i cos\Theta_i \\ sin\Theta_i & 0 & -cos\Theta_i & -l_i sin\Theta_i \\ 0 & 1 & 0 & 0 \\ 0 & 0 & 0 & 1 \end{bmatrix} (i = 2,4,6) \tag{2.8}$$

$$vec = [0 \ 0 \ 0 \ 1]^T$$

$$\Theta_i = \theta_i + \theta_{i0} (i = 1,2,3,..7)$$

Equation (2.6) is the measurement equation of an articulated coordinate measuring machine. However, the equation only contains the parameters with a nominal value of non-zero in the structural parameters of the measuring machine, and the geometric relationship between the adjacent joint axes is considered to be perpendicular, that is, the two axes have a common point, and the angle between the two lines is a right angle, which is impossible to achieve in the process of real machining and assembly. Therefore, equation (2.7) can only represent the basic principle of the measuring machine. In fact, the A matrix given by equation (2.6) contains 4 parameters, and the accuracy of the measured coordinate values can only be guaranteed when all 4 parameters are accurately determined. Therefore, a more accurate measurement equation is given by the following formula:

$$\begin{bmatrix} X_p \\ Y_p \\ Z_p \\ 1 \end{bmatrix} = \prod_{i=1}^{7} \begin{bmatrix} cos\Theta_i & -sin\Theta_i cos\alpha_i & sin\Theta_i sin\alpha_i & l_i cos\Theta_i \\ sin\Theta_i & cos\Theta_i cos\alpha_i & -cos\Theta_i sin\alpha_i & l_i sin\Theta_i \\ 0 & sin\alpha_i & cos\alpha_i & d_i \\ 0 & 0 & 0 & 1 \end{bmatrix} \begin{bmatrix} 0 \\ 0 \\ 0 \\ 1 \end{bmatrix} \quad (2.9)$$

Equation (2.9) is the final measurement equation of the articulated coordinate measuring machine. As can be seen from equation (2.9), the conversion matrix for each member contains 4 parameters, and the measuring machine has a total of 28 parameters. One of these 28 parameters has a different meaning than the others. Suppose that:

$$A^7 = \prod_{i=1}^{7} \begin{bmatrix} cos\Theta_i & -sin\Theta_i cos\alpha_i & sin\Theta_i sin\alpha_i & l_i cos\Theta_i \\ sin\Theta_i & cos\Theta_i cos\alpha_i & -cos\Theta_i sin\alpha_i & l_i sin\Theta_i \\ 0 & sin\alpha_i & cos\alpha_i & d_i \\ 0 & 0 & 0 & 1 \end{bmatrix} \quad (2.10)$$

The articulated arm CMM will give the posture A^7 and position P of the arm. Position can be used for detecting the calibration board and the posture A^7 will be used to replace the function of the marker points of the multi-lines structured light needed.

2.2 single-line 3D reconstruction model

P is a point in the laser line shown in Fig.2.5 and P coordinate in the world system is (X_w, Y_w, Z_w). The world coordinate system can determine the real 3D coordinates of the space where the measured object is located, and when reconstructing the measured object, the system can be used as a container for its 3D coordinates to hold the 3D coordinates of the reconstructed object. The camera coordinate system $O_c X_c Y_c Z_c$ uses the camera itself as the spatial coordinate system. The camera coordinate system has its own optical center as the coordinate origin, where the Z axis is parallel to the camera optical axis. It has a direct connection with the world coordinate system, and the measured object in the world coordinate system first needs to go through the rigid body transformation to the camera coordinate system, and then to the image

coordinate system, where the rigid body transformation includes rotation and translation. The image coordinate system OXY and pixel coordinate system ouv are established based on the 2D image taken by the camera. The origin of the coordinate system (X, Y) is located at the focal point $O(u_0, v_0)$ of the camera's optical axis and the imaging plane, which is the primary point position, which is in units of length (mm).

The P in world coordinate system (X_w, Y_w, Z_w) project to the camera coordinate system (X_c, Y_c, Z_c) is as follows:

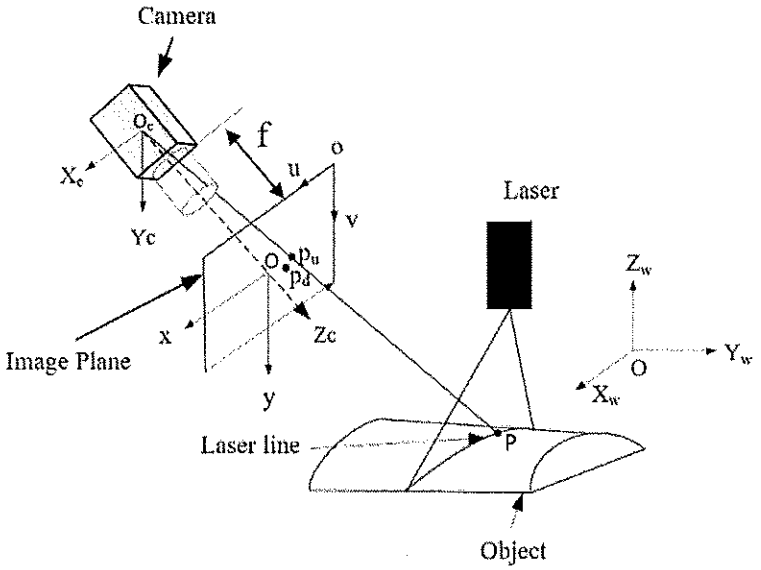

Fig.2.5 single-line 3D reconstruction model

$$\begin{bmatrix} X_c \\ Y_c \\ Z_c \end{bmatrix} = \begin{bmatrix} r_1 & r_2 & r_3 \\ r_4 & r_5 & r_6 \\ r_7 & r_8 & r_9 \end{bmatrix} \begin{bmatrix} X_w \\ Y_w \\ Z_w \end{bmatrix} + \begin{bmatrix} t_x \\ t_y \\ t_z \end{bmatrix} \tag{2.11}$$

$$R = \begin{bmatrix} r_1 & r_2 & r_3 \\ r_4 & r_5 & r_6 \\ r_7 & r_8 & r_9 \end{bmatrix} \tag{2.12}$$

$$T = \begin{bmatrix} t_x \\ t_y \\ t_z \end{bmatrix} \tag{2.13}$$

R stands for rotation matrix and T stands for translation matrix. $R$and T are independent of the camera. These two parameters are called the outer parameters of the camera.

Pin hole imaging model is the most common model in geometric analysis, and the camera model uses the principle of pin hole image, which belongs to the internal parameters of the camera, according to the triangle similarity, P in image coordinate system P_u can be obtained:

$$P_u = \begin{bmatrix} x_u \\ y_u \end{bmatrix} = \begin{bmatrix} \frac{X_c}{Z_c} \\ \frac{Y_c}{Z_c} \end{bmatrix} \tag{2.14}$$

The pixel coordinates of P_u on the camera p_u are:

$$\begin{bmatrix} u_u \\ v_u \\ 1 \end{bmatrix} = \begin{bmatrix} \frac{f}{dx} & 0 & u_0 \\ 0 & \frac{f}{dy} & v_0 \\ 0 & 0 & 1 \end{bmatrix} \begin{bmatrix} x_u \\ y_u \\ 1 \end{bmatrix} \tag{2.15}$$

Where dx and dy are the sizes of the CMOS cell alone X and Y direction respectively, and f is the focal length of the camera.

The errors in the manufacturing and assembly process of the camera optical system, have impacts on the image. We call it distortion. Distortion can be divided into two types: radial distortion and tangential distortion. Radial distortion is caused by changes in the curvature of the lens, while tangential distortion is mainly caused by the non-collinearity of the center line of multiple lenses during the assembly of the lens. Based on the mathematical model of these two distortions [39-40], a total aberration model can be built. Errors $\delta_x(x_u, y_u)$ alone horizontal direction and $\delta_x(x_u, y_u)$ along vertical direction are:

$$\begin{cases} \delta_x(x_u, y_u) = x_u(k_1\rho^2 + k_2\rho^4 + k_3\rho^6) + 2p_1x_uy_u + p_2(3x_u^2 + y_u^2) \\ \delta_y(x_u, y_u) = y_u(k_1\rho^2 + k_2\rho^4 + k_3\rho^6) + 2p_2x_uy_u + p_1(x_u^2 + 3y_u^2) \end{cases} \tag{2.16}$$

where, $\rho = \sqrt{(x_u^2 + y_u^2)}$,$k_1, k_2,\ k_3, p_1, p_2$ refer to the coefficients for radial distortion and tangential distortion, respectively. The relationship between the ideal image coordinates P_u and actual image coordinates $P_d(x_d, y_d)$ for spatial points is:

$$\begin{cases} x_d = x_u + \delta_x(x_u, y_u) \\ y_d = y_u + \delta_y(x_u, y_u) \end{cases} \tag{2.17}$$

The actual pixel coordinates of P_d on the camera p_d are

$$\begin{bmatrix} u \\ v \\ 1 \end{bmatrix} = \begin{bmatrix} f_x & 0 & u_0 \\ 0 & f_y & v_0 \\ 0 & 0 & 1 \end{bmatrix} \begin{bmatrix} x_d \\ y_d \\ 1 \end{bmatrix} \tag{2.18}$$

where $f_x = \frac{f}{dx}$ and $f_y = \frac{f}{dy}$.

Suppose the equation of the light plane of the laser in the camera coordinate system is:

$$aX + bY + cZ + D = 0 \tag{2.19}$$

Putting equation (2.14) into equation (2.19), we obtain:

$$ax_uZ_c + by_uZ_c + cZ_c + D = 0 \tag{2.20}$$

P is solved for the camera coordinate system as follows:

$$\begin{cases} Z_c = -\mathrm{D}/(ax_u + by_u + c) \\ X_c = x_uZ_c \\ Y_c = y_uZ_c \end{cases} \tag{2.21}$$

2.3 System Calibration

2.3.1 Camera calibration

2.3.1.1 Coordinate extraction of calibration target points

The calibration target is circular array calibration plate shown in figure 2.6. In the process of calibration, world target point extraction, edge detection is required first. The so-called edge refers to a collection of pixel points. The gray value of pixels around these pixels changes sharply in a certain direction, thus forming an obvious edge pixel band, which is also the most basic feature of image. In many edge extraction algorithms, Canny edge extraction algorithm has a strong anti-interference ability, can be applied to most of the application environment, it uses the double threshold algorithm to detect and connect the edge, can extract most effective edge information in the image, so this paper chooses Canny edge detection algorithm to extract the target edge information in the image. Since there are more or less some noise points in an image, it is necessary to carry out de-dryness processing before edge extraction of the image. Among them, Gaussian noise will affect the operation of first-order partial derivative of gray value. Therefore, it is necessary to first use Gaussian filter operator to process the image, and then use the finite difference operator of first-order partial derivative to calculate the gradient amplitude and gradient direction. Then, it is necessary to refine the ridge band in the amplitude image to keep the point with the largest local amplitude change. Finally, Canny operator is used to detect the effective edge information, so as to obtain the final edge detection graph. Since the marks used in this paper are black and white circular marks with obvious color contrast, the edges are relatively easy to identify. However, the projection shape of the circular edges captured by the camera is oval, so the location of the marks can be realized only by determining the center of the ellipse. There are many kinds of ellipse extraction algorithms, including least square fitting, Hough transform, genetic algorithm and so on. It is necessary to find a accurate ellipse extraction algorithm. Hough transform algorithm is fast, but the extraction accuracy is not high, while genetic algorithm has a high accuracy, but the algorithm complexity is relatively high, the speed is relatively slow, and cannot meet the real-time requirements. Through comprehensive comparison, The least squares algorithm can extract the ellipse accurately, and its complexity is low and its speed is fast. Therefore, the least squares algorithm is chosen to fit the ellipse in this paper.

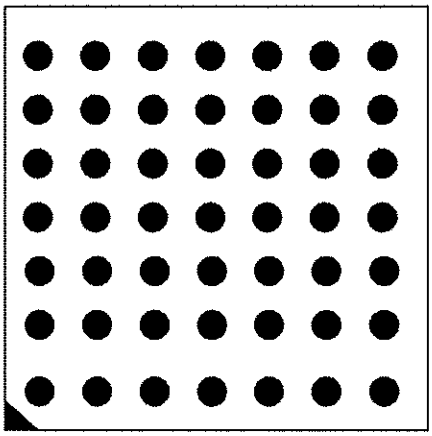

Fig.2.6 Circular array calibration plate

The least squares ellipse fitting was carried out for the edge image coordinate points extracted by Canny edge contour, and the image coordinates p_i $(u_i, v_i)$of the extracted ellipse contour were assumed to be:

$$p_i = [u_i \ \ v_i]^T \tag{2.22}$$

Get the vector *F(P)*

$$F(P) = [u^2 \ uv \ v^2 \ u \ v \ 1]^T \tag{2.23}$$

Assuming that

$$f(p, \beta) = F^T\beta = au^2 + buv + cv^2 + du + ev + f = 0 \tag{2.24}$$

where $f(p, \beta)$ is the implicit equation of the ellipse, u, v is a point in equation of ellipse and β is its parameter vector

$$\beta = [a \ \ b \ c \ d \ e \ f]^T \tag{2.25}$$

The process of least squares fitting is to find the parameter set and determine the data point with the best distance fitting between the ellipse. The objective function is as follows:

$$\sum_{i=1}^{N}[D(p_i, \beta)]^2 \rightarrow min \tag{2.26}$$

where $D(p_i, \beta)$represents different forms of distance. In this paper, algebraic distance is used to transform the elliptic least squares fitting problem into a linear problem. In order to avoid having no solution to the equation, the parameter β in f of (2.25) is set to 1. The minimum expression of the elliptic least squares fitting method based on algebraic distance is as follows:

$$\sum_{i=1}^{N}[p_i^T, \beta]^2 \tag{2.27}$$

Among them:

$$p_i = [u_i^2 \ u_i v_i \ v_i^2 \ u_i \ v_i \ 1]^T \tag{2.26}$$

According to the above steps, the best fitting ellipse expression can be solved to obtain the center of the subpixel ellipse.

2.3.1.2 Camera parameters calibration

The method of Zhang Zhengyou's[41] two-step calibration combines the moving plane template and the one-dimensional calibration object. It can not only ensure high calibration accuracy, but also reduce the dependence on experimental equipment. This calibration method can be divided into two steps:

(1) Ignore the influence of lens distortion, and use the linear model to obtain the internal and external parameters of the camera;

(2) Considering the distortion of the camera, take the obtained camera parameters as initial values and substitute them into the nonlinear standard.

To get the initial values.

First, according to the 3D reconstruction model, we know:

$$s\begin{bmatrix} u \\ v \\ 1 \end{bmatrix} = A\left[\vec{r_1}\ \ \vec{r_2}\ \ \vec{r_3}\ \vec{t}\right]\begin{bmatrix} X_w \\ Y_w \\ Z_w \\ 1 \end{bmatrix} \tag{2.27}$$

Where $\vec{r_1} = [r_1\ r_4\ r_7]^T, \vec{r_2} = [r_2\ r_5\ r_8]^T\ \vec{r_3} = [r_3\ r_6\ r_9]^T$ and $\vec{t} = \left[t_x\ t_y\ t_z\right]^T$.

Since the calibration plate is a two-dimensional plane. Without loss of generality, we assume the model plane is on $Z_w = 0$ of the world coordinate system. Formula (2.27) can be rewritten as:

$$s\begin{bmatrix} u \\ v \\ 1 \end{bmatrix} = A\left[\vec{r_1}\ \ \vec{r_2}\ \ \vec{r_3}\ \vec{t}\right]\begin{bmatrix} X_w \\ Y_w \\ 0 \\ 1 \end{bmatrix} = A\left[\vec{r_1}\ \ \vec{r_2}\ \ \vec{t}\right]\begin{bmatrix} X_w \\ Y_w \\ 1 \end{bmatrix} \tag{2.28}$$

The above formula can be rewritten as:

$$sm' = HM' \tag{2.29}$$

Among them $M' = [X_w\ \ Y_w\ 1]^T, m' = [u\ \ v\ \ 1]^T, H = [h_1\ h_2\ \ h_3\ ] = A\left[\vec{r_1}\ \ \vec{r_2}\ \ \vec{t}\right]$

As can be seen from the above equation, only enough target points are needed to solve the matrix H. Assuming that the matrix H has been solved, equation (2.28) can be written as follows:

$$\begin{cases} h_1 = A\vec{r_1} \\ h_2 = A\,\vec{r_2} \\ h_3 = A\vec{t} \end{cases} \tag{2.30}$$

The column vectors of the rotation matrix R have the identity and orthogonality, so the following constraint equation can be obtained

$$\begin{cases} h_1^T A^{-T} A^{-1} h_2 = 0 \\ h_1^T A^{-T} A^{-1} h_1 = h_2^T A^{-T} A^{-1} h_2 \end{cases} \tag{2.31}$$

Suppose $A^{-T}A^{-1}$ is matrix B. So we have:

$$B = A^{-T}A^{-1} = \begin{bmatrix} B_{11} & B_{12} & B_{13} \\ B_{12} & B_{22} & B_{23} \\ B_{13} & B_{23} & B_{33} \end{bmatrix} \tag{2.32}$$

Make

$$b = [B_{11}\ B_{12}\ B_{13}\ B_{22}\ B_{23}\ B_{33}]^T$$

Then the i^{th}column vector in the matrix H is $h_i = [h_{i1}\ h_{i2}\ h_{i3}]^T$, so:

$$h_i^T B h_j = v_{ij}^T b \tag{2.33}$$

Among them

$$v_{ij} = \left[h_{i1}h_{j1}\ \ h_{i1}h_{j2} + h_{i2}h_{j1}\ \ h_{i2}h_{j2}\ \ h_{i3}h_{j1} + h_{i1}h_{j3}\ h_{i3}h_{j2} + h_{i2}h_{j3}\ h_{i3}h_{j3}\right]^T$$

In this way, homogeneous equations containing unknown vector b can be obtained as follows:

$$\begin{bmatrix} v_{12}^T \\ (v_{12} - v_{22})^T \end{bmatrix} b = 0 \tag{2.34}$$

After b was obtained, A^{-1}could be solved using the method of Cholesky decomposition matrix. Finally, A was obtained by the inverse of A^{-1}. If A and $A^{-1}$are solved accurately, then the external parameters of each image can be solved easily.

$$\begin{cases} \overrightarrow{r_1} = \lambda A^{-1} h_1 \\ \overrightarrow{r_2} = \lambda A^{-1}\ h_2 \\ \overrightarrow{r_3} = \overrightarrow{r_1} \times \overrightarrow{r_2} \\ \vec{t} = \lambda A^{-1}\ h_3 \end{cases} \tag{2.35}$$

where $\lambda = \frac{1}{|A^{-1}\ h_1|} = \frac{1}{|A^{-1}\ h_2|}$.

A camera usually exhibits significant lens distortion, especially radial distortion.

From the equations (2.16) and (2.17), we can get:

$$\begin{bmatrix} x_d \\ y_d \end{bmatrix} = (1 + k_1 p^2 + k_2 p^4) * \begin{bmatrix} x_u \\ y_u \end{bmatrix} + \begin{bmatrix} 2p_1 x_u y_u + p_2(\rho^2 + 2{x_u}^2) \\ 2p_2 x_u y_u + p_1(\rho^2 + 2{y_u}^2) \end{bmatrix} \tag{2.36}$$

change to:

$$\begin{bmatrix} x_u\rho^2 & x_u\rho^4 & 2x_u y_u & 3{x_u}^2 + {y_u}^2 \\ y_u\rho^2 & y_u\rho^4 & {x_u}^2 + 3{y_u}^2 & 2x_u y_u \end{bmatrix} K = \begin{bmatrix} x_d - x_u \\ y_d - y_u \end{bmatrix} \tag{2.37}$$

$K = [k_1 \quad k_2 \quad p_1 \quad p_2]^T$ is a column vector of 1×4, equation (2.37) can be written as a matrix form $LK=F$. When there are N calibration points, L is a matrix of $2N\times4$, F is a column vector of $2N\times1$, and the vector K can be obtained according to the least squares:

$$K = (L^T L)^{-1} L^T F \tag{2.38}$$

Through the above process, we can obtain the internal A and external R, t parameters and distortion coefficients K of the camera, and use these camera parameters as the initial values to establish the optimization objective function.

$$\min \sum_{i=1}^{N1} \sum_{j=1}^{N2} \left| m_{ij} - \hat{m}_{ij}(A, k_1, k_2, p_1, p_2, R_i, t_i, M_{ij}) \right|^2 \tag{2.39}$$

Using Levenberg-Marquardt algorithm to optimize the objective function, we can obtain the optimization solution of the camera internal and external parameters and the distortion coefficients. $\hat{m}_{ij}(A, k_1, k_2, p_1, p_2, R_i, t_i, M_{ij})$ is the world coordinate M_{ij} of the j^{th} center of the circle on the calibration board and the pixel coordinate obtained by the camera nonlinear model. m_{ij} is the pixel coordinates of the center of the circle obtained by circle detection.

2.3.2 Laser plane calibration

2.3.2.1 light center extraction

The laser beam emitted by the laser projector shines on the surface of the measured object, forming a light bar pattern. The brightness of this laser light bar gradually decreases from the center of the laser to the edge of the light bar, generally showing a Gaussian distribution [42], and its mathematical expression can be expressed as:

$$G(x) = \frac{A}{\sqrt{2\pi\sigma}} e^{\left[-\frac{(x-u)^2}{2\sigma^2}\right]} \tag{2.40}$$

In equation (2.40), A represents the amplitude, which represents the height of the curve, σ represents the standard deviation, which represents the span of the curve, and u represents the mean, which represents the center of the laser light bar.

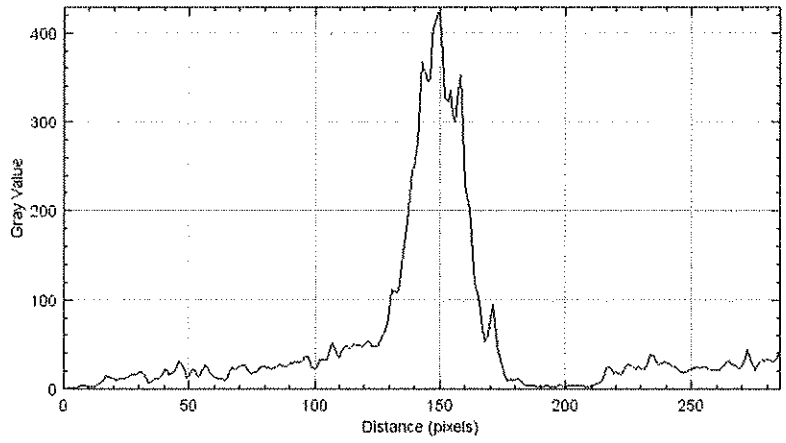

Fig.2.7 Distribution of gray value

In actual measurement, due to many factors, such as material uniformity, light transmittance, color, shape and surface roughness of the measured object, the reflectivity of light intensity is not the same everywhere on the surface of the measured object. These lead to asymmetry in the distribution of gray value of the laser light bar on the image (see Fig.2.7, the gray value is coded by 10bit of the camera), the non-normal distribution [43]. This brings great difficulties to the accurate extraction of the laser light strip center. It is also a major concern for most scholars in China and abroad during their research for years.

During laser 3D measurement, the smallest unit of a CCD camera plane is pixel. However, amid the shooting, the width of the laser light bar captured on the image can reach more than ten or even twenty pixels, so we must convert the light bar with a certain width into a single-pixel width center line so as to accurately obtain the corresponding light plane coordinates. We

call this process the extraction of laser light bar center. During laser 3D measurement, a camera is used to photograph the object which contains laser light strips. In the 2D image, there is a certain pixel width with the laser light stripes. In order to reconstruct the laser light strips accurately, we need to refine them, that is, extracting the center of laser light strips.

Many scholars in China and abroad have conducted research on the extraction algorithms of laser light stripe center, and there are three main common extraction algorithms [44]: the first is a threshold-based laser light stripe geometric center extraction method; the second is laser light strip energy center extraction method based on grayscale center of gravity; The third method is laser light stripe center extraction method based on direction template. Among the three methods, the first method is simple, but the accuracy is susceptible to edge detection. The second method is faster, but it is easily affected by environment and noises [45], The third method has strong noise resistance and can repair some light bar fractures, but it needs much calculating and the accuracy is coarse. Since the center coordinates of the laser light strip obtained through the second method can only reach the pixel level, we need to further obtain the subpixel center of the laser light stripe with higher precision, which can be solved by using the Hessian matrix:

$$H(x,y) = \begin{bmatrix} \frac{\partial^2 g(x,y)}{\partial x^2} & \frac{\partial^2 g(x,y)}{\partial x \partial y} \\ \frac{\partial^2 g(x,y)}{\partial x \partial y} & \frac{\partial^2 g(x,y)}{\partial y^2} \end{bmatrix} \otimes C(x,y) = \begin{bmatrix} r_{xx} & r_{xy} \\ r_{yx} & r_{yy} \end{bmatrix} \tag{2.41}$$

where $g(x,y)$ is the 2D gaussian kernel with standard deviation, $C(x,y)$ is the image and r_{xx}, r_{xy}, r_{xy}, r_{yy} are the partial derivatives.

Laser light plane equation can be calculated after we got the pixel coordinates of the laser center.

2.3.2.2 Laser light plane equation

At present, the main calibration methods of laser optical plane include wire drawing method [46], serrated target method [47] and calibration method based on double intersection ratio invariant [48]. Wire drawing method is to project the laser light plane on several different surface filaments, the light plane and the filaments intersect to form bright spots, calculate the three-dimensional coordinates of these bright spots, and then extract the center coordinates of these bright spots from the image, according to the corresponding relationship can complete the calibration of laser light plane, this method has high requirements for equipment and operation, and can be used for calibration of the number of feature points is limited. The serrated target method is similar to the wire drawing method. The serrated target is fixed on the moving platform, and the intersection of the laser optical plane and the serrated target forms a polyline. The turning point of the polyline is the intersection point of the serrated prism and the laser

optical plane. Cannot be used in field calibration. In this paper, the calibration method based on double intersection ratio invariance is used to find multiple collinear points on the calibration board, and the single-line laser is projected on the calibration board. The corresponding image containing laser light strips is collected by the camera. The intersection point of the line where the laser light strips are located and the line where the collinear points are located is solved by using the intersection ratio invariance characteristics, so as to complete the calibration of the single-line laser light plane.

Light plane calibration is the process of determining the position between the light plane and the camera, that is, obtaining the parameters of the light plane equation under the camera coordinate system. The calibration model of the light plane equation is shown in figure 2.8. L is the light stripe projected by the light plane on the plane target, and the P is a point on the light stripe L. Using the calibrated camera imaging model and the center coordinate extracted on the calibration board, we can get the camera coordinates of the light strip point. Set the camera coordinate of the i^{th} point on the j^{th} light stripe image to $P_{ci}^{j} = (X_{ci}^{j}, Y_{ci}^{j}, Z_{ci}^{j})$.

The equation (2.19) divide by -D for the sake of simplicity, the equation for the spatial plane of the light plane in the camera coordinate system is:

$$aX + bY + cZ - 1 = 0 \tag{2.42}$$

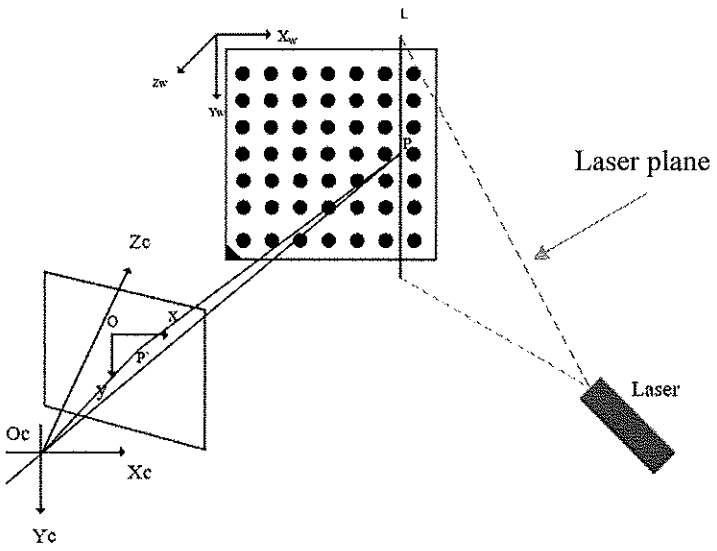

Fig.2.8 Calibrate Laser Plane

Put the camera coordinates of the center point of the light stripe into the equation (2.42) and write it as a matrix:

$$\begin{bmatrix} X_{c1}^{1} & Y_{c1}^{1} & Z_{c1}^{1} \\ \vdots & \vdots & \vdots \\ X_{ci}^{j} & Y_{ci}^{j} & Z_{ci}^{j} \\ \vdots & \vdots & \vdots \\ X_{cK}^{N} & X_{cK}^{N} & X_{cK}^{N} \end{bmatrix} \begin{bmatrix} a \\ b \\ c \end{bmatrix} = \begin{bmatrix} 1 \\ 1 \\ \vdots \\ 1 \end{bmatrix} \tag{2.43}$$

In the equation, N is the number of light stripe image frames obtained by rotating the target, and K is the number of points on each light stripe. Use least squares to solve over-determined equations and we get:

$$\begin{bmatrix} a \\ b \\ c \end{bmatrix} = \begin{bmatrix} \sum_{j=1}^{N}\sum_{i=1}^{K} X_{ci}^{j2} & \sum_{j=1}^{N}\sum_{i=1}^{K} X_{ci}^{j} Y_{ci}^{j} & \sum_{j=1}^{N}\sum_{i=1}^{K} X_{ci}^{j} Z_{ci}^{j} \\ \sum_{j=1}^{N}\sum_{i=1}^{K} X_{ci}^{j} Y_{ci}^{j} & \sum_{j=1}^{N}\sum_{i=1}^{K} Y_{ci}^{j2} & \sum_{j=1}^{N}\sum_{i=1}^{K} Y_{ci}^{j} Z_{ci}^{j} \\ \sum_{j=1}^{N}\sum_{i=1}^{K} X_{ci}^{j} Z_{ci}^{j} & \sum_{j=1}^{N}\sum_{i=1}^{K} Y_{ci}^{j} Z_{ci}^{j} & \sum_{j=1}^{N}\sum_{i=1}^{K} Z_{ci}^{j2} \end{bmatrix} \begin{bmatrix} \sum_{j=1}^{N}\sum_{i=1}^{K} X_{ci}^{j} \\ \sum_{j=1}^{N}\sum_{i=1}^{K} Y_{ci}^{j} \\ \sum_{j=1}^{N}\sum_{i=1}^{K} Z_{ci}^{j} \end{bmatrix} \quad (2.44)$$

2.3.3 hand-eye calibration

2.3.3.1 traditional hand-eye calibration

The base coordinate system $O_bX_bY_bZ_b$ of the scanning system, in which the sensor is fixed at the end of the robot, is presented in figure 2.9. All measured data are converted to this coordinate system. The end-effector coordinate system is indicated as $O_tX_tY_tZ_t$, the coordinate system origin is located in the center of the end flange plate, the direction of the X-axis is opposite to the direction of the identify hole on the end flange plate, the Z-axis is perpendicular to the end-effector, and the Y-axis is established as right-handed rule. The laser sensor coordinate system $O_SX_SY_SZ_S$ is located on the laser plane; its X-axis is perpendicular to the laser plane. The tool placed at the end flange plate needs tool coordinate system to define its center point (TCP). Tool coordinate system is defined based on the end-effector coordinate system, which can be used to describe the motion of the robot along its axes. If a tool is worn or replaced,

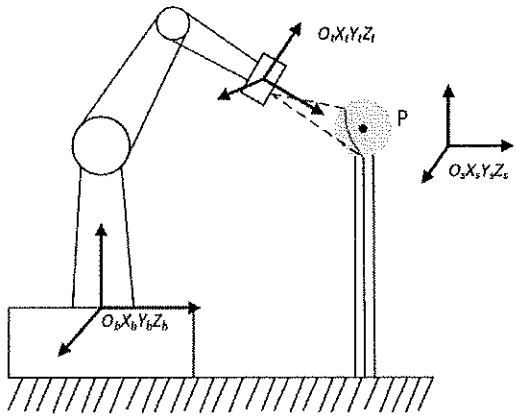

Fig.2.9 Laser scanner system based on robot

it only needs to redefine the tool coordinate system without any change of the program.

In traditional hand-eye calibration [49] is to determine the rotation matrix $R_s$and translation $T_s$between the laser sensor and robot. We use the hole or sphere as reference through measuring a fixed point at different poses by a robot scanning system. Matrices R_s and T_s can be solved through constraint of the fixed space point. Due to errors of the robot itself, it is difficult to

achieve high accuracy, and two-step method described below is proposed.

For a fixed point P in the robot base coordinate system, the relationship between coordinate X_b in the robot base coordinate system and coordinate X_s in the laser sensor coordinate system is as follows:

$$\begin{bmatrix} X_b \\ 1 \end{bmatrix} = \begin{bmatrix} R_0 & T_0 \\ 0 & 1 \end{bmatrix} \cdot \begin{bmatrix} R_s & T_s \\ 0 & 1 \end{bmatrix} \cdot \begin{bmatrix} X_s \\ 1 \end{bmatrix} \tag{2.45}$$

Where X_b is the fixed point's coordinate (X_b, Y_b, Z_b) in the robot base coordinate system, X_s is the fixed point's coordinate (X_s, Y_s, Z_s) in the laser scanning sensor coordinate system. R_0 and T_0 are the rotation matrix and translation from $O_tX_tY_tZ_t$ to $O_bX_bY_bZ_b$. R_s and T_s are the rotation matrix and translation from $O_sX_sY_sZ_s$ to $O_tX_tY_tZ_t$.Equation (2.45) is expanded as follows:

$$X_b = R_0 \cdot R_s \cdot X_s + R_0 \cdot T_s + T_0 \tag{2.46}$$

Controlling the robot and making the laser sensor measure the same fixed point twice, we obtain the following equations:

$$\begin{cases} X_b = R_{01} \cdot R_s \cdot X_{s1} + R_{01} \cdot T_s + T_{01} \\ X_b = R_{02} \cdot R_s \cdot X_{s2} + R_{02} \cdot T_s + T_{02} \end{cases} \tag{2.47}$$

Because the posture of the robot remains unchanged during scanning (the motion with translation only robot controlled shown in figure2.10), that is, $R_{01} = R_{02} = R_0$ .From equation (2.47) we can get:

$$R_0 \cdot R_s \cdot (X_{s1} - X_{s2}) + T_{01} - T_{02} = 0 \tag{2.48}$$

Here, R_0 is an orthogonal matrix. Collecting several sets of experimental data, we have:

$$R_s[X_{s1} - X_{s2} \;\; X_{s1} - X_{s3} \;\; \dots \;\; X_{s1} - X_{sn}] = R_0^T[T_{02} - T_{01} \;\; T_{03} - T_{01} \;\; \dots \;\; T_{0n} - T_{01}] \tag{2.49}$$

Making $A = [X_{s1} - X_{s2} \;\; X_{s1} - X_{s3} \;\; \dots \;\; X_{s1} - X_{sn}]$, $b = R_0^T[T_{02} - T_{01} \;\; T_{03} - T_{01} \;\; \dots \;\; T_{0n} - T_{01}]$ Equation (2.49) can be written as $R_sA = b$. We can use singular value decomposition method to solve this equation, that is:

$$R_s = UV^T \tag{2.50}$$

Here, V, U is right singular matrix and left singular matrix of Ab^T.Note that

$R_s = \begin{bmatrix} r_1 & r_2 & r_3 \\ r_4 & r_5 & r_6 \\ r_7 & r_8 & r_9 \end{bmatrix}$ is a rotation matrix and meets the following orthogonal constraints:

$$\begin{aligned} r_1^2 + r_2^2 + r_3^2 &= 1 \\ r_4^2 + r_5^2 + r_6^2 &= 1 \\ r_7^2 + r_8^2 + r_9^2 &= 1 \\ r_1 \cdot r_4 + r_2 \cdot r_5 + r_3 \cdot r_6 &= 0 \\ r_1 \cdot r_7 + r_2 \cdot r_8 + r_3 \cdot r_9 &= 0 \\ r_4 \cdot r_7 + r_5 \cdot r_8 + r_6 \cdot r_9 &= 0 \end{aligned}$$

Therefore, R_S only has three degrees of freedom. During the experiment, the sensor driven by the robot scans the standard sphere and obtains the centers of the several sections. R_S is solved via equation (2.40).

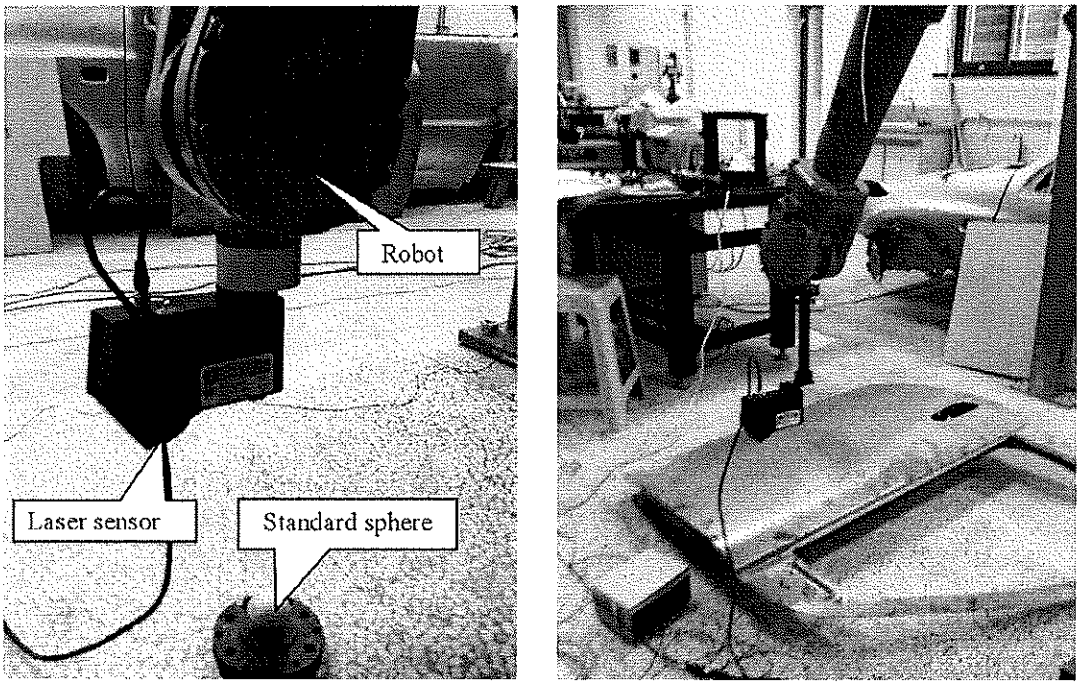

(a) Use sphere to calibrate (b) Use robot to scan

Fig.2.10 Laser scanner system based on robot
from the reference [49]

Using translation and rotation motion to scan a fixed sphere, with the coordinates of the laser sensor in $O_sX_sY_sZ_s$and equation (2.37), the coordinates under $O_bX_bY_bZ_b$ can be acquired, for two different points, we have

$$R_{01} \cdot R_s \cdot X_{s1} - R_{02} \cdot R_s \cdot X_{s2} + T_{01} - T_{02} = (R_{02} - R_{01}) \cdot T_s \quad (2.51)$$

Where R_{01} and T_{01} are the first postures the robot moved, R_{02} and T_{02} are the second postures the robot moved.

Change equation (2.51) to the follows:

$$T_s = (R_{02} - R_{01})^{-1}(R_{01} \cdot R_s \cdot X_{s1} - R_{02} \cdot R_s \cdot X_{s2} + T_{01} - T_{02}) \quad (2.52)$$

Traditional hand-eye calibration method for robot scanning system is not suitable for the articulated arm CMM. Because there is no servo motor inside the articulated arm, the articulated arm cannot be controlled like a robot, which can scan the standard ball only by the posture translation in space. Therefore, the translation matrix${}^t_sT$ cannot be obtained by using the method of standard ball in literature. Therefore, a fixed flat board is proposed to calibrate the relationship between the spatial position${}^t_sT$ and the attitude ${}^t_sR$ of the single-line structured light 3D camera and the articulated arm CMM. The fixed calibration plane has three advantages over the spherical calibration method:

(1) The articulated arm calibration process doesn't need to be like the traditional hand-eye calibration method to avoid the strict requirements of scanning posture.
(2) The accuracy of traditional hand-eye calibration method is affected by different scanning spheres, and this method is avoided by fixing the calibration plane.
(3) The cost of the plate with a certain flatness has an advantage over the cost of the ball with a certain accuracy.

2.3.3.2 plat board hand-eye calibration

Steps of hand-eye calibration via plat board are shown in Fig.2.11. We now derive the calibrated mathematical objective equation.

For a point P on the calibration plate plane, its coordinates in the measuring arm end-effector coordinate system and the linear structured light 3D camera coordinate system satisfy the following relationship:

$$\begin{bmatrix} P_t \\ 1 \end{bmatrix} = \begin{bmatrix} {}^t_bR & {}^t_bT \\ 0 & 1 \end{bmatrix} \begin{bmatrix} P_b \\ 1 \end{bmatrix} = \begin{bmatrix} {}^t_sR & {}^t_sT \\ 0 & 1 \end{bmatrix} \begin{bmatrix} P_s \\ 1 \end{bmatrix} \tag{2.53}$$

P_b is coordinate of point P of the calibration plate plane on the base coordinate system $O_bX_bY_bZ_b$, $P_b = [x_b \quad y_b \quad z_b]^T$. P_s is the coordinate of point P on the calibration plate plane in the coordinate system $O_sX_sY_sZ_s$, as follows:

$$P_s = [x_s \quad y_s \quad z_s]^T \tag{2.54}$$

${}^t_bR$ and ${}^t_bT$ represent the rotation matrix and shift vectors of the transformation from the coordinate system $O_bX_bY_bZ_b$ to the coordinate system $O_tX_tY_tZ_t$ which need to be solved during

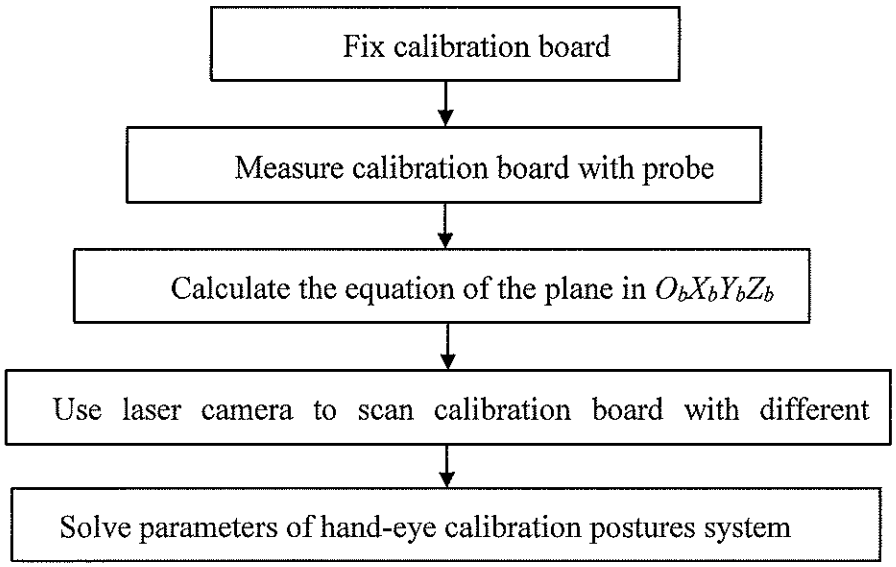

Fig.2.11 Steps for hand-eye calibration

calibration. P_t is coordinate of point P on the end-effector coordinate system $O_tX_tY_tZ_t$, $P_t = [x_t \quad y_t \quad z_t]^T$, the coordinates can be measured with contact probe to obtain calibration plate.

The plane equation of the calibration plate in the measuring arm base coordinate system $O_bX_bY_bZ_b$ is as follows:

$$[A_b\ B_b\ C_b\ D_b]\begin{bmatrix}P_b\\1\end{bmatrix} = 0 \tag{2.55}$$

The parameters$A_b, B_b, C_b, D_b$are parameters of the plane equation. Using the contact probe of the measuring arm to measure the 3D coordinates of a large number of calibration points on the calibration plate, and then using the least square fitting to obtain these parameters of the plane equation of the calibration plate. Transform the plane in equation (2.55) from the base coordinate system $O_bX_bY_bZ_b$ to the end-effector $O_tX_tY_tZ_t$:

$$[A_t\ B_t\ C_t\ \ D_t]\begin{bmatrix}P_t\\1\end{bmatrix} = 0 \tag{2.56}$$

The relationship between A_t, B_t, C_t, D_t and A_b, B_b, C_b, D_b in equation (2.54) is as follows:

$$\begin{bmatrix}A_t\\B_t\\C_t\end{bmatrix} = {}^t_bR\begin{bmatrix}A_b\\B_b\\C_b\end{bmatrix} \tag{2.57}$$

And the D_t expression is as follows:

$$D_t = D_b - [A_t\ B_t\ C_t]{}^t_bT \tag{2.58}$$

Equation (2.58) will be proved as follows:

$$\begin{bmatrix}{}^t_bR & {}^t_bT\\0 & 1\end{bmatrix} = \begin{bmatrix}r_1 & r_2 & r_3 & T_x\\r_4 & r_5 & r_6 & T_y\\r_7 & r_8 & r_9 & T_z\\0 & 0 & 0 & 1\end{bmatrix} \tag{2.59}$$

Point $Q_b = \left(0,0,-\frac{D_b}{C_b}\right)^T$ under coordinate system $O_bX_bY_bZ_b$ is on the plane, can be converted to under $O_tX_tY_tZ_t$ by equation:

$$Q_t = \begin{bmatrix}r_1 & r_2 & r_3 & T_x\\r_4 & r_5 & r_6 & T_y\\r_7 & r_8 & r_9 & T_z\\0 & 0 & 0 & 1\end{bmatrix}\begin{bmatrix}Q_s\\1\end{bmatrix} = \begin{bmatrix}-\frac{D_b}{C_b}r_3 + T_x\\-\frac{D_b}{C_b}r_6 + T_y\\-\frac{D_b}{C_b}r_9 + T_z\end{bmatrix} \tag{2.60}$$

Since $Q_t$is on the equation of (2.56), it has the following relation:

$$A_t\left(-\frac{D_b}{C_b}r_3 + T_x\right) + B_t\left(-\frac{D_b}{C_b}r_6 + T_y\right) + C_t\left(-\frac{D_b}{C_b}r_9 + T_z\right) + D_t = 0 \tag{2.61}$$

From (2.57) and (2.59) get:

$$\begin{bmatrix}A_t\\B_t\\C_t\end{bmatrix} = \begin{bmatrix}r_1A_b + r_2B_b + r_3C_b\\r_4A_b + r_5B_b + r_6C_b\\r_7A_b + r_8B_b + r_9C_b\end{bmatrix} \tag{2.62}$$

we can get:

$$D_t = \frac{D_b}{C_b}(A_t\, r_3 + B_t\, r_6 + C_t\, r_9) - A_t T_x - B_t T_y - C_t T_z$$

$$= \frac{D_b}{C_b}(r_1\, r_3 A_b + r_4\, r_6 A_b + r_7\, r_9 A_b)$$

$$+ \frac{D_b}{C_b}(+r_2\, r_3 B_b + r_5\, r_6 B_b + r_8\, r_9 B_b)$$

$$+ \frac{D_b}{C_b}(r_3\, r_3 C_b + r_6\, r_6 C_b + r_9\, r_9 C_b)$$

$$- A_t T_x - B_t T_y - C_t T_z \tag{2.63}$$

We know from the orthogonality of ${}^t_bR$:

$$r_1\, r_3 A_b + r_4\, r_6 A_b + r_7\, r_9 A_b + r_2\, r_3 B_b + r_5\, r_6 B_b + r_8\, r_9 B_b = 0 \tag{2.64}$$

$$r_3\, r_3 C_b + r_6\, r_6 C_b + r_9\, r_9 C_b = C_b \tag{2.65}$$

Equations (2.64) and (2.65) are substituted into equation (2.63) to obtain:

$$D_t = D_b - [A_t, B_t, C_t]\,{}^t_bT.$$

Substitute equation (2.53) into equation (2.56) to obtain:

$$[A_t\ B_t\ C_t\ D_t]\begin{bmatrix} {}^t_sR & {}^t_sT \\ 0 & 1 \end{bmatrix}\begin{bmatrix} P_s \\ 1 \end{bmatrix} = 0 \tag{2.66}$$

make:

$${}^t_sR = \begin{bmatrix} r_1 & r_2 & r_3 \\ r_4 & r_5 & r_6 \\ r_7 & r_8 & r_9 \end{bmatrix} \tag{2.67}$$

Notice that ${}^t_sR$ is the rotation matrix, which satisfies the orthogonality of matrices. ${}^t_sR\,{}^t_sR^T = E$, E is the identity matrix. As follows:

$$\begin{bmatrix} r_1 & r_2 & r_3 \\ r_4 & r_5 & r_6 \\ r_7 & r_8 & r_9 \end{bmatrix}\begin{bmatrix} r_1 & r_4 & r_7 \\ r_2 & r_5 & r_8 \\ r_3 & r_6 & r_9 \end{bmatrix} = \begin{bmatrix} 1 & 0 & 0 \\ 0 & 1 & 0 \\ 0 & 0 & 1 \end{bmatrix} \tag{2.68}$$

${}^t_sR$ can be represented by the roll angle φ of rotation about Z axis, and angle γ of rotation about Y axis, and angle θ of rotation about X axis, The three angles represent, as follows:

$${}^t_sR = \begin{bmatrix} r_1 & r_2 & r_3 \\ r_4 & r_5 & r_6 \\ r_7 & r_8 & r_9 \end{bmatrix}$$

$$= \begin{bmatrix} 1 & 0 & 0 \\ 0 & C\theta & -S\theta \\ 0 & S\theta & C\theta \end{bmatrix}\begin{bmatrix} C\gamma & 0 & S\gamma \\ 0 & 1 & 0 \\ -S\gamma & 0 & C\gamma \end{bmatrix}\begin{bmatrix} C\varphi & -S\varphi & 0 \\ S\varphi & C\varphi & 0 \\ 0 & 0 & 1 \end{bmatrix}$$

$$= \begin{bmatrix} C\gamma C\varphi & -C\gamma S\varphi & S\gamma \\ C\theta S\varphi + S\theta S\gamma C\varphi & C\theta C\varphi - S\theta S\gamma S\varphi & -S\theta C\gamma \\ S\theta S\varphi - C\theta S\gamma C\varphi & S\theta C\varphi + C\theta S\gamma S\varphi & C\theta C\gamma \end{bmatrix} \tag{2.69}$$

$C\gamma = cos\gamma, C\varphi = cos\varphi, C\theta = cos\theta, S\theta = sin\theta, S\gamma = sin\gamma,\ S\varphi = sin\varphi.$

Let the translation vector ${}_s^tT$:

$$ {}_s^tT = \left(t_x, t_y, t_z\right)^T \tag{2.70} $$

Equations (2.57), (2.58) and (2.69) are substituted into equation (2.56) to expand, and equation (2.61) can be obtained:

$$ A_t x_s r_1 + A_t y_s r_2 + A_t z_s r_3 + A_t t_x + $$

$$ B_t x_s r_4 + B_t y_s r_5 + B_t z_s r_6 + B_t t_y + $$

$$ C_t x_s r_7 + C_t y_s r_8 + C_t z_s r_9 + C_t t_z + D_t = 0 \tag{2.71} $$

Rewriting (2.71) into matrix form (2.72) is obtained:

$$ \left(\begin{bmatrix} A_t x_s \\ A_t y_s \\ A_t z_s \\ A_t \\ B_t x_s \\ B_t y_s \\ B_t z_s \\ B_t \\ C_t x_s \\ C_t y_s \\ C_t z_s \\ C_t \end{bmatrix}\right)^T {}_s^tX + D_t = 0 \tag{2.72} $$

${}_s^tX$ is the parameter required to solve the hand-eye calibration of the measuring arm and the linear structured light 3D camera, it also contains ${}_s^tR$ and ${}_s^tT$. Its expression is as follows (2.73):

$$ {}_s^tX = \begin{bmatrix} r_1 & r_2 & r_3 & t_x & r_4 & r_5 & r_6 & t_y & r_7 & r_8 & r_9 & t_z \end{bmatrix}^T = $$

$$ \begin{bmatrix} cos\gamma cos\varphi \\ -cos\gamma sin\varphi \\ sin\gamma \\ t_x \\ cos\theta sin\varphi + sin\theta sin\gamma cos\varphi \\ cos\theta cos\varphi - sin\theta sin\gamma sin\varphi \\ -sin\theta cos\gamma \\ t_y \\ sin\theta sin\varphi - cos\theta sin\gamma cos\varphi \\ sin\theta cos\varphi + cos\theta sin\gamma sin\varphi \\ cos\theta cos\gamma \\ t_z \end{bmatrix} \tag{2.73} $$

(2.73) is the target equation, assuming that the j point of the laser line obtained from the i^{th} scan on the calibration plate is $P_s^{ij} = \begin{bmatrix} x_s^{ij} & y_s^{ij} & z_s^{ij} \end{bmatrix}^T$ is substituted into 2.74:

$$H_{ij}\,{}_s^tX + D_t^i = 0 \tag{2.74}$$

$$H_{ij} = \left[A_t^i x_s^{ij}\ A_t^i y_s^{ij}\ A_t^i z_s^{ij}\ A_t^i\ B_t^i x_s^{ij}\ B_t^i y_s^{ij}\right.$$
$$\left. B_t^i z_s^{ij}\ B_t^i\ C_t^i x_s^{ij}\ C_t^i y_s^{ij}\ C_t^i z_s^{ij}\ C_t^i\right] \tag{2.75}$$

$A_t^i, B_t^i, C_t^i, D_t^i$ is the representation of the plane equation parameters A_b, B_b, C_b, D_b in the coordinate system $O_tX_tY_tZ_t$ measured by the contact probe under the i-th scanning attitude. Build the objective function.

$$F(\varphi, \gamma, \theta,\ t_x,\ t_y,\ t_z) = min \sum_{i=0}^{M} \sum_{j=0}^{N} \left| H_{ij}\,{}_s^tX + D_t^i \right|^2 \tag{2.76}$$

M is the number of scanning and N is the number of points of laser line on the plate for each scanning. The hand-eye calibration parameters ${}_s^tR$ and ${}_s^tT$ can be obtained from equation (2.73) by using nonlinear optimization algorithm.

2.4 Conclusion

This chapter introduces the working principle, physical structure and mathematical model of the articulated arm. To understand the coordinate system of hand-eye calibration, mathematical modeling is helpful. The hand-eye calibration section introduces the method of single-line structured light and hand-eye calibration of robot in the industry. Although the robot and the articulated arm have the same mathematical model, they have different working modes. This is mainly because the robot is driven by an internal motor, which can make the robot hover in the air and walk out of a specific track, while the articulated arm cannot move by itself. This paper innovatively proposed to rely on a plate for hand-eye calibration, and to build a mathematical model for hand-eye calibration based on the coplanar characteristics of points scanned under different posture scanning calibration plates.

Chapter 3 Cross-line scanning system

3.1 Hardware structure

To achieve rapid acquisition of the indicated contour of the measured object, we designed a set of cross-line structured light scanning systems based on the structured light three-dimensional vision measurement principle. Fig.3.1 shows a schematic diagram of the scanning system. For the single-line structured light A and single-line structured light B, the light planes are cross to each other, thus forming the cross-line structured light. The cross-line structured light and 2D camera are fixed together onto mounting plate, and the whole system is installed at the end of the measuring arm. The measuring arm and camera laser are connected to a computer through a USB interface, enabling unified control.

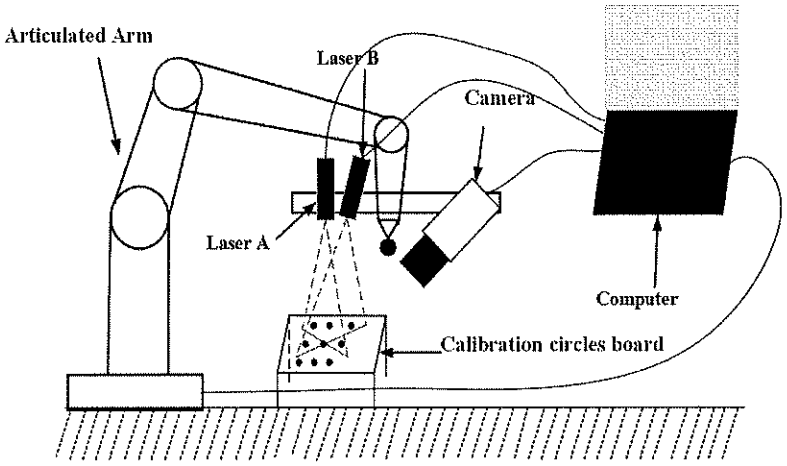

Fig.3.1 Schematic articulated arm-mounted cross-line structured

3.2 cross-line 3D reconstruction model

Fig.3.2 depicts the manner in which the two lasers are turned off and on periodically. Time denotes the time required for the camera to acquire a frame, which is aligned and synchronized in the hardware. Fig.3.3 shows the pictures captured by the camera when laser A, B and AB shoot on the plane.

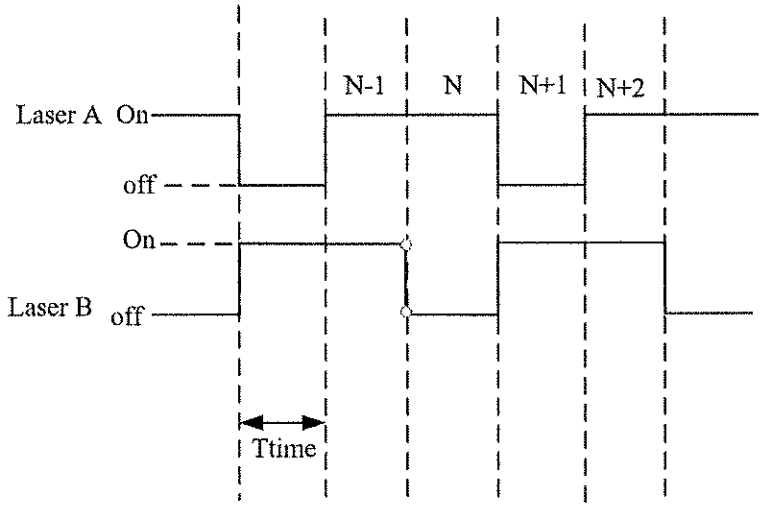

Fig.3.2 Cross-line laser work period

The direction of the line in the 2D image was estimated locally by computing the eigenvalues and eigenvectors of the Hessian matrix. The response of the ridge detector given by the value of the maximum absolute eigenvalue is a good indicator of the saliency of the extracted line points. As we need to compare the center light of the two frame, we used the gray center method. When laser A is turned on, the current frame is denoted by N and the center of the light bar was extracted from left to right and top to bottom. In the j^{th} column of the image, the light bar region is S. Then, the row is calculated as:

$$u_{jN}^{c} = \frac{\Sigma_{yes}\, gray(j,y)*y}{\Sigma_{yes}\, gray(j,y)} \tag{3.1}$$

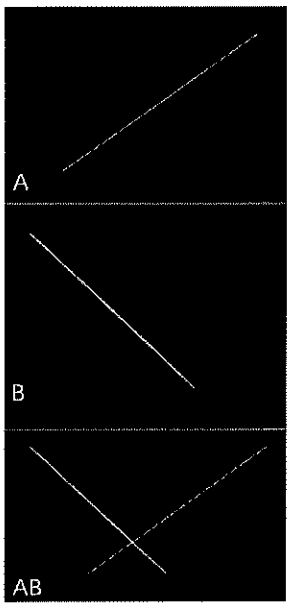

Fig.3.3 Laser A opened (top), laser B opened (middle), and laser AB

All the collected light bars are collectively denoted as:

$$U_N^C = \{u_{jN}^c\} \tag{3.2}$$

Similarly, when laser B is turned on, the current frame is $N+1$ and the light bar in the j^{th} column is located in region S. Similarly, the row is:

$$u_{jN+1}^c = \frac{\sum_{x \in S} gray(j,y) * y}{\sum_{x \in S} gray(j,y)} \tag{3.3}$$

The coordinates of all the collected light bars are denoted as follows:

$$U_{N+1}^C = \{u_{jN+1}^c\} \tag{3.4}$$

When lasers A and B are opened at the same time, light bars in all column directions are found. At this time, the frame is $N+2$ and the collected light bars are denoted as:

$$U_{N+2}^C = \{u_{jN+2}^c\} \tag{3.5}$$

The position of the light bar recorded by U_{N+2}^C in equation (3.5) is polysemous and needed to be distinguished, for which the following equation can be used:

$$\left|u_{jN+2}^c - u_{jN}^c\right| \leq T \tag{3.6}$$

And

$$\left|u_{jN+2}^c - u_{jN+1}^c\right| \leq T \tag{3.7}$$

In the comparison, T is the allowable threshold for extracting the optical bar position. If it matches equation (3.6), it is determined that the light strip belongs to laser A, and if it matches equation (3.7), then the strip belongs to laser B. If three pictures are captured by the camera, we can only obtain four sets of points with the cross-line laser compared to three sets of points obtained with the single-line laser. Through this method to improve the frame rate of the 3D points, the scanning frame rate increased to 1.33 times that with a single-line laser ideally.

3.3 hand-eye calibration

The cross-line is created by two single-line laser, so we can use the approach of 2.3.3.2 section to calibrate the relationship between camera and the end-of articulated arm CMM.

Chapter 4 Multi-lines scanning system

4.1 Hardware structure

We use two cameras and a multi-lines laser to build a multi-lines scanning system with articulated arm CMM shown in Fig 4.1Two 2D cameras and the laser are fixed together with a holder, the holder is mounted on the end-of the arm. The articulated arm, cameras and lasers are connected to a computer through a USB interface, enabling unified control.

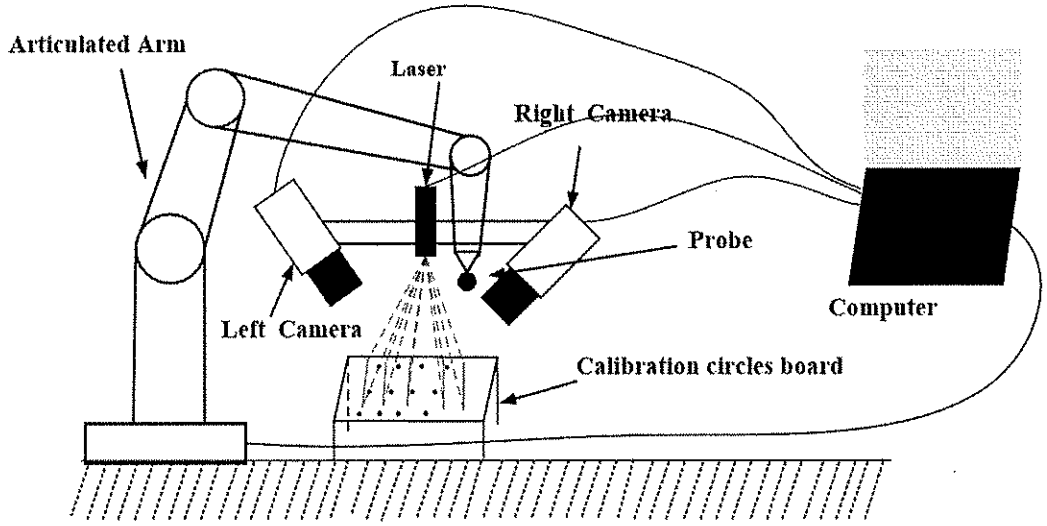

Fig.4.1 Schematic articulated arm-mounted multi-lines structured laser

4.2 3D reconstruction

The hand-hold 3D laser scanner needs to pick the marker point for 3D match. The marker point is reconstructed by the principle of binocular stereo vision.

4.2.1 Binocular reconstruction

Assuming that the world coordinate system coincides with the left camera coordinate system, $O_l X_l Y_l Z_l$ represents the left camera coordinate system, $O_l u_l v_l$ represents the image coordinate system, f_l represents the left camera focal length; $O_r X_r Y_r Z_r$ represents the right camera

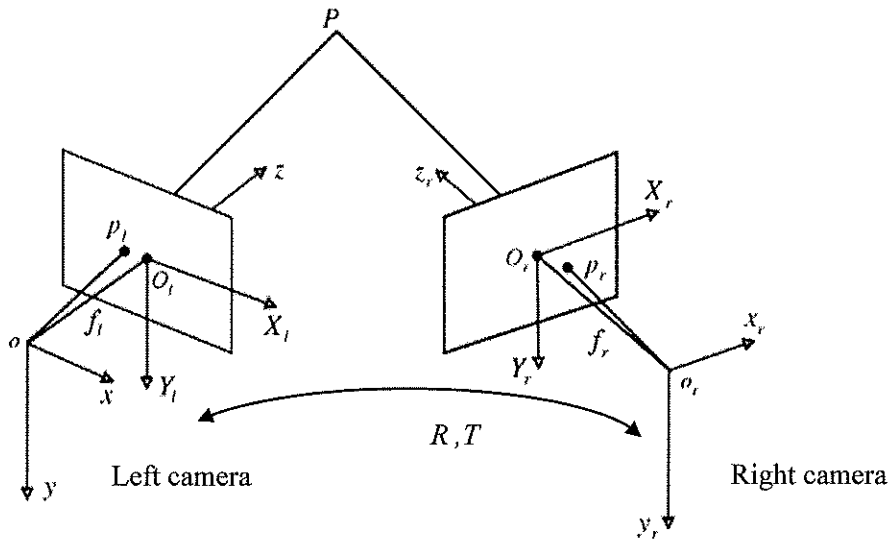

Fig.4.2 binocular stereo vision

coordinate system, $O_r u_r v_r$ represents the image coordinate system, and f_r represents the right camera focal length. P(X_l, Y_l, Z_l) is any point in space, and the coordinates of P point on the left and right cameras are $p_l(u_l, v_l)$ and $p_r(u_r, v_r)$ in the image coordinate system. The following relationship can be obtained by transforming the model from the camera perspective:

$$s_l \begin{bmatrix} u_l \\ v_l \\ 1 \end{bmatrix} = \begin{bmatrix} f_l & 0 & 0 \\ 0 & f_l & 0 \\ 0 & 0 & 1 \end{bmatrix} \begin{bmatrix} X_l \\ Y_l \\ Z_l \end{bmatrix} \tag{4.1}$$

$$s_r \begin{bmatrix} u_r \\ v_r \\ 1 \end{bmatrix} = \begin{bmatrix} f_r & 0 & 0 \\ 0 & f_r & 0 \\ 0 & 0 & 1 \end{bmatrix} \begin{bmatrix} X_r \\ Y_r \\ Z_r \end{bmatrix} \tag{4.2}$$

where $s_l = Z_l, s_r = Z_r$

There is a certain rotation and translation relationship between the left camera coordinate system and the right camera coordinate system, assuming that the rotation matrix is R and the translation vector is T , there is the following transformation relationship:

$$\begin{bmatrix} X_r \\ Y_r \\ Z_r \\ 1 \end{bmatrix} = \begin{bmatrix} R & T \\ 0 & 1 \end{bmatrix} \begin{bmatrix} X_l \\ Y_l \\ Z_l \\ 1 \end{bmatrix} = \begin{bmatrix} r_1 & r_2 & r_3 & t_x \\ r_4 & r_5 & r_6 & t_y \\ r_7 & r_8 & r_9 & t_z \\ 0 & 0 & 0 & 1 \end{bmatrix} \begin{bmatrix} X_l \\ Y_l \\ Z_l \\ 1 \end{bmatrix} \tag{4.3}$$

where

$$R = \begin{bmatrix} r_1 & r_2 & r_3 \\ r_4 & r_5 & r_6 \\ r_7 & r_8 & r_9 \end{bmatrix} \tag{4.4}$$

and

$$T = \begin{bmatrix} t_x \\ t_y \\ t_z \end{bmatrix} \tag{4.5}$$

By combining equations (4.1), (4.2) and (4.3), Equation (4.6) can be obtained:

$$s_r\begin{bmatrix}u_r\\v_r\\1\end{bmatrix}=\begin{bmatrix}f_r r_1 & f_r r_2 & f_r r_3 & f_r t_x\\ f_r r_1 & f_r r_1 & f_r r_6 & f_r t_y\\ r_7 & r_8 & r_9 & t_z\end{bmatrix}\begin{bmatrix}Z_l u_l/f_l\\ Z_l v_l/f_l\\ Z_l\\ 1\end{bmatrix} \tag{4.6}$$

Therefore, the 3D space point $P(X_l, Y_l, Z_l)$in the world coordinate system can be expressed as the following equations (4.7), so that binocular stereo reconstruction can be realized.

$$\begin{cases} X_l = \dfrac{Z_l u_l}{f_l} \\ Y_l = \dfrac{Z_l v_l}{f_l} \\ Z_l = \dfrac{f_l(f_r t_x - u_r t_z)}{u_r(r_7 u_l + r_8 v_l + r_9 f_l) - f_r(r_1 u_l + r_2 v_l + r_3 f_l)} \end{cases} \tag{4.7}$$

4.2.2 parallel multi-lines 3D reconstruction

P is a point in the laser line shown in Fig.4.3 and P image coordinate in the left camera system is (x_{ul}, y_{ul}),and from section 2.2, we know that P (X_{cl}, Y_{cl}, Z_{cl})coordinate in the left camera system is:

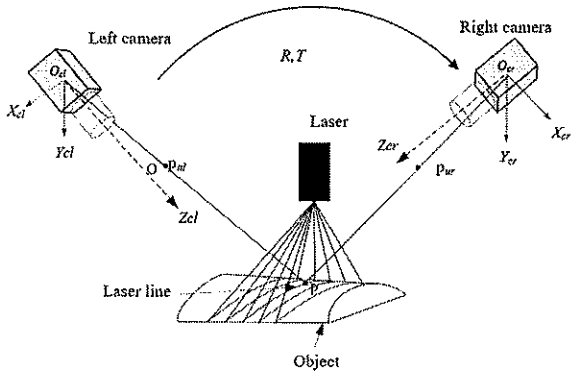

Fig.4.3 multi-lines 3D reconstruction

$$\begin{cases} X_{cl} = x_{ul} Z_{cl} \\ Y_{cl} = y_{ul} Z_{cl} \end{cases} \tag{4.8}$$

Suppose that the optical plane equation of the i^{th}laser in the left camera coordinate system is

$$A_i X + B_i Y + C_i Z + D_i = 0 \tag{4.9}$$

Equation (4.8) is substituted into the above equation as follows:

$$A_i x_{ul} Z_{cl} + B_i y_{ul} Z_{cl} + C_i Z_{cl} + D_i = 0 \tag{4.10}$$

Figure out the point P in the left camera coordinate system of the i^{th} laser line P_i^{lc} as follows:

$$\begin{cases} Z_i^{lc} = -D_i/(A_i x_{ul} + B_i y_{ul} + C_i) \\ X_i^{lc} = x_{ul} Z_i^{lc} \\ Y_i^{lc} = y_{ul} Z_i^{lc} \end{cases} \tag{4.11}$$

How to determine the laser plane, need to use the polar constraint.

The internal parameters of the left and right cameras are calibrated by Zhang's calibration method, and the coordinates of the point X_w in the world coordinate system to the left and right cameras are set asX_L and X_R, and transformed into R_R, T_L , R_R, T_R. There are:

$$X_L = R_L X_w + T_L \tag{4.12}$$

and

$$X_R = R_R X_w + T_R \tag{4.13}$$

Combined equation (4.12) and equation (4. 13) eliminates X_w to get:

$$X_R = R_R R_L^{-1} X_L + T_R - R_R R_L^{-1} T_L \tag{4.14}$$

The relation between the points in the left camera coordinate system and the right camera is:

$$R_{LR} = R_R R_L^{-1} \tag{4.15}$$

$$T_{LR} = T_R - R_R R_L^{-1} T_L \tag{4.16}$$

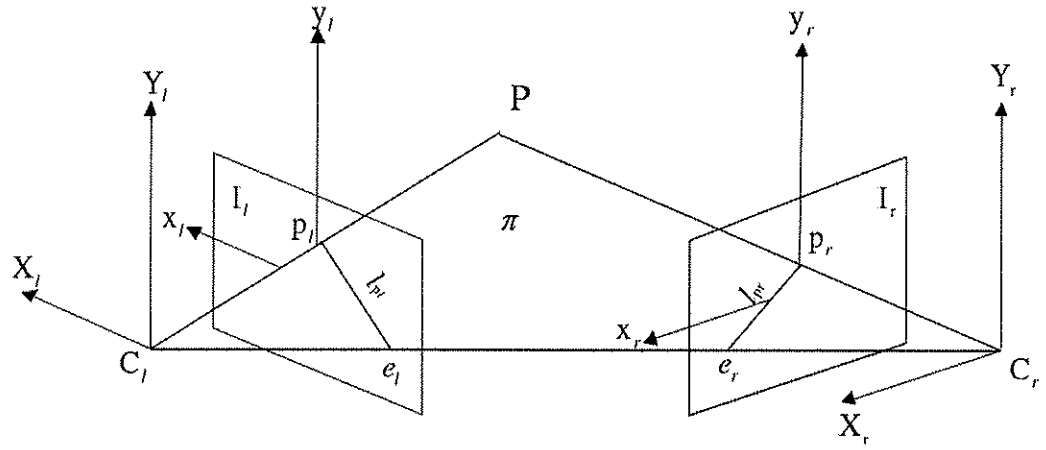

Fig.4.4 Epipolar constraint

As shown in Fig.4.4. The origin of the left and right camera coordinate systems is C_l and C_r respectively. Through any point P in the world coordinate system and the opposite polar plane is the plane π. The intersection line between the opposite polar plane and the left and right camera image plane is called the polar line, namely $e_l$and $e_r$in Fig. 4.4. The intersection point of the left pole $e_l$and $C_l P$ is p_l, which is the projection point formed by the three-dimensional space point P on the left camera image plane, while the intersection point pr of the stone pole

e_r and C_rP is the projection point formed by the three-dimensional space point P on the right camera image plane.

For the left camera, we assume that the projection point of three-dimensional point P in space on the left image plane is p_l, and three-dimensional point P in space is located on the ray with optical center C_l as the endpoint pointing to the projection point p_l. In addition, we cannot obtain other constraint information, so it is impossible to determine the depth of the dimension C_lP Therefore, the true position of three-dimensional point P in space cannot be determined. If a right view is added to consider, then the situation is quite different. Any three-dimensional point in C_lP corresponds to a unique point on the pole e_r in the right image. That is to say, we can use the corresponding relationship between the projection point p_l on the left image and the projection point $p_r$on the stone pole e_r to finally determine the specific position of the three-dimensional point P in space. Corresponding to a fixed point in space in the left and right camera projection is determined.

According to the transformation relation between left camera and right camera in equations (4.15) and (4.16), the coordinate P_i^{rc} in the coordinate system of right camera is:

$$P_i^{rc} = [X_i^{rc} \ Y_i^{rc} \ Z_i^{rc}]^T = R_{LR}P_i^{lc} + T_{LR} \tag{4.17}$$

In the case that the internal parameters of the right camera are known, the pixel coordinates of the right camera are converted by equations (4.17) :

$$p_i^r = [x_i^r \quad y_i^r]^{\mathrm{T}} \tag{4.18}$$

Through i, p_i^r is compared with the laser fringe taken by the right camera. If p_i^r is within a certain range of the laser fringe taken by the right camera, the light plane can be determined, so as to reconstruct all the laser fringe.

4.3 multi-line scanning model

4.3.1 match marks

The matte ring mark point used can increase brightness along the direction of the light source (see figure 4.5). Under the condition of lighting, we extract the central circle and obtain the center point of the circle, which takes on the shape of an ellipse in the camera due to the camera's angle of view and distance.

Ring mark can be filtered out by size and shape.

(1) Size filtering. In binocular stereo vision, we can determine the size of the measured object projected in the image according to the size of the measured object, adjust the angle between the left and right cameras, and the distance between the object. When the camera angle is 0, the non-coding point produces the largest image on the CCD. Therefore, we only need to calculate the circumference of the non-coding point circle in the image taken at this time to determine the filter range. Through the above analysis, the camera working

distance in this paper is 300mm, the focal length of the camera is 8mm, the diameter of the non-coding point circle is 3mm, and the corresponding image circumference is about 200 pixels, so we can set a perimeter range to filter out ellipses that do not meet the conditions. We can filter out with the following constraints:

$$P_{min} < P < P_{max} \tag{4.19}$$

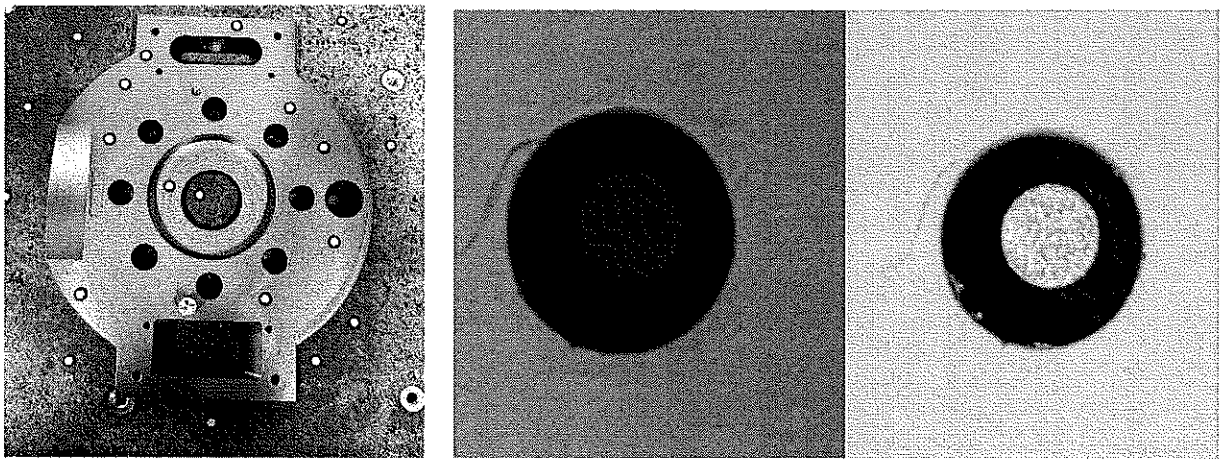

(a)Label mark points on the object

(b) No light on the left and light on the

Fig.4.5 Marker points

P is the contour circumference of the non-coding point circle projected on the image when the angle between the camera and the non-coding point is 0, P_{min} and P_{max} are the maximum and minimum values of the contour circumference projected on the image when the angle between the camera and the non-coding point is slightly changed, and the value here is P_{min} =200, P_{max} = 350 .

(2) There are many ways to describe the shape of non-coded points. In this paper, we select roundness as the shape criterion for describing non-coded points. Roundness can be used to describe how close the contour of a small circle is to a circle at a detected non-coding point, and we can define it as the ratio of the square of the circumference P of the small circle contour to the area A of the small circle:

$$C = \frac{P^2}{4\pi A} \tag{4.20}$$

When the outline is a standard circle, the roundness C takes a value of 1, which is the value of the non-coded point when the projection angle is 0 degrees. In actual measurement, the projection angle captured by the camera will change, that is, when the projection angle becomes larger, the roundness C will also become larger, and the ratio of the long and short axes of the ellipse will also become larger, and the error will be larger if the center of the ellipse is used as the anchor point. Therefore, we need to filter out this part of the ellipse. By calculation, we conclude that when the projection angle is 50 degrees, the roundness of the image outline of the non-coded point in this chapter has a range of values as:

$$1.0 < C < 1.7 \tag{4.21}$$

In order to get the correct matching point pair on the image captured by the left and right

cameras, we need to use the matching information and some topological relationships of other non-coding points within a certain range around the matching point to determine the uniqueness of the match. At present, there are two common matching methods: the first one is a 2D image matching method based on its own features , usually using SIFT operators or other methods to finish the matching of image feature points taken by left and right cameras in binocular stereo vision. This method doesn't need to manually paste marker points, but it is greatly affected by the surface of the measured object, for example, if the surface of the measured object is smooth and with no obvious features, the image matching can not be carried out smoothly. Moreover, in the high-speed real-time measurement, this method requires large computing, so it is not applicable. The second method is to combine coded and non-coded points [50]. Since the coding point has unique identity, we can find the corresponding point in the left and right images by decoding, and then match by establishing a topological relationship between the non-coding point and the coding point with a known matching relationship [51]. The topological relationship here makes use of the intersection ratio invariance principle of affine transformations. Next, we will give a brief introduction to this principle, as shown in figure 4.6.

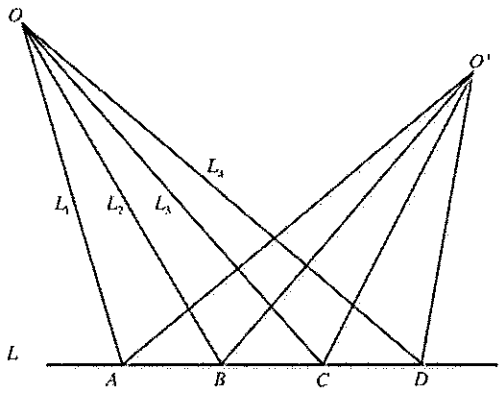

Fig.4.6 Schematic diagram of intersection ratio

In the figure 4.6, points A and B are called the base point pairs, and points C and D are called separated point pairs. The ratio of two directed line segments determined by the dividing point to the base point is called a simple ratio as follows:

$$SR(A,B,C) = AC/BC \tag{4.22}$$

$$SR(A,B,D) = AD/BD \tag{4.23}$$

while the ratio of two simple ratios in four points on a line is called the intersection ratio. The intersection ratio of the four points A, B, C, and D on the straight line in the figure is:

$$CR(A,B,C,D) = \frac{SR(A,B,C)}{SR(A,B,D)} = \frac{AC/BC}{AD/BD} \tag{4.24}$$

The straight line in space is transformed by spatial geometry and the intersection ratio of the

corresponding point column on the line remains unchanged, as shown in figure 4.7.

$$CR(A,B,C,D) = CR(A',\ B',\ C',\ D') \tag{4.25}$$

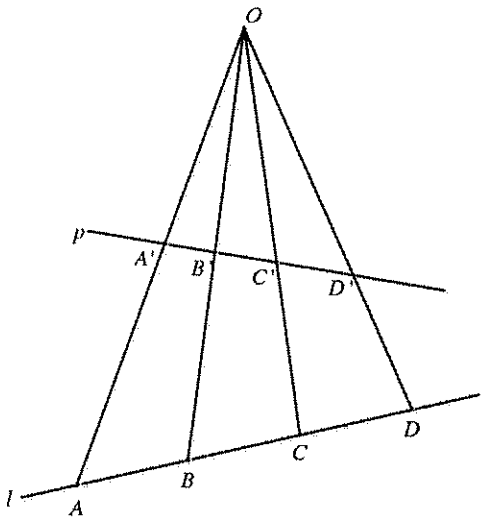

Fig 4.7 Schematic diagram of the spatial intersection ratio invariance

However, it is very strict in pasting coded points and non-coding points, otherwise it is easy to mismatch, so usually it is not suitable for practical applications, and the decoding process is also complex, not suitable for high-speed scanning. Using the binocular matching method of non-coding points, we only need to paste non-coding points instead of coding points as we want. And it is easy-to-operate and convenient, only to ensure that there are a certain number of non-coding points in the public field of view of the left and right cameras. This matching method combines the advantages of the RANSAC algorithm [52-53] and polar constraints, greatly reducing the false matching rate, so as to obtain as many matching pairs as possible. Next, we will briefly introduce the principle of the RANSAC algorithm.

Here we can use an example to describe the RANSAC algorithm, assuming that given some points on a 2D plane, now we need to fit these points to an approximate straight line, and the estimated mathematical model equation is the straight line equation. Because two points can determine a straight line, we first randomly select two of them, find their straight line equations, and then calculate the distance from other points on the plane to the line. Here we need to set the distance threshold to select the appropriate point, and then take out these points that meet the distance threshold range, and the target point can also become the inside point. After solving through multiple sampling, the straight-line equation obtained by the set of experiments with the largest number of internal points is the straight-line equation we need to fit. We think that this line is the best fit to these 2D plane points. The above is a preliminary explanation of the RANSAC algorithm, and it has obvious effect in image matching. For binocular stereo vision, assuming that the left and right cameras collect two pictures, there are N pairs of matching point among them, the set of matching point pairs is P, obviously there will be more or less some wrong mismatching, but the RANSAC algorithm can filter out them. Although it is a left and

right picture taken of the same object, due to the different perspectives that cause affine transformation, the geometric relationship between the two images can be described using the affine transformation matrix H with 9 parameters, that is, the transformation matrix will also be met between pairs of matching points. To solve the affine transformation matrix, we need at least 4 pairs of matching points.

The specific process of the RANSAC algorithm in image matching is as follows:

(1) Each time, N pairs of matching point can be randomly selected from the initially obtained set of matching point pairs P, where N is greater than or equal to 4;

(2) The affine transformation matrix H between the two images is calculated using the selected N pairs of matching points;

(3) Calculate the distance from other matching point pairs in the set P to the matrix H, and then find out the matching point pairs with distances less than the preset threshold T, and add these found matching point pairs to the inner point set. We record the number of matching point pairs c in the inner point set;

(4) Repeat the above three steps at k times;

(5) Compare the number of inner points c in the k sampling results, select the largest set of inner point data, and use it as the best set of matching point pairs;

(6) According to the maximum number of inner points calculated above, the affine transformation matrix H is recalculated;

However, the RANSAC algorithm takes a long time when there are many points.

As shown in figure 4.4, I_l and I_r are the image planes captured by the left and right cameras in the binocular measurement system, assuming that there is any point P, P_l and P_r are the projection points of point P on the left and right camera images, it can be seen that P_l and P_r are a pair of matching points, and there is the following conversion relationship between them:

$$P_r^T F P_l = 0 \cdot \tag{4.26}$$

F is the base matrix.

Since in real measurement, it is inevitably to have some errors caused by external conditions, so we only need to ensure that the distance between the center of the non-coded point and the pole line is within a certain threshold range can be counted as a candidate matching point, assuming this threshold range, the relationship is as follows:

$$P_r^T F P_l < \delta \tag{4.27}$$

The setting of the threshold depends on the accuracy of the camera calibration. In this chapter, we first used 0.01 pixel value as the threshold condition. Thus, we can get a candidate match point set N. However, due to the distribution of non-coding points and the extraction error of non-coding points, there will be some mismatches in the matching point pairs obtained by using polar line constraints. Sometimes one-to-one unique matches can also be false matches.

Therefore, how to eliminate false matching point pairs is the key to non-coding point matching. Usually there is a one-to-many situation during the experiment, when the polar constraint can no longer meet the uniqueness requirement. Since there are not many non-coded points that can be matched in the two figures, they cannot be filtered, but points with non-matching relationships need to be excluded. In this regard, we first need to find at least four pairs of unique matching points, through which the perspective transformation matrix H (containing 9 unknown parameters) can be solved, assuming that the perspective transformation matrix H has the following form:

$$H = \begin{bmatrix} h_{11} & h_{12} & h_{13} \\ h_{21} & h_{22} & h_{23} \\ h_{31} & h_{32} & h_{33} \end{bmatrix} \tag{4.28}$$

Assuming that the set of matching points between the two images captured by the left and right cameras is (x_i, y_i) and (x_i', y_i'), respectively, each set of matching points can obtain the following relationship according to the above perspective transformation matrix:

$$x_i'(h_{13}x_i + h_{32}y_i + h_{33}) = h_{11}x_i + h_{12}y_i + h_{13} \tag{4.29}$$

$$y_i'(h_{31}x_i + h_{32}y_i + h_{33}) = h_{21}x_i + h_{22}y_i + h_{23} \tag{4.30}$$

Through four pairs of non-collinear matching point pairs, we can find all the parameters of the H matrix, and then calculate the distance from the matching point pairs in the remaining matching point sets to the matrix H. Set a threshold T, all points with a distance less than the threshold T will be added to the set of matching points, and then we record the number of matching points c in the set. Repeat multiple sampling, we solve the number of matching point pairs c according to the perspective transformation matrix H obtained each time, and then compare the number of these matching point pairs, and take the largest value as the best value, so that we can get the correct matching point pair, so as to add constraints to one-to-many matching point pairs, find unique matching point pairs, and filter out one-to-one mismatched point pairs.

Take an image with a mark with a binocular (see figure 4.8).

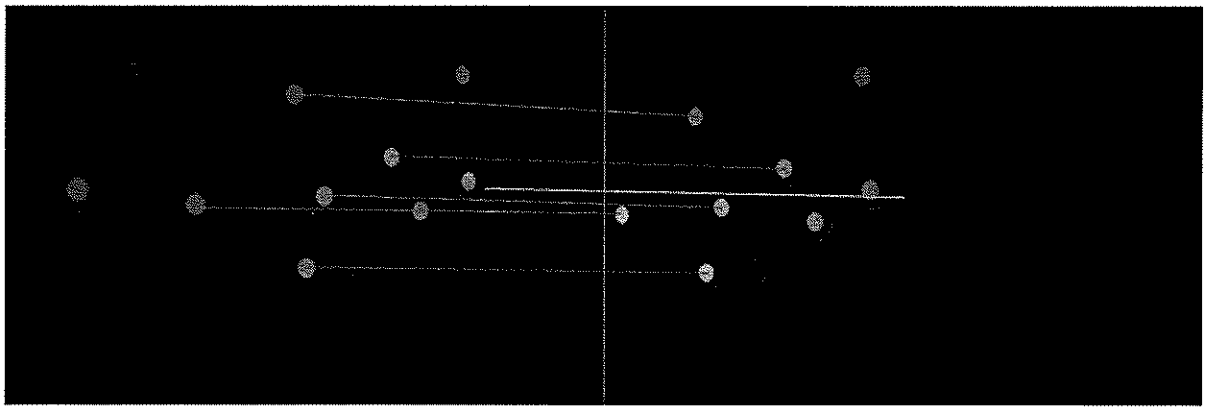

Fig.4.8 marks match.

The purpose of 3D matching is to convert the local point cloud data reconstructed from

different perspectives to the same coordinate system, which is also to realize the reconstruction of the entire measured object through multiple perspectives under the condition of insufficient single-view 3D information. Now there are also some solutions, one of which is to use multiple cameras to shoot the measured object from different perspectives. Because the camera is fixed, so the relative position relationship between them can be guaranteed. This way, the coordinate system under each camera can be converted to a coordinate system through the position relationship, so as to reconstruct the entire shooting object. The advantage of this method is that it is more convenient and faster. However, the fixed camera is not convenient to carry, and the cost is high, so it is not practical.

The advantage of handheld laser 3D scanning is its portability and not affected by geographical factors. From the perspective of real-time measurement, if the camera can collect 50 pictures per second, then laser scanning measurement needs to complete 50 image processing, matching, reconstruction and 3D matching in one second, and the scanning of the entire measured object requires at least thousands of times. Therefore, there is high standard for scanning speed. Moreover, the speed of the 3D matching algorithm directly affects the speed and accuracy of the entire scanning process. At present, researchers in China and abroad have also done several deep research and experiments on 3D data matching, and one of the most common methods is a 3D matching based on distance matrix [54]. This method requires us to manually paste marker points on the object, and then use the spatial invariance of marker points [55] to establish a spatial distance matrix between marker points, and then find matching marker points through iteration. This method can realize the automatic matching of spatial marker points, but it does not effectively use the information around the matching marker points, so the accuracy is not high, and mismatching occurs when the distance is equal. The above matching method is not high in accuracy and slow, which is difficult to meet the requirements of multi-view matching during real-time 3D scanning. This paper proposes a 3D matching method based on Euclidean distance for non-coded point 3D matching, which makes full use of the Euclidean distance information of the points around each 3D point, and these information are different, so that each 3D point can be labeled with an identity, just like an ID card, so that we can precisely find the matching point pair.

In the last section, we introduce detailed binocular matching of non-coded points, so we can add two points clouds obtained from different angles that have been reconstructed by the binocular system, and the two points clouds exist in a common area for 3D reconstruction. Suppose these two points clouds are point cloud A and point cloud B, the set of non-coding points in point cloud A is represented by $M(p_i)$, and the set of non-coding points in point cloud B is represented by $M(q_i)$. The essence of 3D matching is the 3D matching of spatial point clouds, as long as the common non-coding point part of the two points clouds is found, the rotation translation of the two points clouds can be solved, and finally normalized to the same coordinate system. This method comprehensively uses the "spatial feature invariability"

constraint, "continuity" constraint and "uniqueness" constraint to match the point cloud. Among them, the "spatial feature invariability" constraint means that if there are common points in two points clouds, then the Euclidean distance between these common points must be equal. The "uniqueness" constraint, as the name implies, is that the pairings between matching points must be unique. The "continuity" constraint means that the correctly matched points are always continuous across two points clouds.

Since the position of each reconstructed non-coding point in the point cloud is fixed, its Euclidean distance relationship with the surrounding point cloud is also fixed. We can use these relationships to label each non-coded point with its own Euclidean distance feature label. We can consider each label as an ordered container, and the order represents the only feature of the non-coding point, which we call the Euclidean distance feature of the non-coding point.

Suppose p_i is a point in the set $M(p_i)$ and q_i is a point in the set $M(q_i)$, in order to find the matching point in the set Q, we need to go through the following steps:

(1) First, we find the label of p_i, that is, solve the Euclidean distance from the point to p_i in $M(p_i)$;

(2) Then we arrange them in order of distance and size, and store them in the corresponding array container Vp_i.

(3) Then we solve the labels of the points in $M(q_i)$ and save them to their array containers Vq_i respectively;

(4) We compare the distance in all array containers Vq_i with the distance in the array container Vp_i in turn, due to the existence of error, even if the two points clouds have something in common, the Euclidean distance between them will not be exactly the same, so it is necessary to set a threshold T to count the paired distance that meets the threshold range, and finally obtain the counting result C_j;

(5) Repeat step (4) to obtain the counting result C_j of the point p_i in $M(q_i)$, compare the result C_j. The maximum value corresponding to q_j is the spatial match point of p_i, but sometimes because the maximum value has duplicate, then we can discard and continue to start from step (1), if there is only one maximum value, then we execute the next step;

(6) We can start from the matching point pair when we find it, if the distance between a point p_i and p_i in $M(p_i)$ is $d(p - p_i)$, and then go to $M(q_i)$ to find a point q, that is:

i. $|d(q - q_i) - d(p - p_i)| < T$

(7) Then the point p is the spatial match point of the point q.

(8) Repeat step (6) until all matching point pairs have been identified. By taking steps [56] above, point clouds can be matched. But it's still not very convenient. But if the linear laser camera and the measuring arm are well coordinated, the matching of marker points can be very easy.

From the step above, we find it isn't convenient to use mark points to stitch the point clouds. Use posture during articulated arm working to replace the mark point. Hand-eye calibration is

necessary for multi-lines structured light camera to work with articulated arm.

4.3.2 Hand-eye calibration

We can use the approach of 2.3.3.2 section to calibrate the relationship between camera and the end-of articulated arm CMM.

4.4 Conclusion

This chapter studied the 3D reconstruction of multi-lines lasers. Firstly, we introduce the binocular reconstruction algorithm. Secondly, we have studied multi-lines 3D reconstruction. Last, we have studied the marker points matching method before point clouds stitching, as the complex of the marker points, we proposed that use articulated arm's posture to replace the method of marker points.

Chapter 5 Experiment

5.1 single-line scanning system experiment

5.1.1 The hardware system

Fig.5.1 is the hardware system used in this experiment. The system mainly consists of a calibration board that is a white standard plane plate, a flexible 7-axis measuring arm, line laser and 2D camera. The hardware parameters are as follows:

1) Flatness of the calibration board:0.015mm.
2) The precision of the articulated arm: 0.02mm.
3) linear structured light 3D camera based on camera and laser
   a) Z direction resolution: 0.01-0.012mm.
   b) X direction resolution: 0.025-0.028mm.
   c) The field of view of the line sweep camera: 62-72mm.
   d) laser wave length: 405nm

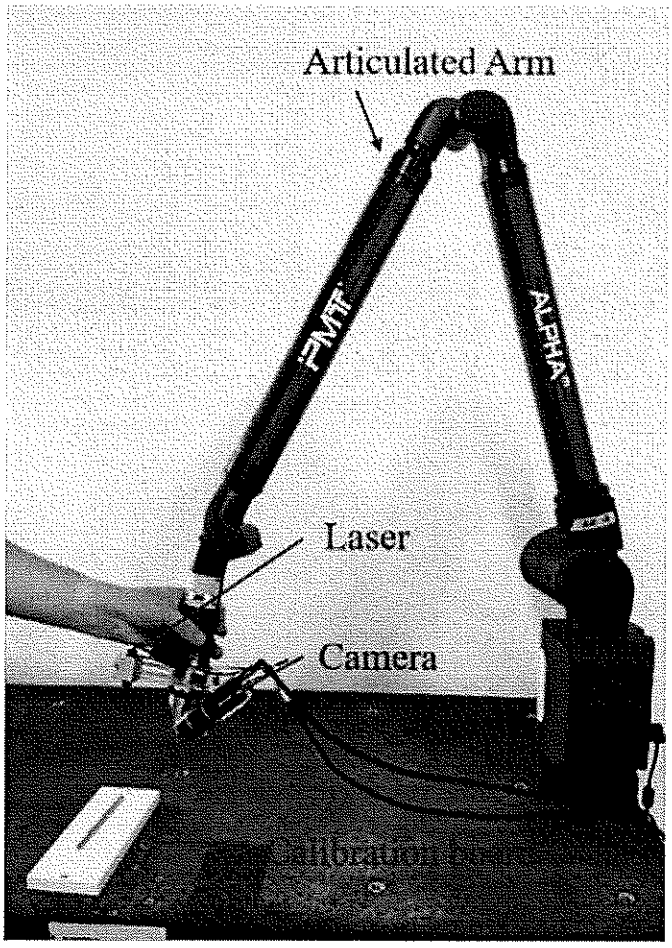

Fig.5.1 hardware system

5.1.2 The experimental steps

The experimental process as follows:

1） Calibrate 2D camera and laser plane equation

Position the calibration board under the camera shown in figure 5.2 at different angles and take at least 8. The circle centers of each captured image were extracted ,then the internal parameters of the camera and the distortion of the lens are calibrated by Zhang Zhengyou's calibration method. As shown in figure 5.3, we captured the center of the circle on the calibration board, assign the value of the world coordinate system to each center according to the specifications of the calibration board, and calibrate the internal parameters .The internal parameters of the calibrated camera are:

$$M = \begin{bmatrix} 5145.36 & 0 & 1517.37 \\ 0 & 5153.66 & 1023.36 \\ 0 & 0 & 1 \end{bmatrix}$$

The corresponding distortion parameter K is:

$$k = [-0.09035\ 0.1954\ -0.000659\ -0.000978\ -0.4617]$$

Capture the laser line on the calibration board image. Then keep the calibration board stall, turn off the laser, adjust the exposure time of the camera, and take the corresponding calibration board image. Within the laser irradiation and the camera's field of view, move to the b,c positions, as shown in figure 5.4.

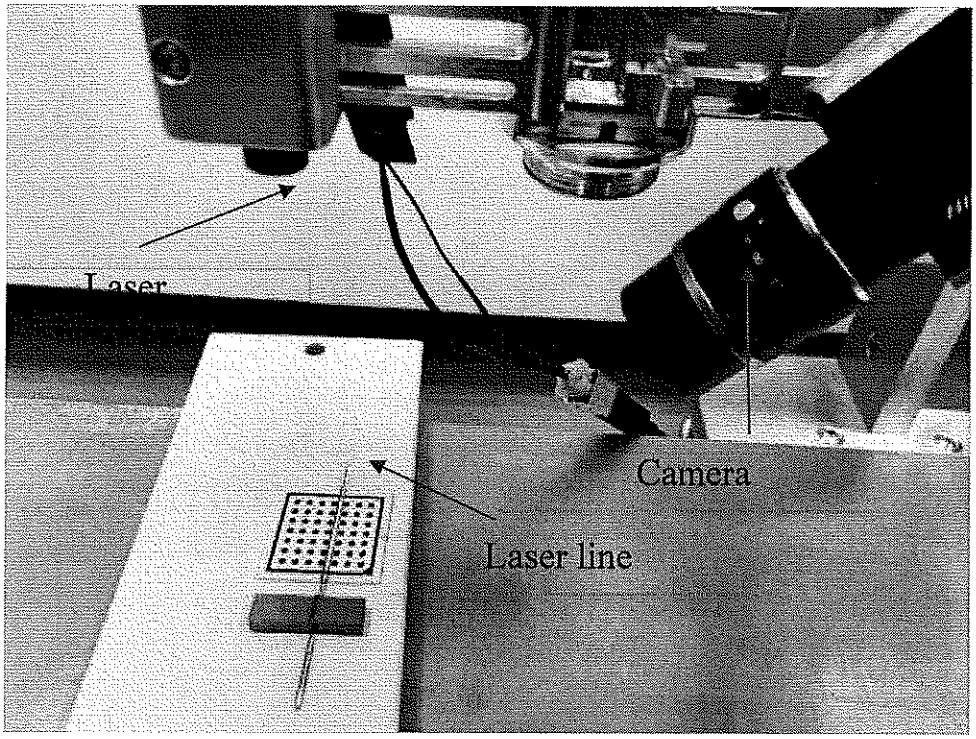

Fig.5.2 The equipment for experiment

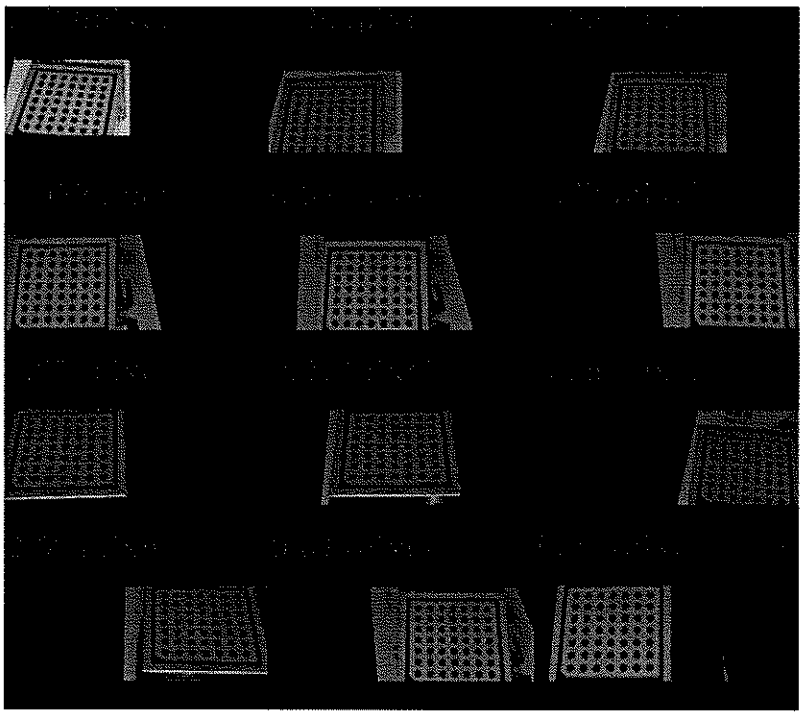

Fig.5.3 figures collected for calibration camera, green note stands for RMS(Root Mean Square)

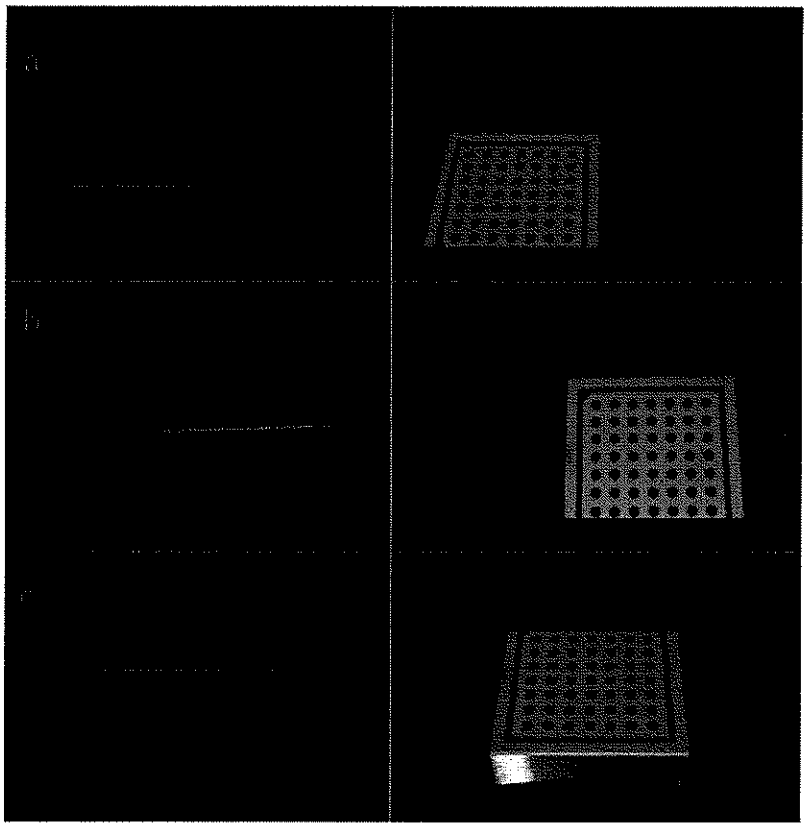

Fig.5.4 Calibration laser plane, left side is the image of laser line on the calibration board, right side is the image of calibration board when laser turn off.

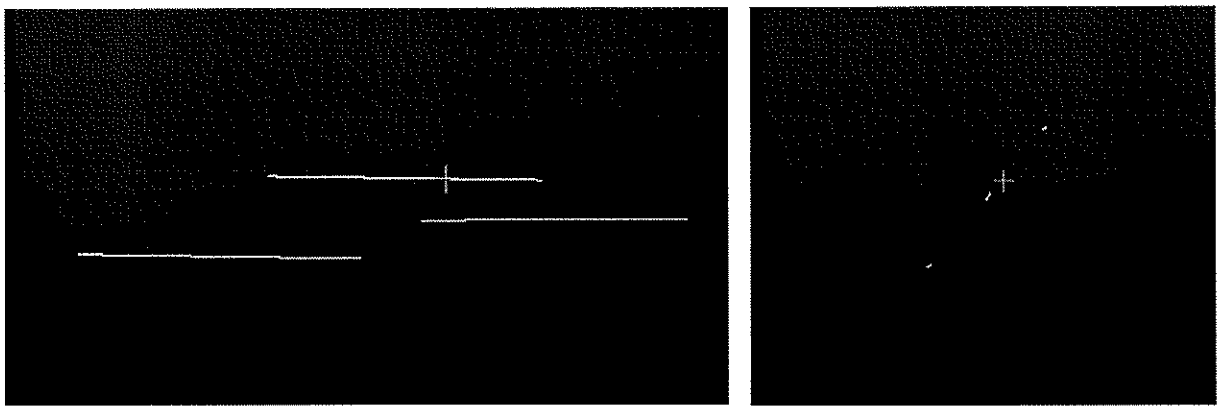

a. Z direction view b. Y direction view

Fig.5.5 points cloud extracted for calibration the laser line,
two different views in camera coordinate system

The pixel center of each position photographed into the light stripe was extracted, and the 3D coordinates of the light stripe under the camera coordinate system were calculated through the camera's internal parameters and the center information of the calibration board.

Fit the 3D coordinates of each collected light stripe to a plane. After normalizing the normal vector of the plane, we can get:

$$-0.0042275x + 0.73558y - 0.67742z + 91.78 = 0$$

Import the extracted light stripe point cloud into the 3D software, as shown in figure 5.5.

2) Calibrating board setting and planar equations obtaining

The calibration board is fixed on the desktop, and the hard probe of the measuring arm is used to measure around the plane calibration board. The positions measured around the measuring arm are shown as the black dots in Fig5.2. The plane equation of the calibration plate in the articulated arm base coordinate system $O_bX_bY_bZ_b$ can be obtained with the following parameters:

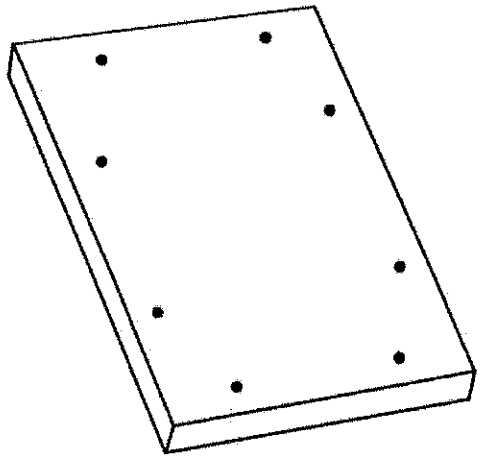

Fig.5.6 Reference position diagram of calibration board

$$[A_b\ B_b\ C_b\ D_b] =$$
$$[0.0001814\ \ 0.00000737\ \ 0.9999\ 6.3935]$$

3） Image information obtaining

The articulated arm takes linear structured light 3D camera to scan the calibrated board from different attitudes as Fig.5.7 shown. In the attitude a, c, e, the laser light plane is perpendicular to the calibration plate as far as possible. In the attitude b and d, the included angle between the laser light plane and the calibration plate plane is about 45 degrees. At least 2 times of data collection under each attitude Fig.5.8 shown. The aim is to cover as much as possible the working attitude of the linear structured light 3D camera.

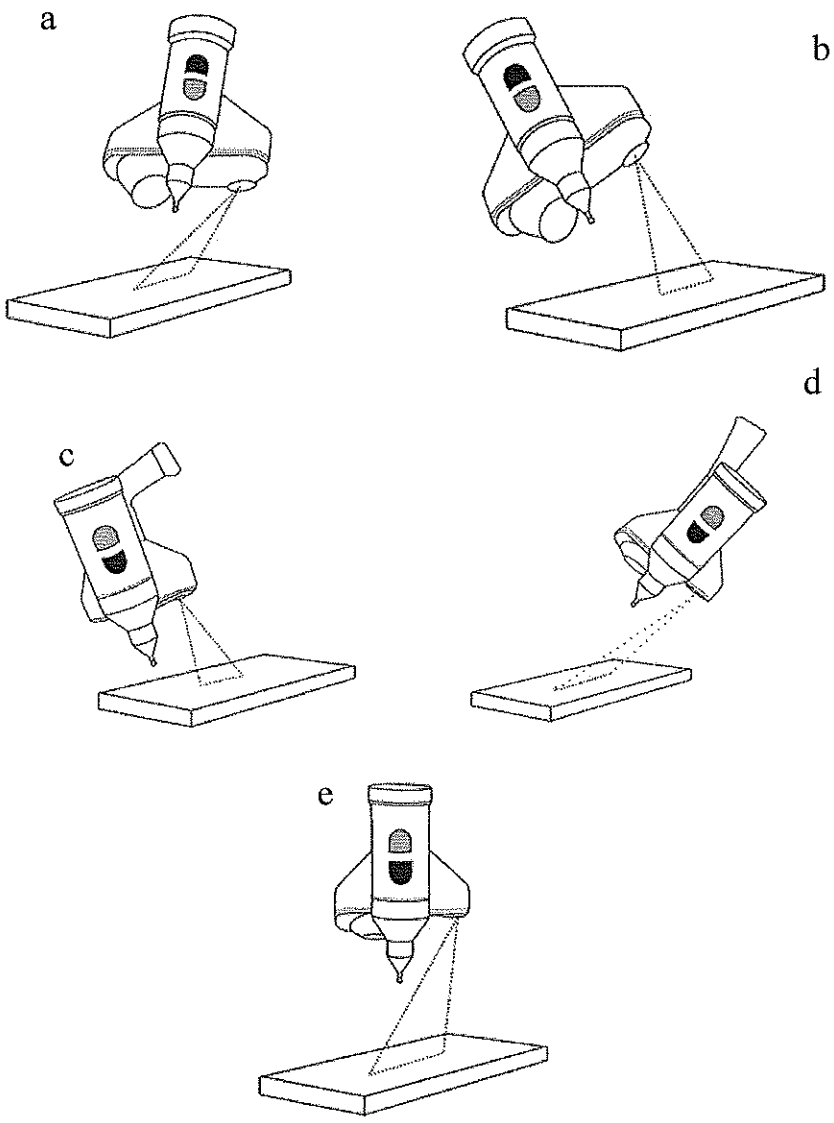

Fig.5.7 Reference position diagram of scanning

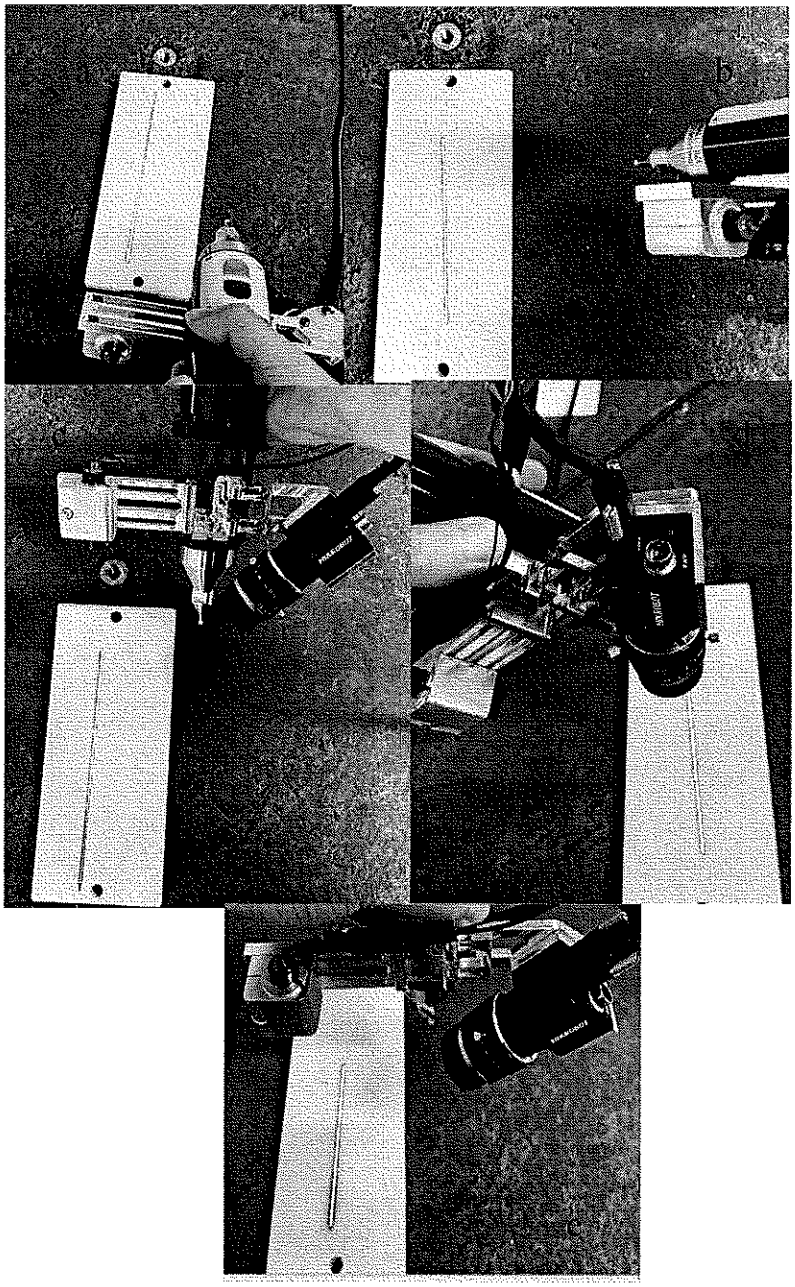

Fig.5.8 Scanning calibrated board with 5 angles

Fig.5.9 shows captured images by camera on each posture. Table 3 shows the attitude and position of the end-effector feedback of the articulated arm when linear structured light 3D camera scanning calibration board. A, B and C represent the pitch angle, yaw angle and roll angle of the end-effector respectively, and the unit is Angle. X, Y, and Z are the position components of the end-effector in the $O_bX_bY_bZ_b$ coordinate system X, Y, and Z in millimeters.From A, B, C, X, Y, Z we can get ${}^{b}_{t}R$ and ${}^{b}_{t}T$, get ${}^{t}_{b}R$ and ${}^{t}_{b}T$.

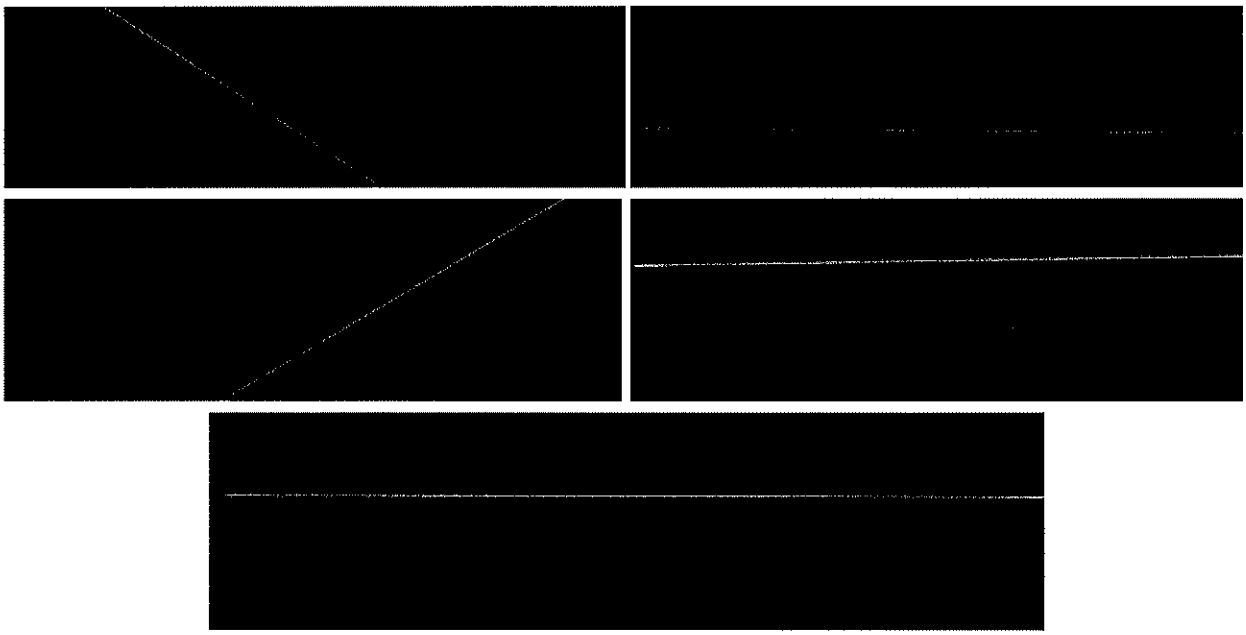

Fig.5.9 Captured images by camera on each posture

Table 3 Arm coordinates collected for each of the five postures.

Posture	A	B	C	X	Y	Z
a	178.812	4.462	19.542	649.179	-171.705	201.483
b	183.281	-23.115	31.753	744.115	-197.079	179.886
c	146.105	3.211	23.922	649.743	-63.662	143.021
d	-176.732	41.058	19.680	499.043	-188.059	200.824
e	-145.388	-1.381	31.560	651.862	-308.580	174.691

The plane parameters A_b, B_b, C_b, D_b can be converted into the corresponding $A_t^i, B_t^i, C_t^i, D_t^i$ (I equals a,b,c,d,e) with ${}_b^tR$ and ${}_b^tT$. Substitute the laser points P_s^{ij} obtained by scanning in Step 2) and $A_t^i, B_t^i, C_t^i, D_t^i$ into the target equation to obtain:

$$ {}_s^tX = \begin{bmatrix} -0.42453 \\ 0.663009 \\ -0.61659 \\ 41.376 \\ -0.90541 \\ -0.31178 \\ 0.288130 \\ 21.496 \\ -0.00121 \\ 0.680594 \\ 0.73266 \\ 112.286 \end{bmatrix} $$

Write the result above as ${}_s^tR$ as follows:

$$ {}^{t}_{s}R = \begin{bmatrix} -0.4245 & 0.6630 & -0.61659 \\ -0.90541 & -0.31178 & 0.28813 \\ -0.00121 & 0.68059 & 0.73266 \end{bmatrix} $$

The corresponding angles θ, γ, φ:

$\theta = -21.468°, \gamma = -38.068°, \varphi = -122.632°,$

Translation vector ${}^{t}_{s}T$:

$$ {}^{t}_{s}T = [41.376 \quad 21.496 \quad 112.286]^{T} $$

In this way, the parameters of hand-eye calibration are obtained. Repeat 5 times according to the above experimental steps to get table 4. The average values of ${}^{t}_{s}R$ and ${}^{t}_{s}T$ of the 5 experiments results are as follows.:

$$ {}^{t}_{s}R = \begin{bmatrix} -0.4245 & 0.6630 & -0.6166 \\ -0.9054 & -0.3119 & 0.2881 \\ -0.00121 & 0.6806 & 0.7327 \end{bmatrix} $$

$$ {}^{t}_{s}T = [41.341 \quad 21.504 \quad 112.257]^{T} $$

${}^{t}_{s}R$ and ${}^{t}_{s}T$ are used as hand-eye calibration results to verify the 3D image measurement accuracy of the system.

In Fig.5.10, we use the scanning system to scan the cup and get the point clouds with the hand-eye calibration results.

5.1.3 Verifying the calibration accuracy

Table.4 Hand-eye calibration results obtained by 5 times

No.	θ	γ	φ	t_x	t_y	t_z
1	-21.468	-38.068	-122.632	41.376	21.496	112.286
2	-21.405	-38.031	-122.617	41.338	21.521	112.232
3	-21.464	-38.083	-122.648	41.432	21.477	112.289
4	-21.522	-37.990	-122.635	41.224	21.550	112.154
5	-21.370	-38.131	-122.578	41.337	21.483	112.326
AVG	-21.446	-38.061	-122.622	41.341	21.505	112.257
Std	0.0530	0.0477	0.0241	0.0681	0.0269	0.0598

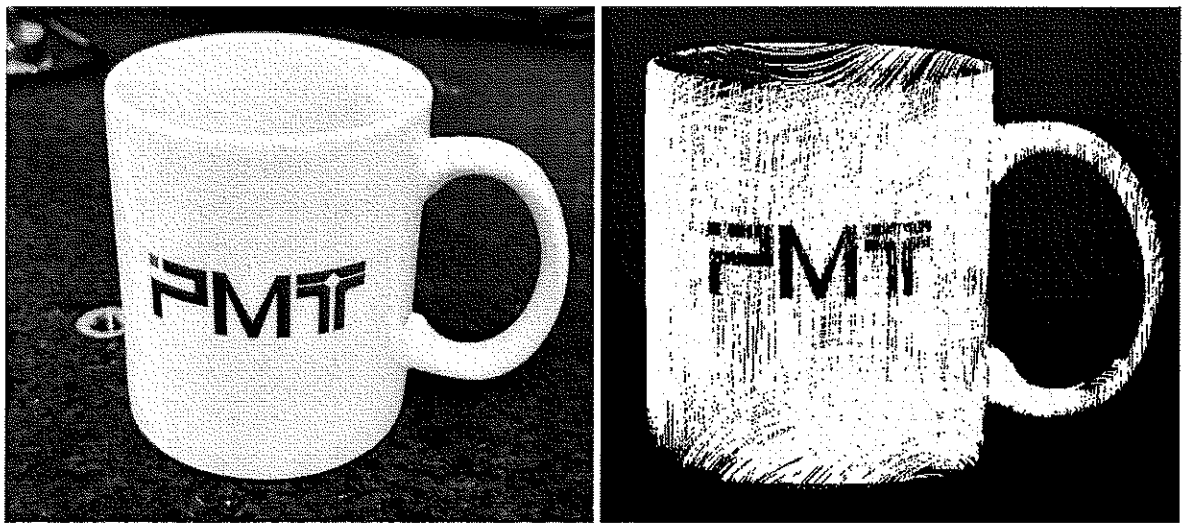

Fig.5.10 cup and points clouds obtained

In order to verify the accuracy of the calibration, measurement experiments of several objects were performed using the above calibration results. Fig.5.10 shows the white flat plate one the left, the true value of flatness of board is 0.015mm manufacturer afforded, and points cloud obtained by about 83210 pixels converted.

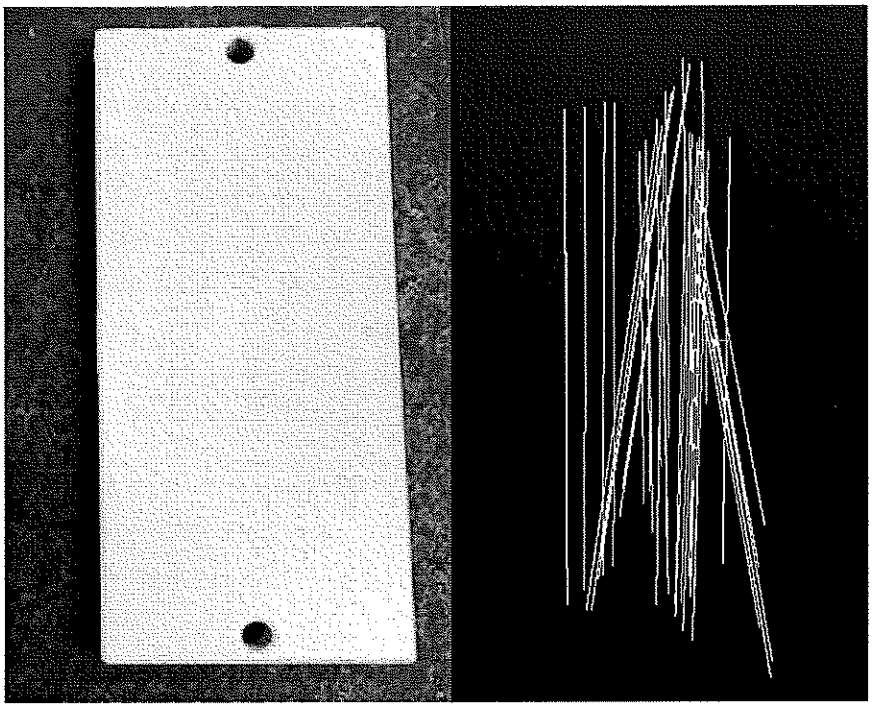

Fig.5.11 calibration board and points clouds obtained

The distances from all points to the plane were plotted as the histogram shown in Fig.5.12 where the horizontal axis stands for the distance bins and the vertical axis stands for the numbers of points. The horizontal axis unit is millimeter. From Fig.5.12, about 97.9% of points were distributed between -0.05mm and 0.05mm.

5.1.4 Measured results and precision analysis

A standard metal ball with tolerance of 0.02mm and a diameter of 34.96mm was measured. Fig.5.13 is standard metal standard ball on the left and the points cloud obtained by scanning the standard ball on the right. About 179427 pixels of 3D image are convert to points. The points are fitted into a ball by the least square method and the ball diameter was calculated to be 34.94mm. Calculate the distances from the measured points to the least-squares ball center subtracted by the radius of the standard ball, and plot them as a histogram shown in Fig.5.13 where the horizontal axis stands for the distance bins and the vertical axis stands for the numbers of points.

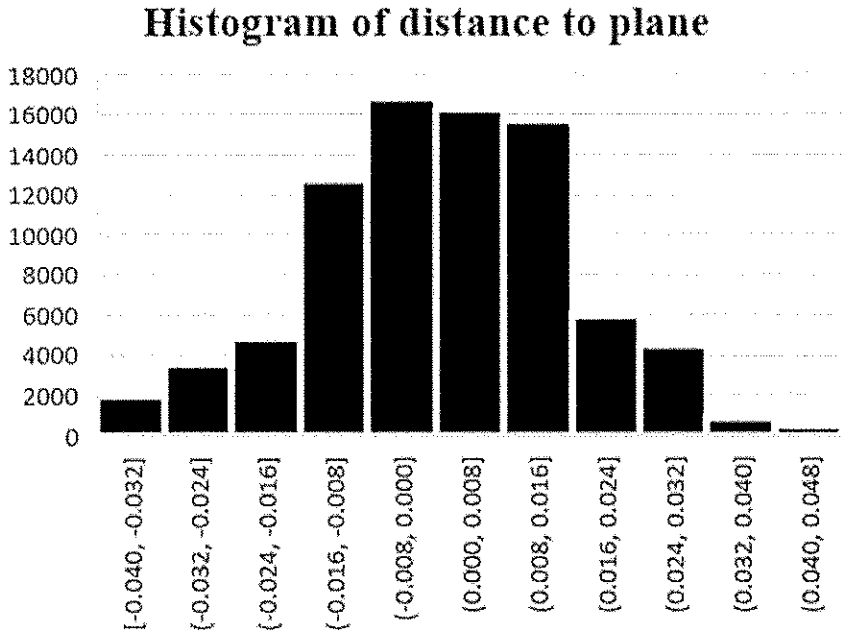

Fig.5.12 Histogram of distance to plane

As shown in Fig.5.14, 95.54% of the points in the histogram of the difference between the distance from the measured point to the center of the ball and the radius of the ball are distributed in -0.05mm to 0.05mm. The accuracy can reach 0.05mm obtained for the difference between the measured diameter of the ball and the standard diameter based on ISO-10360-8.

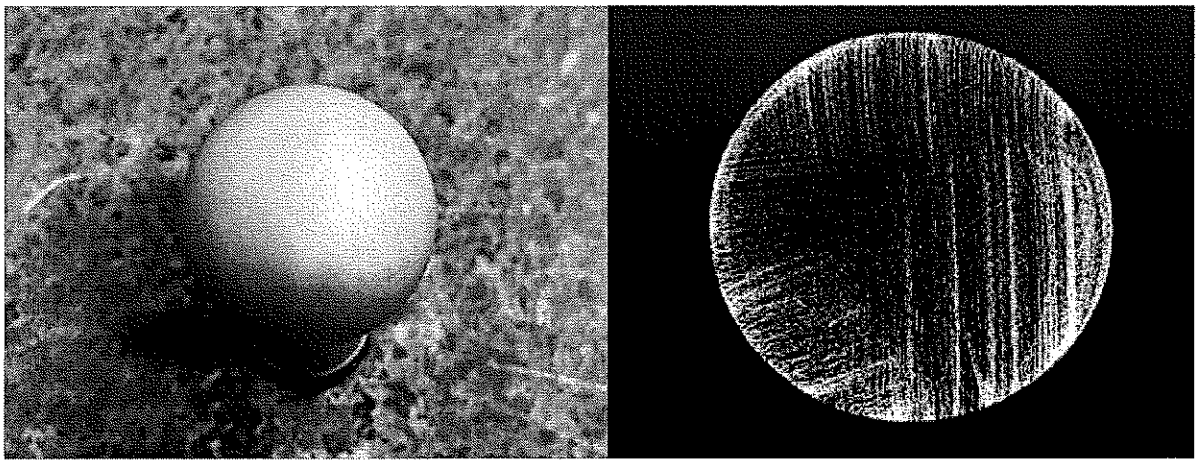

Fig.5.13 standard ball object and the points cloud obtained by scanning

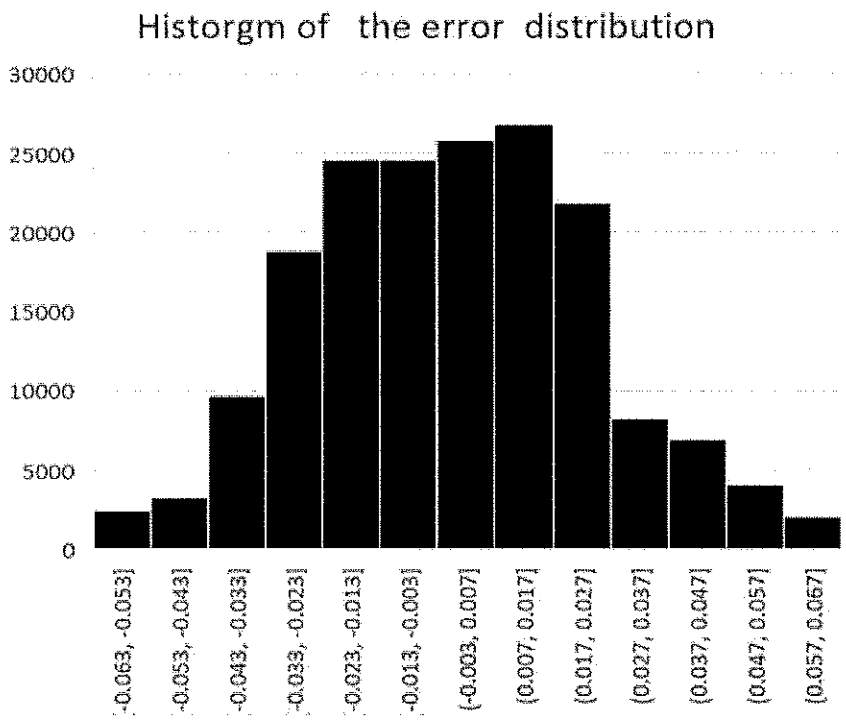

Fig.5.14 Histogram of the difference with the radius of the ball

The problem that traditional hand-eye calibration method is not suitable for the articulated arm scanning system is solved. Aiming at the difference between articulated arm and Robot, a plane calibration board with certain flatness is proposed as the calibration tool, and the target equations for solving ${}^{t}_{s}R$ and ${}^{t}_{s}T$ are constructed. Experiments verify the feasibility of the method, and the scanning standard ball accuracy can reach 0.05mm.

5.2 Cross-line scanning system experiment

5.2.1 The hardware system

Fig.5.15 shows the hardware system used in this experiment. The system mainly consisted of a flexible 7-axis measuring arm, laser A, laser B, and a 2D camera. The hardware parameters were as follows:

(1) The precision of the articulated arm: 0.02mm.

(2) For the 2D camera:

a) Z direction resolution: 0.01-0.012mm.

b) X direction resolution: 0.025-0.028mm.

c) The field of view of the line sweep camera: 62-72mm.

d) Laser wave length: 405nm

Fig.5.16 shows the calibration camera and the circular array calibration plate used for hand–eye calibration. In Fig.5.16, the circle spacing was 3.75 mm, the circle diameter was 1.875 mm, and the accuracy was 0.001 mm. The material was ceramic. The metal gauge block used to verify the calibration result is also shown.

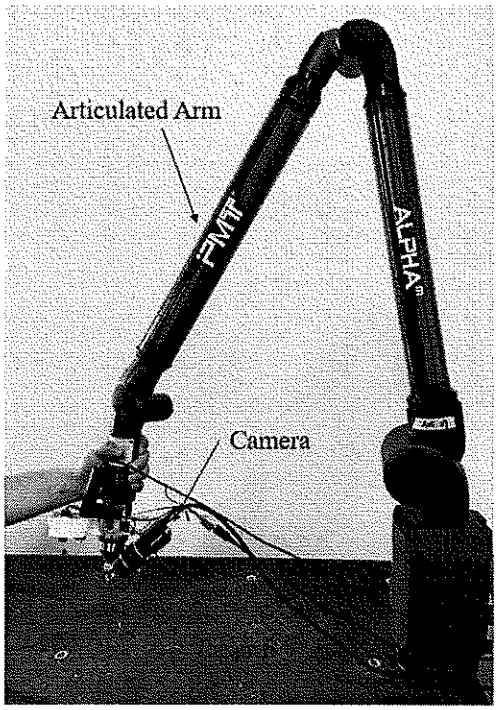

Fig.5.15 Hardware system

5.2.2 Calibration of the camera and laser light plane

First, the camera was calibrated, following which the calibrated camera parameters were used to calibrate the optical plane of AB and lasers A and B. As shown in Fig.5.17, 15 pictures were collected from various angles, and the internal parameters of the camera were obtained using the calibration method of Zhengyou Zhang, where $fx = 5145.362$, $fy = 5153.664$, $cx = 1517.375$, and $cy = 1023.363$. In the obtained distortion parameters, for the radial distortion, $k_1 = -0.09903$, $k_2 = 0.195427$, and $k_5 = 0.41673$; meanwhile, for the tangential distortion, $k_3 = -0.000065974$ and $k_4 = -0.0000978477$.

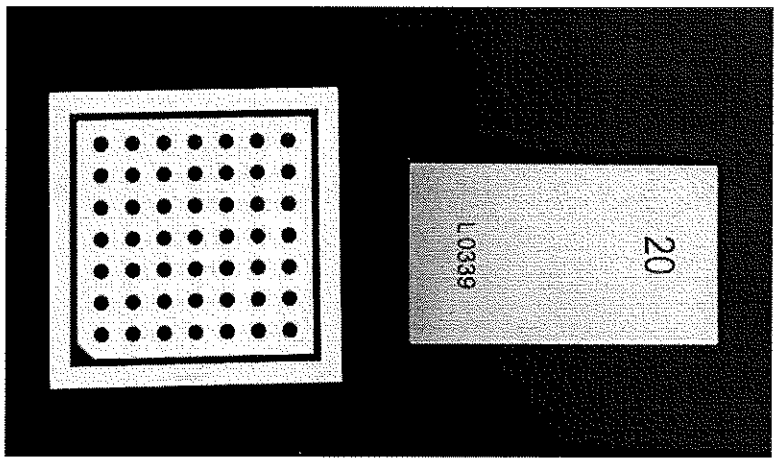

Fig.5.16 Calibration board and gauge blocks

As shown in Fig5.18, the upper and lower graphs on the left were used to calibrate the optical plane of laser B, while the upper and lower graphs on the right were used to calibrate the optical plane of laser A. The calibrated equation of the light plane of laser A was as follows:

$$[A_a\ B_a\ C_a\ D_a] = [-0.659905\ -0.551732\ 0.51\ -68.7215]$$

while that for laser B was:

$$[A_b\ B_b\ C_b\ D_b] = [0.76417\ -0.543156\ 0.34787\ -49.616]$$

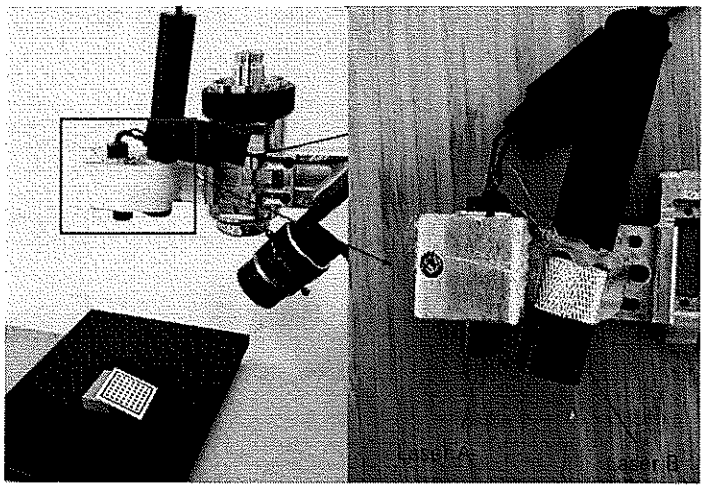

Fig.5.17 Calibrate the camera. Laser B is fixed by hot glue

The accuracy of the calibration was verified by measuring the height of 20 mm and the statistical height distribution, as explained next.

As shown in figure 5.19, a measurement block with a height of 20 mm was used for verification. The abscissa represents the measured height (in mm), and the ordinate represents

Fig.5.18 Calibration the laser line plane

the height value statistics (in units). The mean height was 19.989 mm, and the standard deviation(std) of height was 0.006 mm.

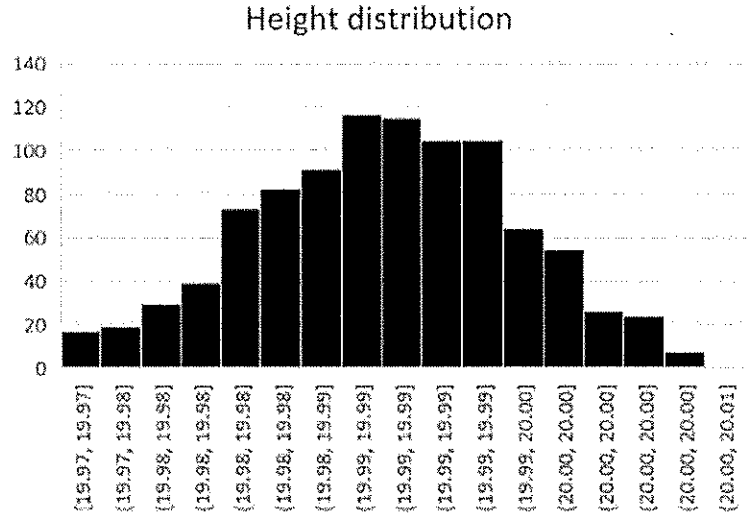

Fig.5.19 Histogram of the height of block

5.2.3 Hand–Eye Calibration

As shown in Fig5.20, the joint arm with the camera photographed the calibration plate in

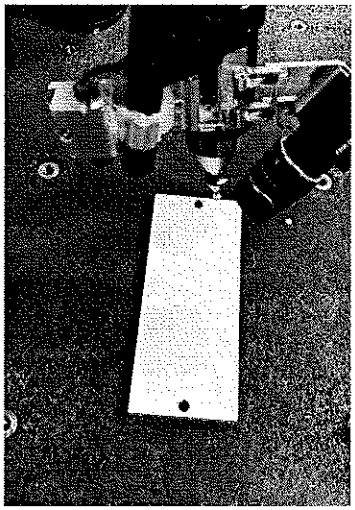

Fig.5.20 One of the six postures captured

different postures and recorded the coordinates of the joint arm feedback. A total of five sets were captured. we obtained the hand-eye relationship X:

$$X = \begin{bmatrix} -0.42684 & 0.66270 & -0.61532 & 4.1373 \\ -0.904314 & -0.3163 & 0.286604 & 21.393 \\ -0.004728 & 0.678785 & 0.73432 & 112.962 \\ 0 & 0 & 0 & 1 \end{bmatrix}$$

The calibration result X and laser light plane parameters were used for scanning and testing. Fig.5.21 shows a scan of the calibration plate (note that only a single scan could be completed),

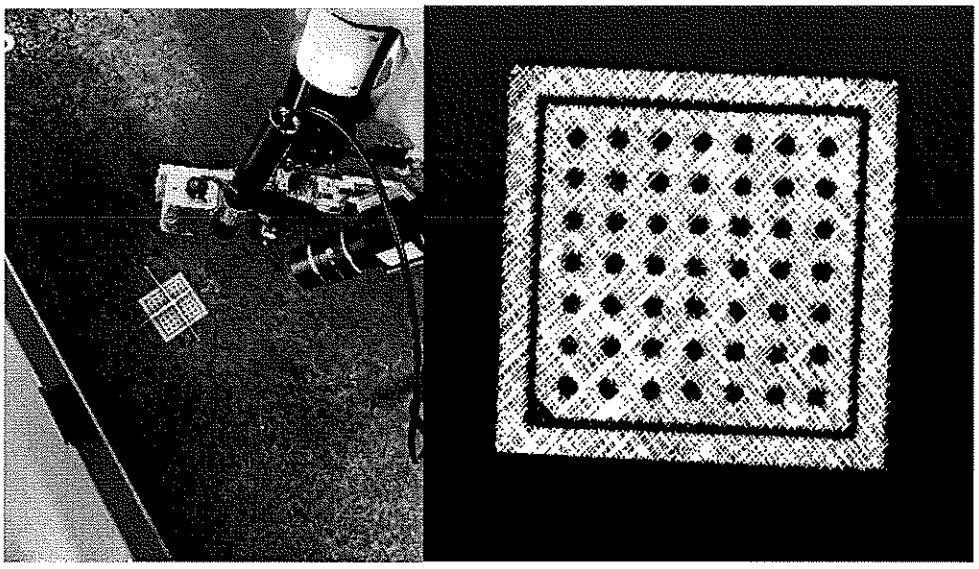

Fig.5.21 Calibration board scanning result

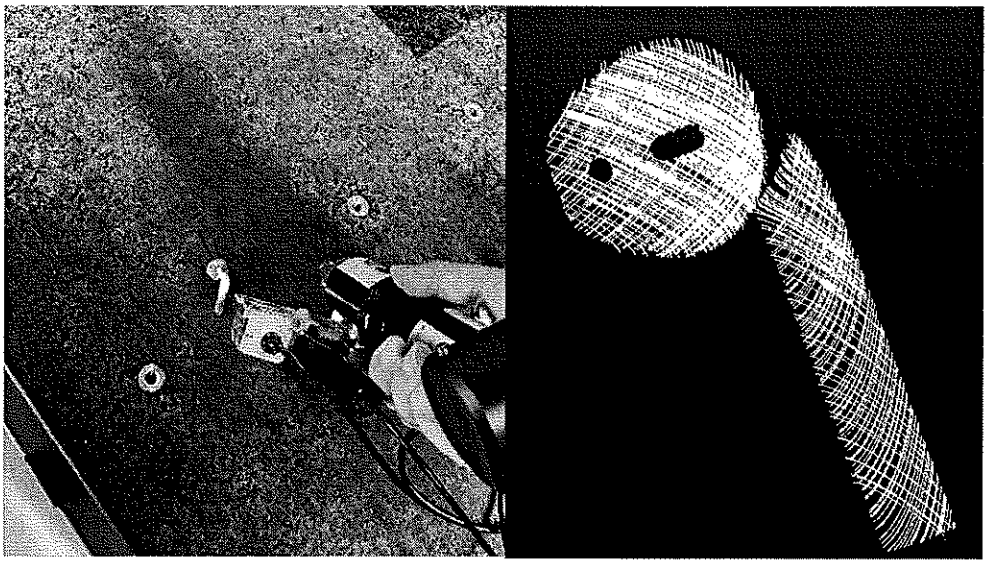

Fig.5.22 Air pod scanning result

Fig.5.22 shows a scan of a complex surface that is correct, and Fig.5.23 shows a standard ball.

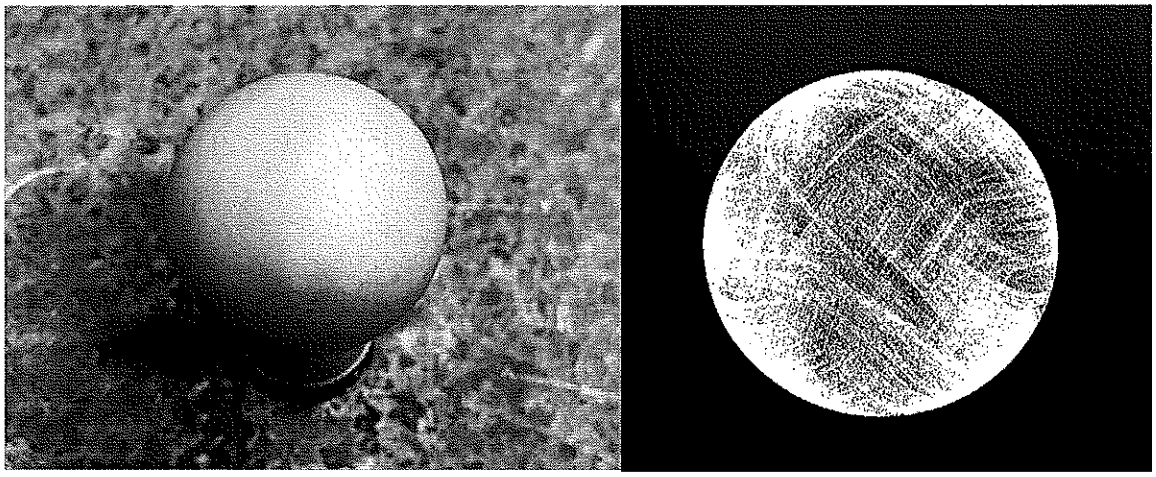

Fig.5.23 Standard ball scanning result

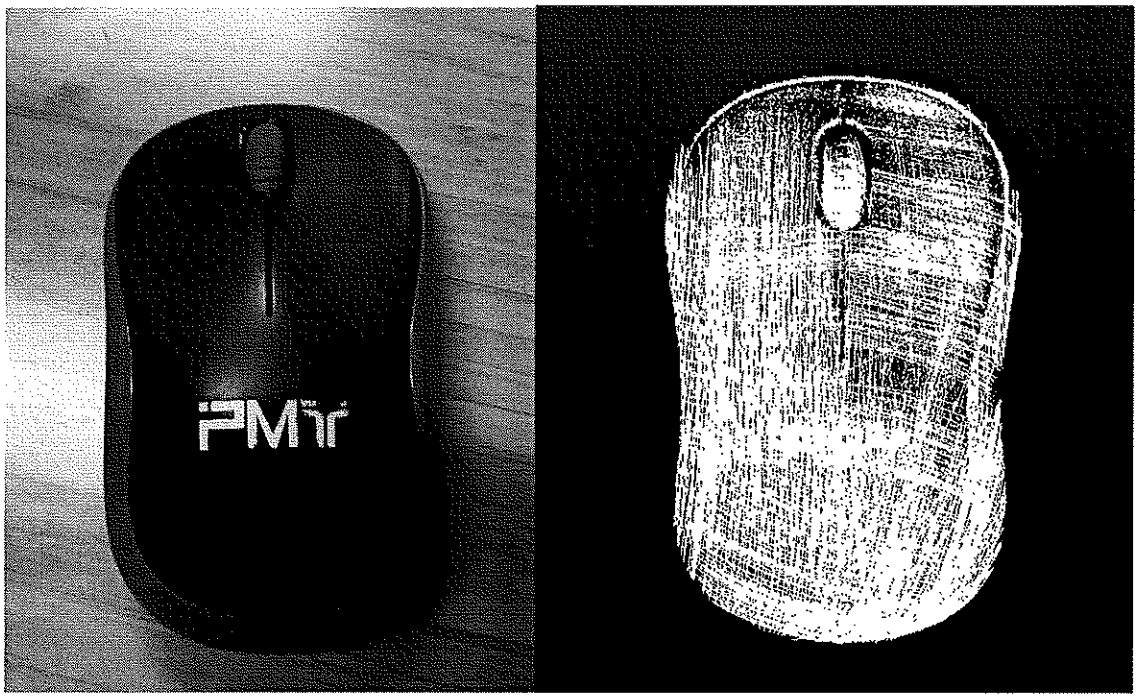

Fig.5.24 Mouse scanning result

In the scan, the determination threshold T of equation (3.6) was set as 10 pixels.

If equation (3.6) and equation (3.7) both met the conditions, the one with the smallest difference was chosen.

Point clouds are obtained shown in Fig.5.25 when the flat board is scanned in one direction with a single-line and a cross-structured light.

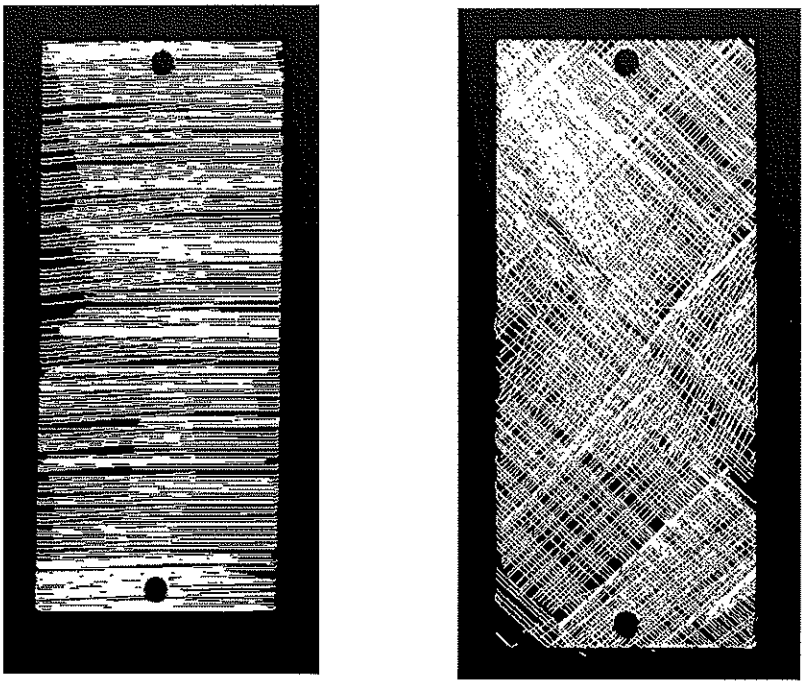

(a) Single-line structured light (b) Cross-line structured light

Fig.5.25 Flat board point clouds with single-line and multi-line structured light

We scan the workpiece shown in Fig.5.26 (a) and use the software PolyWorks [57] to calculate the deviation from the model in Fig.5.27 (b).

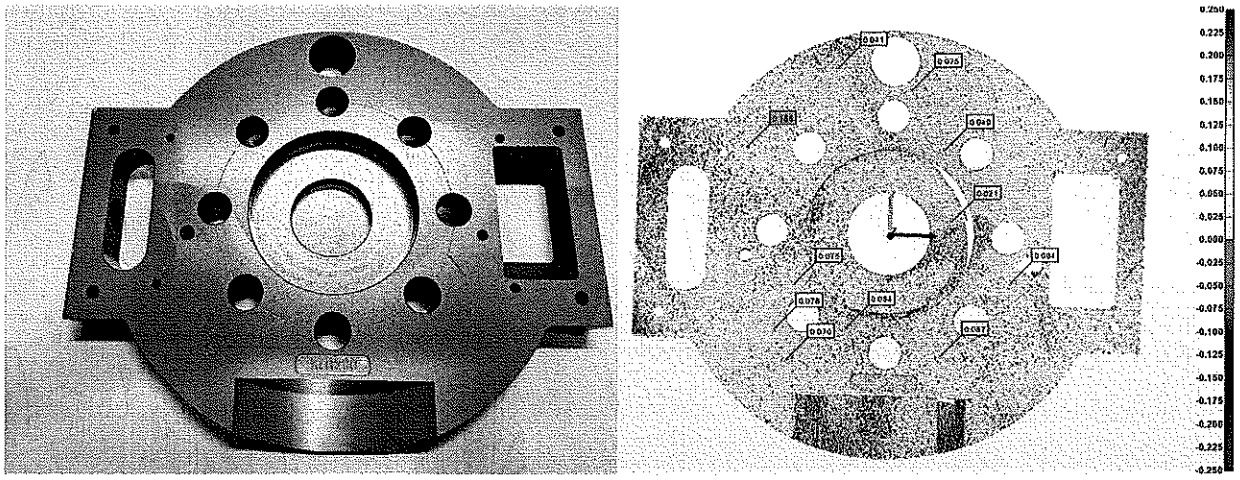

(a) workpiece (b) compare with model

Fig.5.26 Scan the workpiece and calculate the deviation from the model

5.2.4 Measured results and precision analysis

Fig.5.27(left) shows a white plate with a scanning flatness of 0.015 mm. Fig.5.27 (right) shows a point cloud obtained from a white flat board. All points were fit to a plane, and the distance from all points to the plane was calculated. The statistical histogram shown in Fig.5.28 was obtained. The abscissa represents the distance (in mm), while the ordinate is the number of points in the distribution, with 96% distributed within +/−0.05 mm. The main deviation was due to the hand–eye calibration.

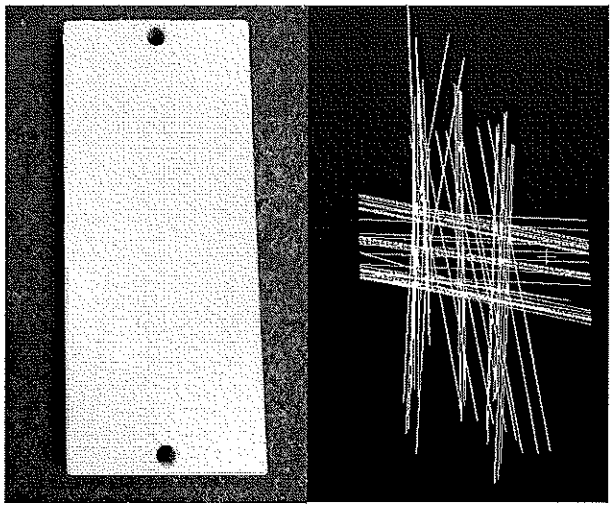

Fig.5.27 Flat board and the scanning result obtained

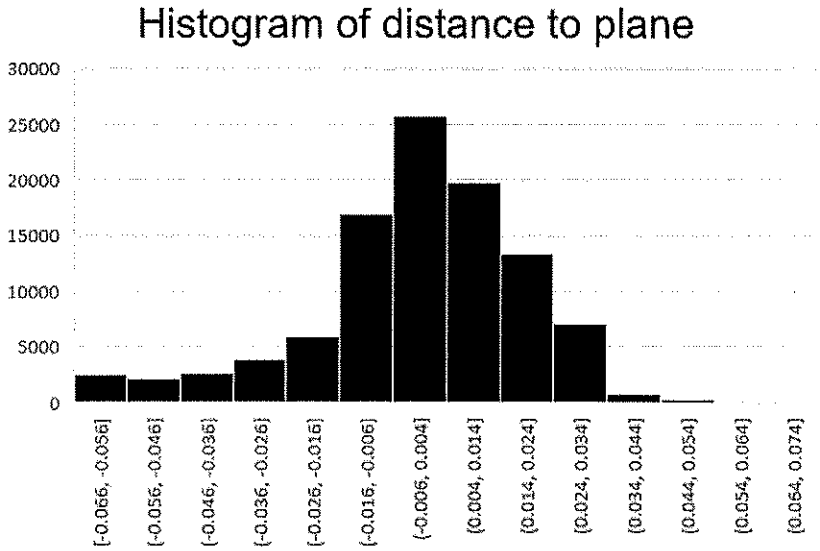

Fig.5.28. Flat board and the scanning result obtained

5.3 multi-lines scanning system experiment

5.3.1 The hardware system

Fig.5.29 is the hardware system used in this experiment. The system mainly consists of a flexible 7-axis articulated arm, multi-line laser, and two 2D cameras. The hardware parameters are follows:

1) The precision of the articulated arm: 0.02mm.
2) 2D camera
   a) The field of view of the camera: 62-72mm.
   b) Acquisition rate:80FPS(frame per second)
   c) Resolution:3072x2048pixel
   d) Work resolution:2658x800pixel
3) multi-line laser
   a) wave length: 650nm
   b) Number of lines:11

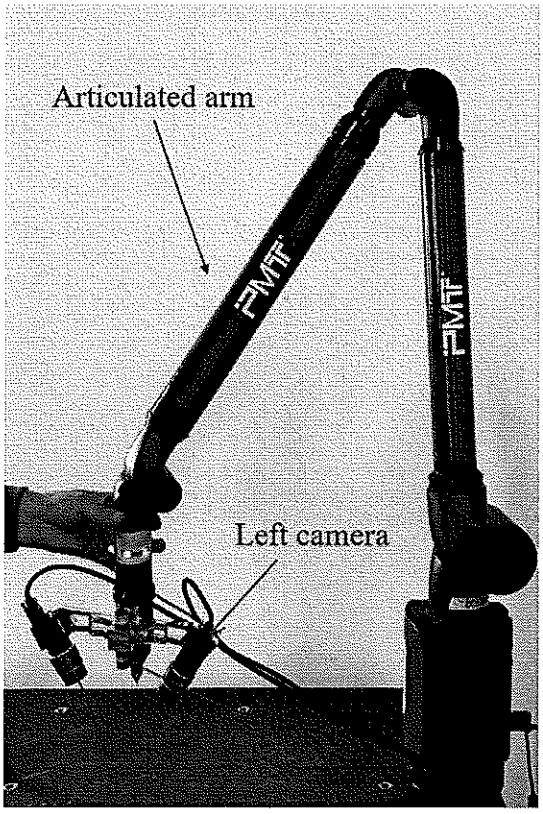

Fig.5.29 Hardware system

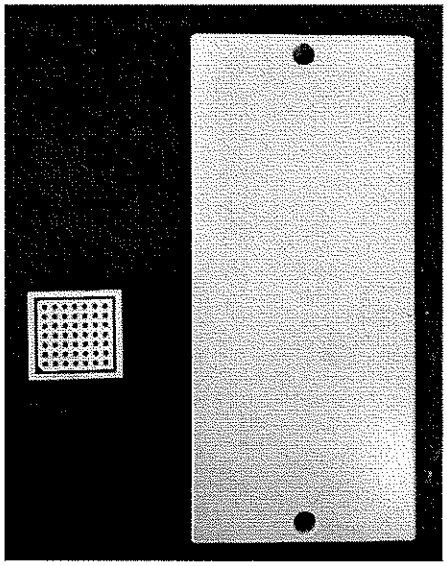

Fig.5.30 Circular array calibration plate and white calibration plate

5.3.2 Binocular calibration

Calibrate the camera with a circular calibration plate.
Calibrate the internal parameter M_L of the camera as follows:

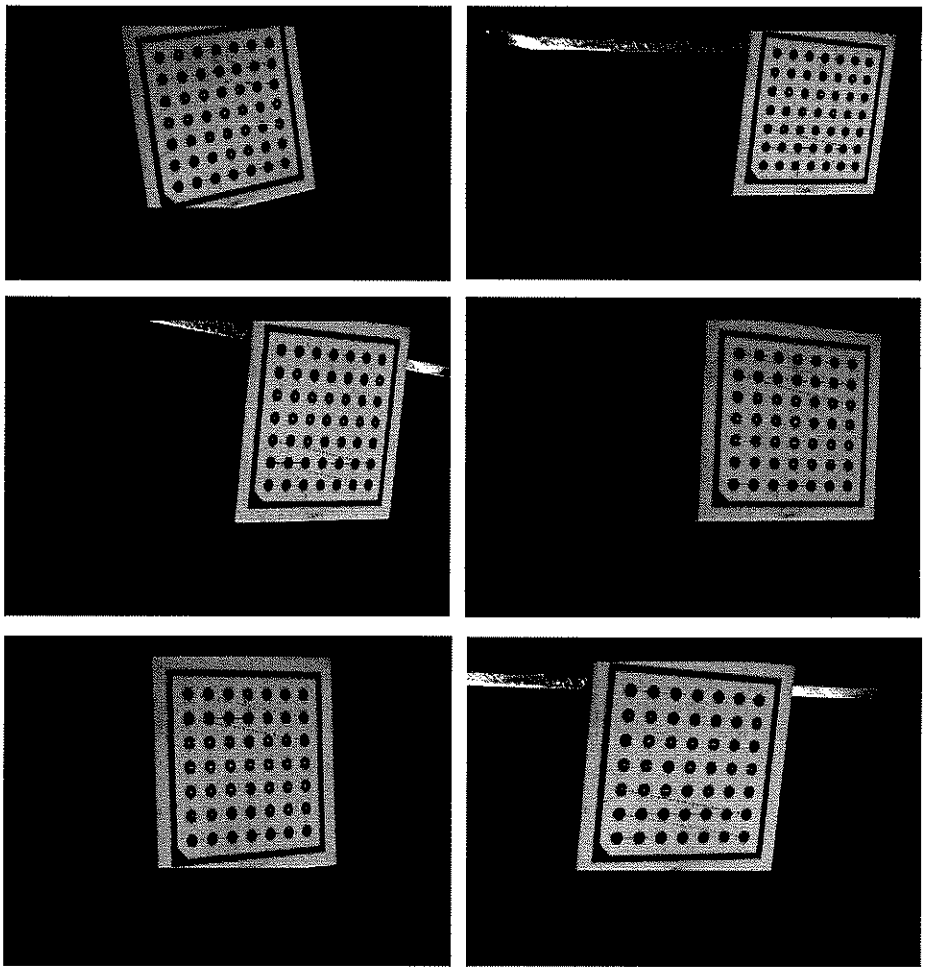

Fig.5.31 Center of circle captured by calibration plate collected

$$M_L = \begin{bmatrix} 5174.97 & 0 & 1524.358 \\ 0 & 5175.62 & 1032.405 \\ 0 & 0 & 1 \end{bmatrix}$$

The corresponding distortion parameter $k_L$is:

$$k_L = [-0.1035\ 0.3449\ 0.000706\ -0.00032\ -0.139]$$

The internal parameter matrix M_R of the right camera is:

$$M_R = \begin{bmatrix} 5163.38 & 0 & 1563.458 \\ 0 & 5162.49 & 1039.554 \\ 0 & 0 & 1 \end{bmatrix}$$

The corresponding distortion parameter k_R is:

$$k_R = [-0.0895\ 0.192148\ 0.000079\ -0.00015\ -0.5824]$$

The rotation relation of the two cameras is:

$$R_{LR} = \begin{bmatrix} 0.546702 & 0.02539 & 0.8369417 \\ -0.03461 & 0.99937 & -0.007715 \\ -0.83661 & -0.0247 & 0.547238 \end{bmatrix}$$

Translation relation is:

$$T_{LR} = [-117.4319 \quad 2.4648 \quad 63.229]^T$$

5.3.3 Optical plane calibration

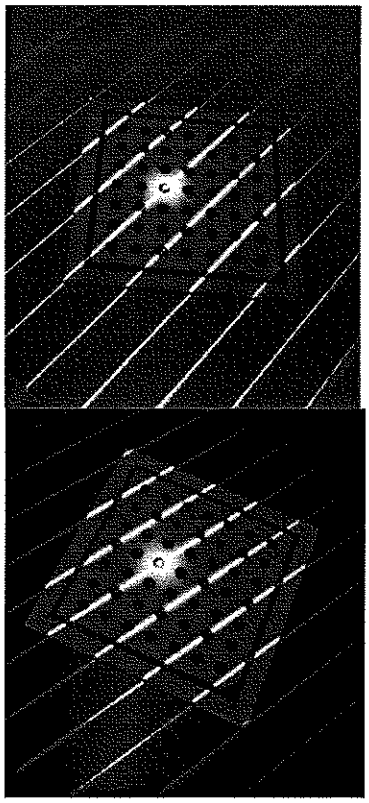

Fig.5.32 Calibration light plane

The circular calibration plate was placed on the plane, the laser line fitting line irradiated on the calibration plate was extracted, the coordinates of the extracted laser line could be calculated

according to the relationship between the left camera and the calibration plate, and the circular array calibration plate could be moved to another position under the condition that the laser and camera were not moved. Solve the coordinates of the laser line. Here, because the straightness of the laser edge is less than the center part, select the middle 5 lines are solved, and the optical plane equation obtained is:

$$A: 0.5465x + 0.7106y + 0.4431z - 43.254 = 0$$
$$B: 0.5772x + 0.7132y + 0.3976z - 44.228 = 0$$
$$C: 0.6050x + 0.7144y + 0.3513z - 45.155 = 0$$
$$D: 0.6316x + 0.7138y + 0.3025z - 45.743 = 0$$
$$E: 0.6565x + 0.7107y + 0.2527z - 46.175 = 0$$

The 5mm measuring block was measured to verify the accuracy of the calibration. Fig.5.33 shows the distribution of measuring point cloud height. The horizontal coordinate indicates that the unit of height measured is mm, and the vertical coordinate indicates the unit of height worth statistics. The mean height is 5.002mm. Std = 0.02.

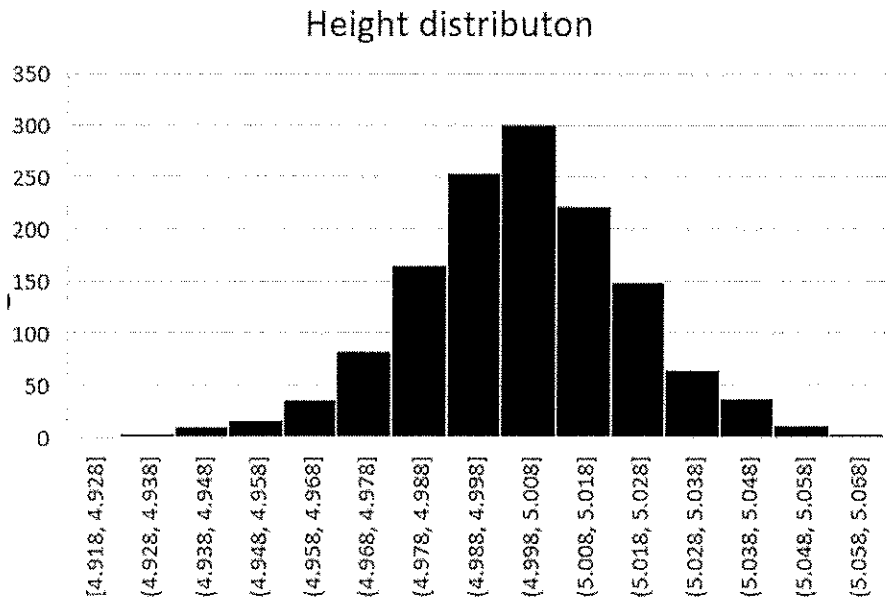

Fig.5.33 Histogram of height

5.3.4 Hand-eye calibration

Fix the white calibration plate on the marble and measure the calibration plate for one week with the measuring arm probe. The general position of the measurement is shown in Fig. 5.34.

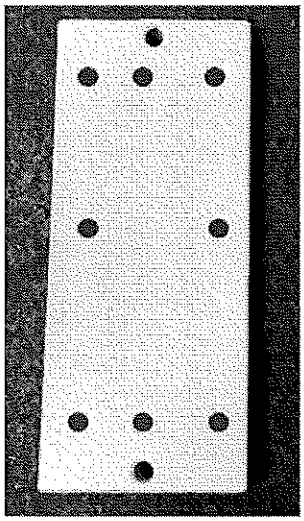

Fig.5.34 Position for probe on the board

The plane equation of the white calibration plate in the coordinate system of the measuring arm base is:

$$[A_b\ B_b\ C_b\ D_b] = [0.00066\ \ 0.0001421\ \ 0.9999\ 6.498867]$$

As shown in Fig.5.35, the measuring arm scans the white calibration plate with the structured

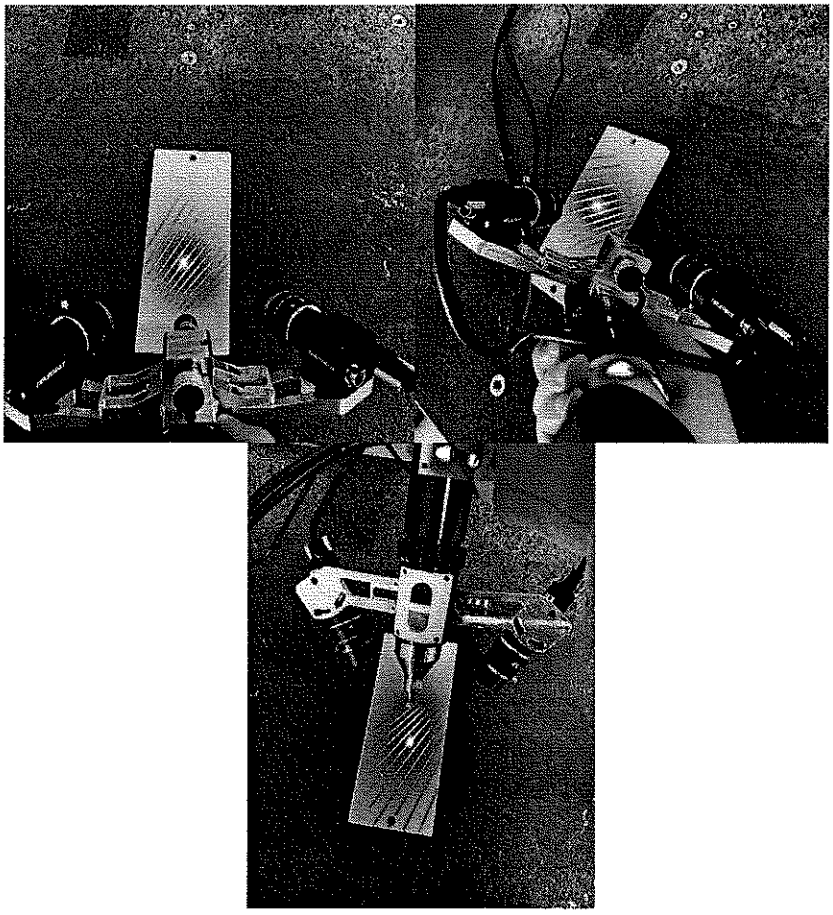

Fig.5.35 Scan the white calibration plate.

light camera. The obtained point cloud data and the attitude matrix ${}_{t}^{b}R$ and ${}_{t}^{b}T$ fed back from the end of the measuring arm to get the solution.

The attitude matrix ${}_{t}^{b}R$ and ${}_{t}^{b}T$ of the feedback at the end of the measurement arm are substituted into equation (2.47) to get the solution.

The rotation relation ${}_{s}^{t}R$ between the multi-line structured light camera and the end of the measuring arm is:

$$ {}_{s}^{t}R = \begin{bmatrix} -0.77305 & -0.44229 & -0.454708 \\ 0.38834 & -0.896779 & 0.212077 \\ -0.50157 & -0.012635 & 0.865022 \end{bmatrix} $$

Quantity of translation ${}_{s}^{t}T$ *is*:

$$ {}_{s}^{t}T = [73.507 \quad 4.651 \quad 119.688]^{T} $$

5.3.5 Scan Test

As the bright spot in the laser center is removed during processing, the point cloud of a frame is obtained, as shown in Fig. 5.36

Fig.5.36 The camera acquires a frame point cloud

The camera can be moved to fill in the gaps as the object is scanned. By scanning the workpiece on the right of Fig.5.37, the complete workpiece can be scanned without the aid of the mark points.

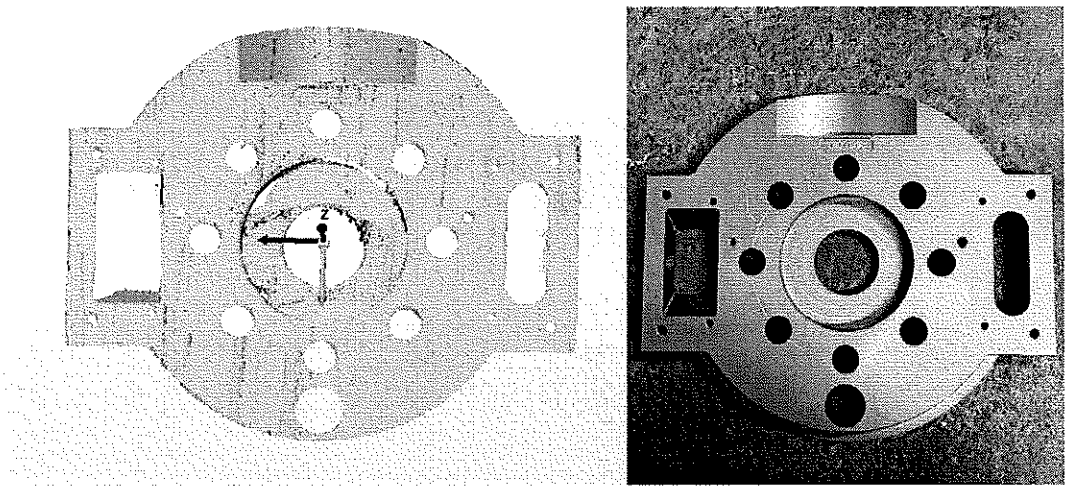

Fig.5.37 Complete artifact scan

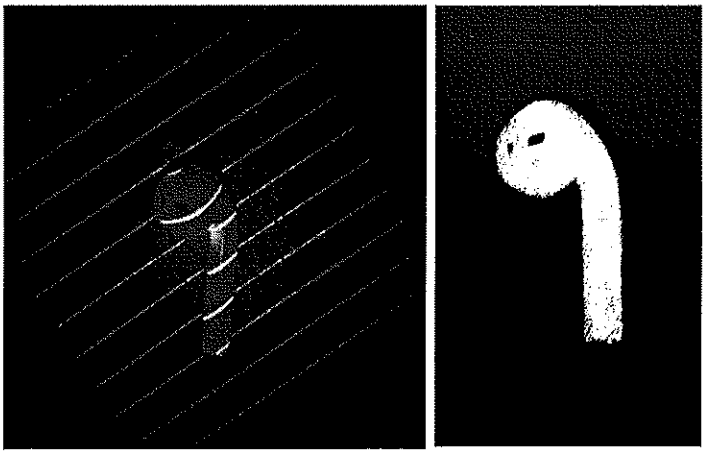

Fig.5.38 Right earphone of airpods

The earphone effect of scanning complex curved surface is shown in Fig.5.38.

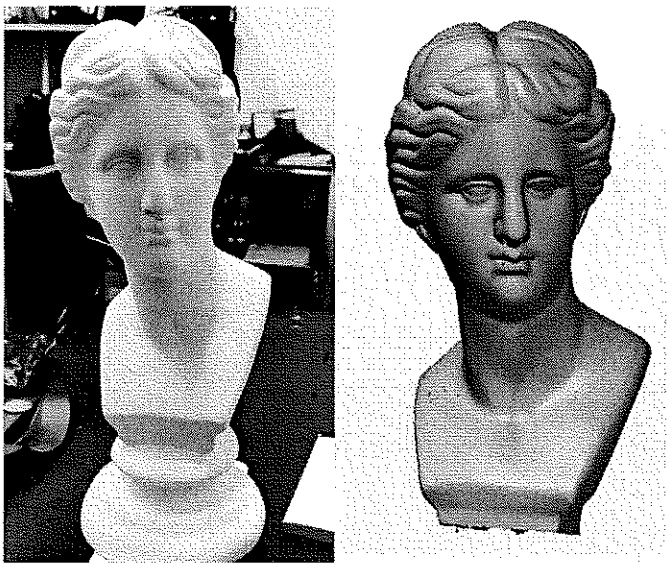

Fig.5.39 Venus statue

Scan Venus statue shown in Fig.5.39(left), the point clouds is shown in Fig.5.39(right).

Point clouds were obtained from five different attitude scanning calibration plates. In Fig.5.40, the same color of the point cloud on the right represents the point cloud acquired at one time.

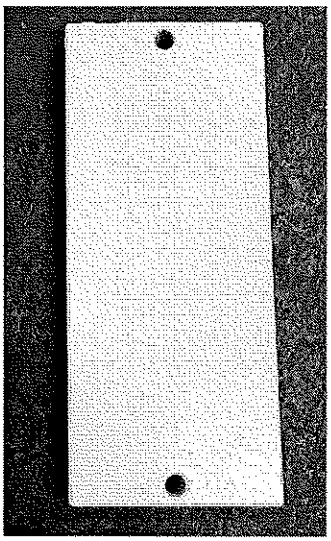

Fig.5.40 The white calibration board on the left and the point cloud on the right.

Fit all the point clouds into a plane. Calculate the distance from the point to the plane. The statistical histogram of Fig.5.41 is obtained. The horizontal coordinate represents the distance, in mm. The y-coordinate is the number of points distributed. 95.1% is distributed at +-0.08mm. The main deviation comes from laser.

In Fig.5.42, the number of point clouds in one frame of three structured light is calculated for the same scene, we find that the number of multi-line structure light point clouds is the largest.

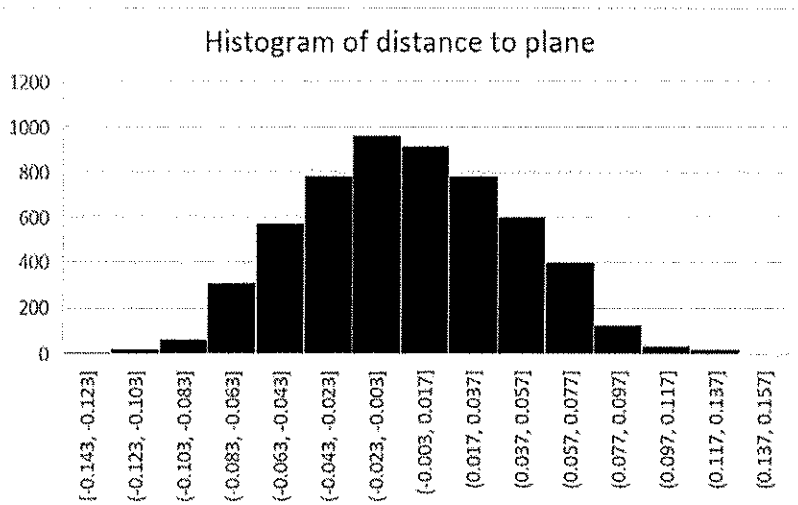

Fig.5.41 Histogram of distance to plane

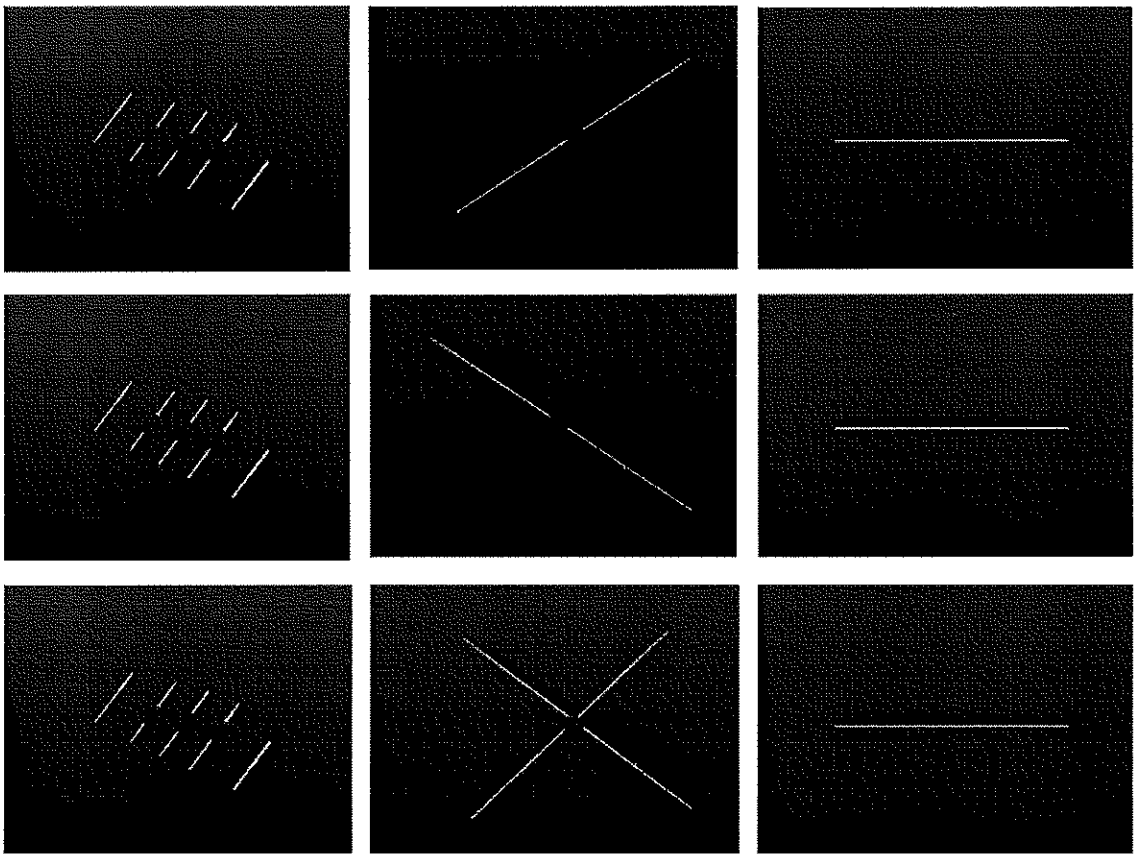

(a) Multi-line structured light
Points number:3859

(b) cross-line structured light
Points number:1171(average)

(c) single-line structured light
Points number:968

Fig.5.42 Point clouds with three forms of structured lights

Chapter 6 Summary

6.1 Conclusion

At present, the advancement of laser 3D scanning technology is gathering its pace. Compared with the traditional measurement solution, it features in speed, accuracy and stability, which can be used in all walks of life. In the future, laser structured light scanning technology will become more and more popular and enrich people's lives. This paper, we study the approach of hand-eye calibration for single-line structured light camera with the end-of articulated arm. In order to improve the efficiency of the single-line structured light based on articulated arm, we extend the single-line structured light to the cross-line structured light. Through the analysis and study of the binocular matching problem of parallel multi-line laser light strip center and based on non-coding point matching problem, this paper proposes detailed solutions, and tested them with lots of experiments. This paper also designs a set of parallel multi-line 3D scanning device based on articulated arm CMM.

This paper proposes a new model scheme for laser 3D scanning technology based on articulated arm CMM, which combines single-line, cross-line structured light system and the multi-lines structured light based on binocular stereo vision. The main contents and achievements of this paper are as follows:

(1) This paper proposes a method for hand-eye calibration based on flat calibration board. Different from the traditional method of using small balls to calibrate the line laser, the flat calibration board is cheap, and flatness is easy-to-guarantee and easy-to-obtain. The acquisition of the center and diameter of the ball is directly related to the obtained spherical data, and the third traditional calibration algorithm relies on the fixed scanning path of the ball, and there is no motor inside the measuring arm for a specific track.

(2) This paper proposes that how a single-line laser scanning technique can be extended to a cross-line laser scanning system in order to improve the scanning efficiency. Moreover, we provided our implementation details, through which an object point cloud can finally be obtained, and showed how to differentiate the cross-line in one frame by comparing the pixel position extracted throughout the frame sequence.

(3) In order to 3D match the point clouds reconstructed for multi-line structured light, non-coding points are required. This paper discusses the combination with the articulated arm CMM to avoid manually attaching marker points, so that the workpiece can be scanned at any time. Under the condition of the same frame rate, the efficiency of multi-line laser scanning system is much higher than that of cross-line and one-line structured light.

(4) Finally, this paper verifies the line laser and articulated arm CMM calibration, and by scanning the standard product, this paper also validates that the accuracy of scanning based on the single-line laser and articulated arm CMM can be controlled within 0.05mm. The experiment verifies the effectiveness of distinguishing different laser light planes when laser A

and laser B are opened in the cross-line structured light system. Considering the linearity of multi-line laser and the problem of bright spots in the middle, the accuracy is 0.08mm, and this paper verifies that the multi-line laser and the articulated arm CMM do not depend on the 3D matching of marker points.

6.2 Next steps and future research

In this paper, a scanning system consisting of the structured light with the articulated arm CMM is verified. The frame rate of 3D points was 1.33 times faster than that of single-line structured light with the same 2D camera ideally. However, it should be noted that further work is necessary to improve the ratio of AB opening simultaneously, which may increase the efficiency of scanning by controlling the periodicity of the two lasers. The red laser used in for multi-lines scanning system in the experiment has bright spots in the middle, so the extraction of the centerline and irradiation of the high-reflection material will interfere with other laser lines. In the next step, we need to replace it with a laser projector with good straightness and no stray light interference in the middle.

We also have to consider deploying more laser lines, and more and more compact, easy to operate. The real sense of fast, convenient, high precision.

Acknowledgements

I would first like to thank my tutor Prof. Lu of Graduate school of Intelligent Information System Engineering at Fukuoka Institute of Technology. Three years ago, he leaded me to the field of Measurement of image and has been my tutor since then. Prof. Lu held online meetings every day, all of us reported our research progress, and then Prof. Lu gave us guidance. We also know about other students' research, we learn from each other and improve each other. Prof. Lu provides us with a good learning platform, all the students in our lab have not only gained research results, but also gained friendship each other. Prof. Lu is very strict in academic research, but at the same time, he helped me a lot in all aspects of life and studies during my studies in Japan or in China, including but not limited to teaching me how to write a paper, how to do experiment, helping me revise my paper, and answering questions that arise in my research. He is also the supervisor of this thesis, without his help, this thesis could not have been successfully completed as now.

I would also thank the other professors on the doctoral review committee. Their insightful comments and useful advice greatly helped me to refine my PhD thesis. Especially Prof. Song. In the last semester, he agreed to set up courses for me, so that I could learn more knowledge outside my major, which could better help me finish my PhD thesis and rethink my work and study. There is also Miss. Li from the student affairs Department, who has given me a lot of help in my life and cares about our life in Japan. In addition, our dormitory management staff were also very friendly and made us feel at home in Japan. To all of them, I would like to thank them.

I would like to thank other classmates at the same laboratory for their kind help in my studies and life. Most of the time spent in the laboratory is enjoyable due to their kindness and help. Due to the epidemic, we communicated online in Japan and China respectively. All of the experiment data were obtained by their help, this research work could not be completed without their help.

Finally, I must give my faithful gratitude to my family, continuous encouragement throughout these three years and through the process of researching and writing my PhD thesis. Due to the three years of COVID-19, all economic activity stops, We are faced with many difficulties and challenges, we overcame a lot of difficulties together. My accomplishment would not have been possible without them. Thank you.

I will work harder and hard in my future study and work to live up to the help of all the above person.

References

[1] Han Qing Hua, Zheng Bao, Gu Hong Li, Wang Hong Xiang: Measurement of aircraft by using laser tracker equipment, 24, 15-16, 2004.

[2] Zhou Jun: Application of optical scanning measuring technology in quality control of auto products, Robot, 3, 63-79, 2006.

[3] Wang Jian Jun, Wang Ying: Application of raster metering to hull transverse twist measurement, Optics and Precision Engineering,13,371-375.2005.

[4] Hu Cheng Xin, Lin Xin Yu, Liu Guang Dong: Application of CMM in the inspection of aerospace vehicle parts,9,141-143.2022.

[5] Zhang Hong Wei, Zhang Guo Xiong, Li Zhen: Non-contact measurement of the surface of aircraft engine blade, Aviation precision manufacturing technology, 40, 34-36, 2004.

[6] Wehr A, Lohr U:Airborne laser scanning an introduction and overview, Isprs Journal of Photogrammetry & Remote Sensing,54,68-82.1999.

[7] Axelsson P:Processing of laser scanner data algorithms and applications, Isprs Journal of Photogrammetry & Remote Sensing, 54,138-147.1999.

[8] Takeda M, Mutoh K:Fourier transform profilometry for the automatic measurement of 3-D object shapes, Applied Optics, 22,3977-3982,1983.

[9] Ghiglia, Dennis C:Two-dimensional phase unwrapping:theory, algorithms, and software, Analyticalscience.wiley.com, 1998.

[10] Sun X, Chen Wu:Fourier transform profilometry:a review, Optics & Lasers in Engineering,35,263-284.2001.

[11] Sjödahl M, Synnergren P: Measurement of shape by using projected random patterns and temporal digital speckle photography, Applied Optics, 38,1990-1997.1999.

[12] McMutry, DavidR:Touch Probe.USA Patent, No:5146691.1992.

[13] Peggs G N:A review of the method for the accurate metrology of Complex three-dimensional components and artifacts, NPL Report MOM101,1991.

[14] Ding W:Research on error analysis of the non-orthogonal coordinate measurement system, Tianjin Unversity,2017.

[15] B Parry,D Beutel:Methods for performance evaluation of articulated arm coordinate measuring machines ,asme.B89.4.22.2004.

[16] https://www.faro.com/en/Products/Hardware/ScanArms 2022.

[17] https://www.hexagonmi.com.cn/cms/p-316.aspx 2022.

[18] https://www.pmt3d.com/products.html 2022.

[19] https://www.kosakalab.co.jp/english/product/precision/3_dimensions/ 2022.

[20] Su X, Zhang Q: Dynamic 3-D shape measurement method: a review, Optics &Lasers in Engineering, 48,191-204.2010.

[21] Ding L Y, Yu Lie, W,U. Sheng-Yi L I:Surface measurement for long focal length mirror with phase retrieval, Photonica Sinica,39,1431-1437.2010.

[22] Duan F J, Liu F M, Ye S H:A new accurate method for the calibration of line structured light sensor, Chinese Journal Ofentific Instrument, 2000.

[23] Jarvis R A:A laser time-of-light range scanner for robotic vision, IEEE Transactions on Pattern Analysis & Machine Intelligence,5,505-512, 1983.

[24] D M Johnson, W O: Generation of surface contours by moiré patterns, Applied Optics,9,942-947, 1970.

[25] https://www.robosense.cn/rslidar/RS-Ruby_Plus 2022.

[26] Wang Xiao Jia, Gao Xie,Wang Lei: Survey one the laser triangulation, Instrumentation,25,601-604, 2004.

[27] Zhi Hua Lv, Zhi Yi Zhang: Build 3D Scanner System based on binocular stereo vision, Journal of computers,2,399-405,2012.

[28] Ma Song De, Zhang Zhen You:Computer Sicence, Science Press, 1998.

[29] https://polhemus.com/scanning-digitizing/fastscan/ 2022.

[30] https://www.creaform3d.com/en/portable-3d-scanner-handyscan-3d 2022.

[31] https://www.keyence.com/products/measure/ 2022.

[32] Simon Raab, Sajedi Seyed Ali, Hasloecher Kenneth:Method for improving measurement accuracy of a portable coordinate measurement machine,8,15-18, 2003.

[33] Simon Raab, Sajedi Seyed Ali, Hasloecher Kenneth :Portable coordinate measurement machine with integrated touch probe and improved handle assembly,13-16,2005.

[34] Santolaria J, Brau A, Vel A Zquez J: A self-centering active probing technique for kinematic parameter identification and verification of articulated arm coordinate measuring machines, Measurement Science and Technology. 2010.

[35] Ruibo He, Yingjun Zhao, Shunian Yanget:Kinematic-Parameter identification for serial-robot calibration based on POE formula, IEEE Transactions on Robotics,26,411-423,2010.

[36] Gatti G, Danieli G:A practical approach to compensate for geometric errors in measuring arms: application to a six-degree-of-freedom kinematic structurem, Measurement Science and Technology,19,151071-1510712,2008.

[37] Schr O Er K, Albright S L, Grethlein M:Complete minimal and model-continuous kinematic models for robot calibration, Robotics and Computer-Integrated Manufacturing. 13,73-85,1997.

[38] Denavit J,Hartenberg R B:A kinematics notation for lower-pair mechanism based on matrices, Journal of Applied Mechanics,23,215-221, 1955.

[39] Weng J, Cohen P, Herniou P: Camera calibration with distortion models and accuracy evaluation, IEEE Transaction on Pattern Analysis and Machine Intelligence, 14,965-980, 1992.

[40] Wong W:Mathematical formulation and digital analysis in close range photogrammetry, Photogrammetric Engineering and Remote Sensing, 41,1355-1373, 1975.

[41] Zhen You Zhang: A Flexible new technique for camera calibration, IEEE Transactions on Pattern Analysis & Machine Intelligence,22,1330-1334, 2000.

[42] Zhang Fen Shen:A new numerical simulation method for Gaussian beam,Acta Phot on ica sinica,37,1259-1262, 2008.

[43] Izquierdo M A G, Sanchez M T, Ibañez A:Sub-pixel measurement of 3D surfaces by laser scanning, Sensors & Actuators A Physical,76,1-8, 1999.

[44] Li Ying Yin, Zhang Zhi Yi, Yuan Lin:Survey on linear structured light stripe center extraction, Laser&Optoelectronics progress,10,9-18,2013.

[45] Liu Zhen. Research on techniques for binocular stereo vision based on structured light, University of Chinese Academy of Sciences, 2013.

[46] Seymour J, Browne J:Recent progress in coded structured light as a technique to solve the correspondence problem: a survey, Pattern Recognition,31,963-982, 1998.

[47] Duan F J, Liu F M, Ye S H: A new accurate method for the calibration of line structured light sensor, Chinese Journal Ofentific Instrument, 2000.

[48] Huynh D Q, Owens R A, Hartmann P E: Calibrating a structured light stripe system: A novel approach, International Journal of Computer Vision,33,73-86, 1999.

[49] Y J Ren, S B Yin, J G Zhu:Calibration technology in application of robot-laser scanning system, Opt. Eng. 11, 20-26.2012.

[50] Zhang Wei, Zhong Zhang, Li Yan Pan, Zhen Kuan W, Xiao Ping, Zhou Ling: Close-range photogrammetric system based on reference points, Journal of Southeast University,36,741-745,2006.

[51] Zhen Xiao Jie: Research of key technologies in close range photogrammetry applied in reverse engineering, Shanghai Jiao Tong University, 2007.

[52] Felsberg M, Sommerm G:The monogenic signal, IEEE Transactions on Signal Processing,49,3136-3144, 2001.

[53] Shan Xin, Wang, Yao Ming, Dong Jian Ping: The matching method based on RANSAC algorithm for estimation of the fundamental matrix, Shanghai DianJi University,9,66-69.2006.

[54] Liang Y B, Deng W Y, Lou X P:Automatic registration method of multi-view 3D data based on marked points, Journal of Beijing Information Science & Technology University, 30,490-508, 2010.

[55] Ji Gui Z, Lei G, Sheng, Hua Y:Principle and implementation method of thre-dimensional precision positioning in large field working space, Acta Optica Sinica, 29,1872-1876.2009.

[56] Zhang Chen Bo:Research and application of hand - held 3D laser scanning technology based on parallel multi-lines, Nanjing University of Aeronautics and Astronautics.2017.

[57] https://www.innovmetric.com/products/polyworks-inspector 2023.